Ultrathin Iron Oxide Films on Ru(0001)

Author:
Matteo Monti

Supervisor:
Dr. Juan de la Figuera
Co-Supervisor:
Dr. José F. Marco

A thesis submitted in fulfilment of the requirements for the degree of Doctor of Philosophy in Physics

Departamento de Física Aplicada
Madrid, June 9, 2014

"...conquering matter is to understand it, and understanding matter is necessary to understanding the universe and ourselves..."

Primo Levi

Abstract

In this dissertation the growth and properties of ultrathin iron oxides films on ruthenium have been investigated by means of diffraction, microscopy and spectroscopy techniques. The systems studied have been prepared *in-situ* using molecular beam epitaxy and oxygen-assisted molecular beam epitaxy. We begin with the preparation of ultrathin FeO films following their growth on Ru(0001) by low-energy electron microscopy and scanning tunneling microscopy. After a brief spectroscopic and structural characterization, the role of the experimental parameters, i.e., temperature and oxygen pressure, in the growth mechanism has been discussed. Then, the preparation of a bi-component iron oxide film on ruthenium has been presented. This system, composed by an FeO wetting layer and perfect magnetite crystals, has been characterized by means of structural and spectroscopic measurements. Focusing on these magnetite crystals, we have shown that selecting adequately the experimental conditions they can maintain their stability even when their thickness is reduced at the nanometer scale. Additionally, we have characterized the magnetic properties of these crystals using synchrotron radiation-based techniques, and we have found that they exhibit well-defined magnetic domains proving that ferrimagnetism can be retained in these $\sim$1 nm thick magnetite films.

Next, the oxidation of this bi-component film by NO_2 has been studied. The chemical transformation of the initially-grown film takes place producing a different bi-component film, formed by an hematite wetting layer and maghemite crystals. We have been able to propose an oxidation mechanism consisting in a topotactic transformation experienced by the iron cations. Thus, by means of a choice of the experimental parameters, the preparation of different bi-component iron oxides in ultrathin film form on the same substrate can be achieved.

Finally, we reported the design and construction of an ultra high vacuum integral low-energy electron Mössbauer spectrometer aimed at the chemical, structural and magnetic characterization of Fe-containing surfaces. The proposed design together with the optimization procedures have been presented and discussed. The first results on bi-component iron oxide films suggest that this unconventional Mössbauer spectroscopy is suitable for measurements of iron oxide nanostructures.

Resumen

Los óxidos de hierro son considerados materiales prometedores de cara a futuros desarrollos en diferentes campos tecnológicos como la catálisis, la biología, o la microelectrónica. A pesar de ser compuestos ampliamente estudiados, está demostrado que las propiedades de volumen se ven fuertemente modificadas en superficie o afectadas por la reducción de sus dimensiones a escala nanométrica. Para favorecer un correcto desarrollo de los dispositivos en el cual estos materiales están involucrados, es de crucial importancia obtener un conocimiento detallado de cómo las propiedades químico–físicas de los óxidos de hierro dependen de los fenómenos superficiales y de los efectos de baja dimensionalidad. De acuerdo con esto, el objetivo principal del trabajo presentado es el estudio de cómo se modifican las propiedades de los óxidos de hierro cuando están preparados en capas ultra-delgadas.

Inicialmente mediante técnicas de microscopia, espectroscopia y difracción, hemos investigado películas de FeO preparadas mediante la técnica de epitaxia de haces moleculares, tanto estándar como asistida por oxígeno molecular. Hemos detectado que, dependiendo de las condiciones experimentales utilizadas, la morfología de las películas crecidas sobre Ru(0001) se modifica, dejando inalterada la naturaleza químico–física del material. Realizando estudios con microscopía de electrones de baja energía hemos podido investigar y proponer un modelo que describe la dependencia del mecanismo de crecimiento de las películas de FeO con la presión de oxígeno y la temperatura del substrato.

En una segunda etapa, hemos crecido películas de óxidos de hierro compuestas de una capa continua de FeO sobre la cual se ha identificado la nucleación de cristales de magnetita. Hemos centrado nuestra atención en los cristales de magnetita y, combinando técnicas de microscopia, espectroscopia y difracción hemos observado como dichos cristales permanecen estables aunque su espesor se mantenga muy próximo a un nanómetro. Además, se han estudiado las propiedades magnéticas de estos cristales nanométricos mediante dicroísmo magnético circular de rayos X, demostrando que el carácter ferrimagnético se mantiene a pesar de ser extremadamente delgados.

En una tercera etapa, los cristales de magnetita crecidos sobre una *wetting layer* de FeO se han expuestos a un gas reactivo (NO_2) y se ha estudiado el mecanismo de oxidación utilizando las técnicas mencionadas anteriormente. Se ha detectado que la fase FeO se oxida dando lugar a una *wetting layer* compuesta por hematita mientras los cristales de magnetita evolucionan formando maghemita. Los distintos procesos de oxidación se han explicado proponiendo un mecanismo topotáctico en el cual están involucrados los cationes de hierro de las diferentes estructuras. En particular, hemos podido describir como selecionando adecuadamente parámetros experimentales es posible preparar una

película ultra-delgada de óxidos de hierro de distinta composición sobre el mismo substrato metálico.

Finalmente, hemos presentado y discutido la construcción y la puesta en marcha de un espectrómetro Mössbauer para la detección de electrones de baja energía. Dicha técnica basada en el efecto Mössbauer proporciona información químico-física con sensibilidad superficial de nanoestructuras que contengan hierro. Hemos presentados los primeros resultados obtenidos de la caracterización de películas ultra-delgadas de óxido de hierro descrita anteriormente, demostrando así la extrema versatilidad de esta técnica en los estudio de nano-estructuras.

Acknowledgements

Iniciando esta tesis doctoral querría agradecer a muchas de las personas que he encontrado y me han ayudado a lo largo de estos cinco años.

En primer lugar tengo que dar las gracias a mi supervisor Juan, que desde el principio ha confiado en mí dándome la posibilidad de empezar mi carrera investigadora en su grupo. Ha sido un orgullo trabajar con él y aprender el gusto de la investigación. Sus estímulos, sus consejos y el entusiasmo que siempre me ha transmitido, han sido preciosos y fundamentales en el desarrollo de esta tesis. Muchas gracias Juan, espero, un día, tener la fortuna de poder colaborar contigo otra vez.

Quiero agradecer también a mi codirector de tesis, Pepe. No olvidare su disponibilidad y su esencial ayuda a lo largo de estos cinco años. En particular ha sabido transmitirme el optimismo necesario para superar los momentos más complicados.

Gracias a Ramón y Mercedes que han sido siempre muy gentiles conmigo en compartir sus sabidurías y sus consejos. Ramón, nunca olvidare tu destreza con la navaja suiza para solucionar los inconvenientes en laboratorio.

I would like to acknowledge my supervisors, Kevin and Andreas, who gave me the chance to work at Sandia and Berkeley. It was a pleasure to work with you and spend great moments during the Californian summers.

Doy las gracias a todos los compañeros con los cuales tengo la suerte de trabajar, Laura, Raquel, Carlos y M^a. Carmen y a los que se han pasado por el laboratorio, Lucia, Tirma, Benito, y Roberto.

Un agradecimiento a todo el personal del "Roca". En particular a José y Nacho del taller mecánico y Pedro del taller de electrónica que han sido colaboradores fundamentales en el desarrollo de muchos de los equipos que hemos utilizados. Y al grupo de laseres (LANAMAP), Marta, Mikel, y Mohamed.

No puedo dejar de dar las gracias a Farid, ha sido un placer trabajar contigo y sobre todo pasar unos bellos momentos bajo el limonero o en San Francisco viendo algún concierto. A Carlota y a las niñas, no olvidare vuestra hospitalidad.

A los colaboradores de la UCM, en particular Arantzazu, y Oscar.

Thanks to the Sandia collaborators, Norm, Shu, David for their support with the LEEM and I wish to thank Gong and Alpha for their support at the NCEM.

A mis amigos del master, Manu, Annalisa, Marcos, Constanza, Miriam, Sonia, Darío, Esther, Valerio.

A tutti gli amici di Montegalda che porto sempre con me ovunuque vada, soprattutto adesso che le famigliole si stanno allargando! In particolare un grazie a Doris che mi è sempre vicina, soprattutto quando ne ho piu' bisogno.

A la súper doctora Elena (McPos), porque su apoyo y su ayuda han sido fundamentales para empezar mi experiencia en España.

Un grazie anche a tutti i super dottori di Padova, Luca X, Diego, Eddy, il Volto. Anche se ho tradito la chimica per la fisica, sotto sotto restero sempre un chimico.

A Meeno and Dootcho, per la magnifica "estate" californiana.

A mis compañeros de piso Xuanín, Aroa, el Buta, y Raúl que han sido como una familia a lo largo de esto cinco años en Madrid. No será fácil dejar el piso en septiembre.

A Pippo, sempre gentile e disponibile a lunghe chiaccherate (e birrette) in compagnia.

In fine voglio ringraziare tutta la mia famiglia. In particolare i miei genitori che sempre hanno creduto in me appoggiandomi e dandomi fiducia soprattutto quando ho decido di lasciare l'Italia. Ringrazio le mie sorelle perchè mi sono vicine anche a mille chilometri di distanza. Ringrazio la nonna che sempre mi supporta con il suo affetto.

* * *

Contents

List of Figures

List of Tables

Dedicated to Laura

Chapter 1

Scope of The Research

Iron oxides are common compounds which are widespread in nature and constitute an important class of materials. Thinking about the importance of iron oxides for the humankind, magnetite, one of the most abundant magnetic minerals in earth's crust, comes to mind as a clear example. For many years, magnetite found a wide technological application range from navigation (compasses) to modern high density magnetic recording media. Moreover, iron oxides prepared in several nanostructure forms are also involved in environmental science, catalysis, biology, electronics, and other fields.

This dissertation studies several aspects of iron oxide grown on Ru(0001) and the modification of their properties when one dimension is reduced at the nanoscale limit. Since the preparation of iron oxides with defined structure and stoichiometry turned out to be not trivial, a basic understanding of the chemical and physical properties of ultrathin films becomes fundamental in order to tailor them for desired applications. For these purposes, we select the most common binary iron oxides: Wüstite (FeO), Magnetite (Fe_3O_4), Maghemite (γ–Fe_2O_3) and Hematite (α–Fe_2O_3).

This thesis begins with the experimental Chapter 2 in which the experimental methods are presented. We follow by discussing the first iron oxide, wüstite, and its applications in heterogeneous catalysis. Since the FeO catalytic proprieties are directly related to the structure and the morphology of the nanostructures, we consider relevant to research the preparation of FeO ultrathin films. Thus, by means of a surface-science approach, we study the growth and the structural properties of ultrathin FeO films pointing out their relationship with the preparation methods (Chapter 3).

In Chapter 4, we introduce a more "curious" iron oxide, magnetite, giving more emphasis to its magnetic properties for which this oxide is attractive. Since magnetite has been suggested as promising material for microelectronic applications, the fabrication

of this oxide with well-defined properties remains an important challenge. Thus, after a brief overview about the magnetite growth and its relationship with the experimental conditions, we try to answer of how the question about how the magnetic properties of magnetite ultrathin films change with respect to their bulk counterpart.

Maghemite (γ–Fe_2O_3) and Hematite (α–Fe_2O_3) are finally introduced in the Chapter 5. We follow by discussing the oxidation mechanisms of ultrathin iron oxide films and the possibility to prepare precise oxide phases by selecting adequately the experimental conditions.

In Chapter 6, we explain the basic concepts and an instrument design of a novel surface science technique based on the Mössbauer effect: integral low-energy Mössbauer spectroscopy. The optimization procedures and the first results about ultrathin iron oxide films are also presented.

Finally, the thesis finishes with the concluding Chapter 7 which gives a general discussion about the main results.

Chapter 2

Experimental Details

2.1 Introduction

In this chapter, we will present the techniques used to perform our experiments. First, we will start introducing the "Surfmoss" system located at the *Instituto de Química Física "Rocasolano"* (Madrid). It is an ultra-high vacuum chamber equipped with classical surface techniques that provide a detailed control of the experimental procedures, from the sample preparation to its characterization. Because the system has been entirely home-designed and built during the thesis, some aspects of the experimental system will be described.

Next, we will present the low-energy electron microscope (LEEM) and the photoemission electron microscope (PEEM). They are two techniques that have been used at different stages at Sandia National Laboratories (USA) and at Elettra Synchrotron Lightsource (IT). The LEEM-PEEM instrument offers a combination of microscopy and spectroscopy that allows to obtain detailed information about the morphology, structure and chemical composition of the sample surface.

Finally, the methods used for the specimen preparation are commented.

2.2 The "Surfmoss" Chamber System

The "Surfmoss" chamber system is a multi-purpose UHV chamber equipped with a variable temperature scanning tunnel microscope (VT-STM), an hemispherical electron analyzer for x-ray photoelectron and Auger spectroscopies (XPS, AES) and a low-energy electron diffractometer (LEED). The fundamental ideas that inspire the development of the "Surfmoss" system are the use of the common surface science techniques in a

single system and the ability to carry out *in-situ* experiments. While the chamber has been designed at our laboratory, its fabrication has been commissioned mostly to SEGAINVEX at the Universidad Autónoma de Madrid [14]. In Figure 2.1a we show the first vacuum test on the as-received chamber. During the Spring of 2010, the main chamber was completed with a fast-entry system and a VG Clam 2 electron analyzer coupled with an x-ray gun for XPS analysis. The sample handling was performed by two transfer bars and a conventional one axis manipulator (more details in Appendix A). A Specs μ-focus differential pumped Ar^+ gun and a mass spectrometer completed the first chamber setup 2.1b.

We improved the system in 2011 when a home-made variable temperature scanning tunneling microscope was mounted in the main chamber. The VT-STM designed by B. Diaconescu and coworkers [15], was built by B. Santos in our laboratory. An extensive description about the assembly and the operation procedures are reported by B. Santos in his PhD dissertation [16]. We added several electron-bombardment metal dosers that allow a high quality film growth by means of molecular beam epitaxy (MBE). Like the VT-STM, all the evaporators were designed by us and made at the SEGAINVEX machine shop. The XPS system was upgraded with an high performance Specs Phoibos 150 electron analyzer, a new high intensity twin anode x-ray source, and a Staib electron gun coupled with a secondary electron detector for scanning electron microscopy (see Figure 2.1c and Figure 2.2). The new analyzer is characterized by a 150 mm mean radius, nine channeltron detectors and several entrance slits (see the schematics in Figure 2.7). All these aspects contributed to improve the quality of the experiments radically. At this point we reached the ability to produce high quality samples and characterize their morphology and chemical composition with surface sensibility.

In 2012 we added a low-energy electron diffractometer for laterally averaged low-energy electron diffraction (LEED) used for surface structure determination. Furthermore, the manipulator was replaced by a two-axis manipulator. The new manipulator has been customized at the "Rocasolano" machine shop incorporating an additional tilt (see Figure A.3 in Appendix A). The goal of this simple modification is to improve the diffraction measurements. The new tilt allows the correct aligning of the sample normal relative to the incident electron beam during LEED measurements. To separate the preparation from the characterization areas we added a preparation chamber. Because the preparation chamber has been equipped with an independent pumping system, the main chamber vacuum is maintained during the growth procedures.

Finally, we installed another chamber for integral low-energy electron Mössbauer spectroscopy (ILEEMS). This unconventional variant of Mössbauer spectroscopy is an effective technique for the analysis of iron-containing surfaces. Information about structure,

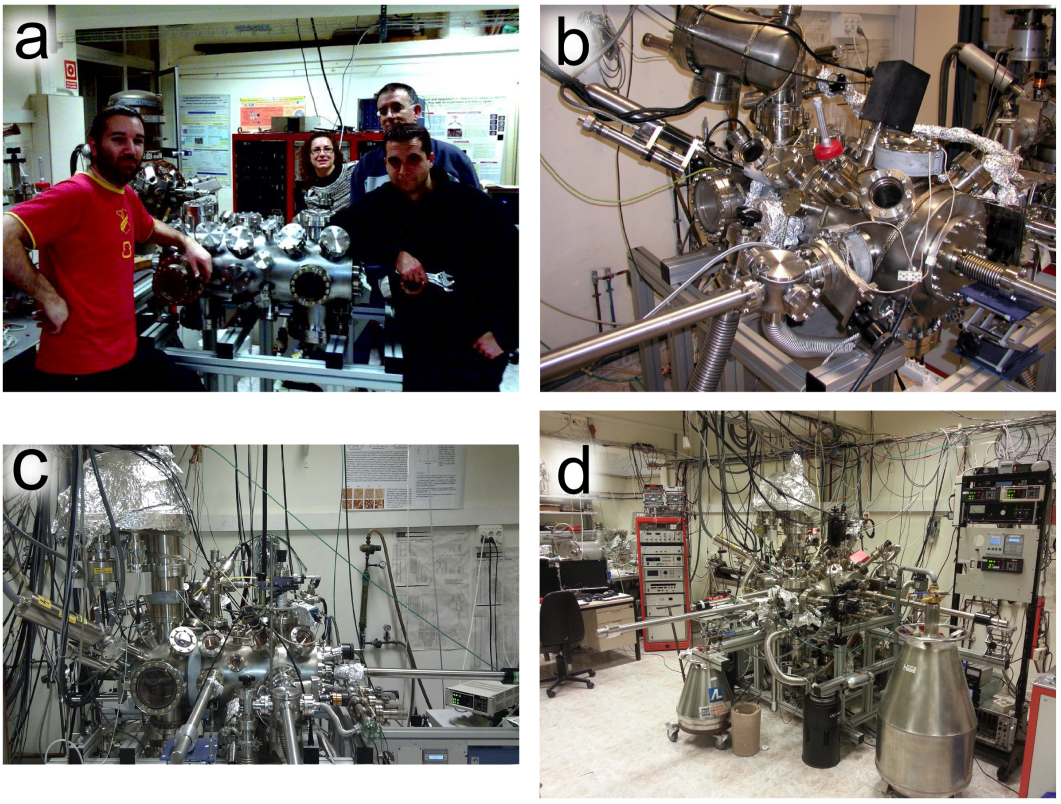

FIGURE 2.1: Stages of the "Surfmoss" system. **a**. The chamber as-received from SEGAINVEX (February 2010). **b**. First configuration (April 2010). **c**. With Phoibos analyzer (September 2011). **d**. Present configuration with preparation chamber and Mössbauer chamber (Summer 2013).

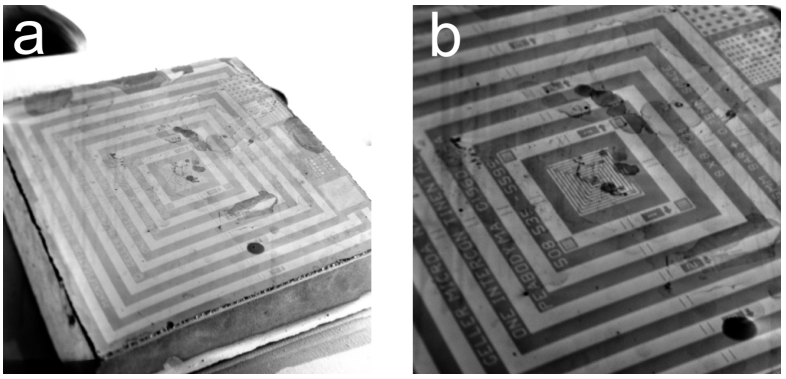

FIGURE 2.2: MRS-3 sample for calibration imaged by SEM . **a**. SEM image collected at 1 kV (magnification × 10). The overall size of the sample is 9×9×2.3 mm **b**. SEM image collected at 2 kV (magnification × 10).

TABLE 2.1: Summary of "Surfmoss" System Equipment

Characterization Techniques	
Method	*Acronym*
X-ray Photoelectron Spectroscopy	XPS
Scanning Electron Microscopy	SEM
Low-Energy Electron Diffraction	LEED
Scanning Tunneling Microscopy	STM
Residual Gas Analyzer	RGA
Integral Low-Energy Electron Mössbauer Spectroscopy	ILEEMS
Auger Electron Spectroscopy	AES

Preparation Techniques
Several metal evaporators for MBE
Ar^+ ion gun
O_2 and NO_2 leak valves

Pumping Systems
Oil-free roughing pump station
Turbo-molecular pumps
Ion pump
Titanium sublimation pump
Non-evaporable getter

chemical state, phase analysis and magnetic structure can be obtained by ILEEMS. A complete description of the basic principles, the technical details and some experimental examples will be presented in Chapter 6. Nowadays the multipurpose "Surfmoss" system (see Figure 2.1d) permits to prepare the sample in a dedicated chamber as well as high pressure operations: the characterization procedures take place in the main chamber where the association of microscopy, spectroscopy and diffraction techniques provides a complete view of the sample properties.

2.2.1 Scanning Tunneling Microscopy

Scanning tunneling microscopy is an attractive technique developed by G. Binnig and H. Rohrer in the early eighties [17–19]. This is a widespread method that offers a direct real space imaging of solid surfaces with unique atomic resolution. The functioning concepts

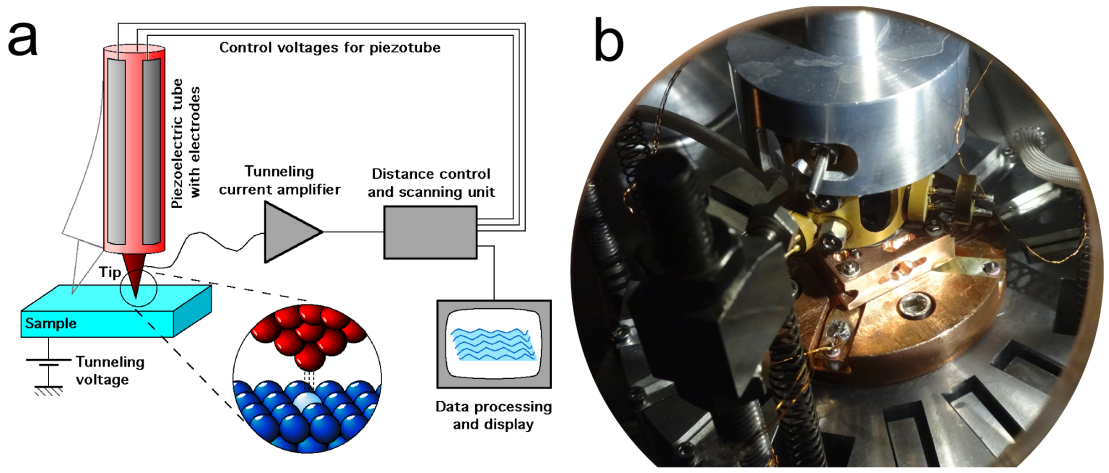

FIGURE 2.3: **a**. Schematic illustration of a common STM instrument adopted from Michael Schmid (TU, Wien) website. **b**. Detail view of the STM head resting on the sample holder. This photo has been captured at the "Surfmoss" chamber system.

are relative simple. When a metal tip is brought close enough to a conductor surface a so-called tunneling current is originated even though they are not in contact. This is due to the quantum-mechanical process of electron tunneling.

The tip is placed on a piezoelectric support, which allows microscopic displacements by applying a voltage at its electrodes. The microscope electronics control the tip position in such a way that the tunneling current is kept constant, while the tip is scanning a small area of the sample in two dimensions. The horizontal movements are recorded and can be displayed as a topographic image of the surface (see Figure 2.3a). The tunnel current I_t is a sensitive function of the sample-tip distance z, expressed by:

$$I_t \sim \exp\left(-Az\sqrt{\frac{\phi_s + \phi_t + V}{2}}\right) \tag{2.1}$$

where ϕ_s and ϕ_t are the sample and tip work functions, respectively and V is the applied bias. A is a constant which approaches to 1 when the ϕ value is measured in eV and z in Å. Because the I_t value changes by an order of magnitude for every angstrom change of z (with work functions of some eV), the depth resolution is in the sub-Å range (∼0.01 Å) [18].

As described in the introduction of Section 2.2, our microscope has been built [15] and mounted at our laboratory (Figure 2.3b). It has been coupled to a Nanonis electronics together with an Omicron MSCU coarse approach unit. The STM experiments have been carried out using a tungsten tip produced at our laboratory by the DC drop-off method [20]. All the images have been acquired at room temperature, tunneling at constant current mode with sample biases of -2/+2 V and tunneling currents of

0.3/10 nA. The Gwyddion software has been used for image treatment [21]. The images are usually displayed with the protrusions shown yellow and depressions black, their background has been corrected and in some cases image processing has been used in order to enhance the contrast.

2.2.2 Low-Energy Electron Diffraction

Low-Energy Electron Diffraction is a common tool to probe the long-range order of periodic surface structures [22, 23]. A commercial LEED diffractometer is constituted by an electron gun that generates a mono-energetic electron beam, a series of hemispherical grids, and a screen for the collection of the elastically scattered electrons. The electron beam that illuminates the sample has a typical energy varying between about 20 and 300 eV. Following the de Broglie equation:

$$\lambda = \frac{h}{m\nu} \tag{2.2}$$

the electron wavelength[1] is comparable with the inter-atomic distances and the interference of these waves with periodic surface lattices is expected. In this low-energy range the electron mean free path (see Figure 2.5) is so short that only the scattered electrons coming from the topmost layers contribute to the LEED measurement. Since diffraction occurs only when the surface structure satisfies the condition:

$$n\lambda = d\sin\alpha \tag{2.3}$$

where n is an integer value, λ the electron wavelength, d the in-plane periodicity (in one direction) and $\sin\alpha$ the angle between the incoming beam with respect to the scattered beam, the diffracted beams indicate the in-plane periodicity of those surface layers.

The 2-D atomic arrangement can be described by a pair of lattice vectors $\mathbf{a}_1$ and $\mathbf{a}_2$ which define the surface unit cell[2]. An example is given by the Figure 2.4a (left) where an hexagonal surface together with its unit cell are illustrated. Because the diffraction pattern can be related to a reciprocal lattice, two-dimensional Laue equations are used in order to derive the real-space lattice parameters. The relationship between the basis

[1] According with the De Broglie equation where m and ν are the mass and velocity of the particle and h is the Planck's constant, the wavelength for an electron beam with energy between 20 and 300 eV, varies from about 250 to 50 pm.

[2] The smallest unit that can be repeated to build up the whole surface.

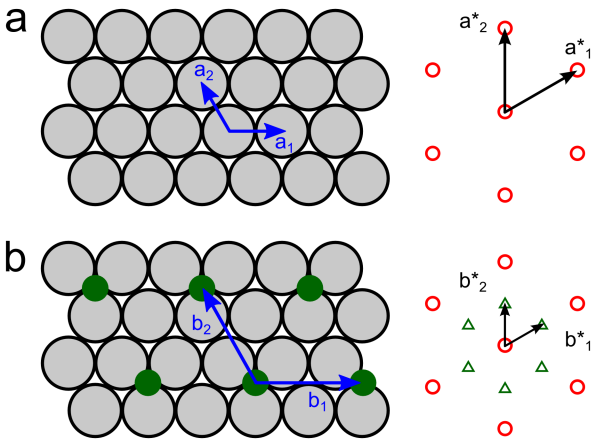

FIGURE 2.4: **a**. Schematic of the atomic arrangement of an hexagonal surface. The real-space (reciprocal-space) unit cell of the surface is defined on the left (right). **b**. Schematic of the atomic arrangement of (2×2) superstructure on an hexagonal surface. The real-space (reciprocal-space) unit cell is defined on the left (right).

vectors in reciprocal and real space is given by the equations:

$$\mathbf{a_1} \cdot \mathbf{a_1^*} = 2\pi \qquad \mathbf{a_2} \cdot \mathbf{a_2^*} = 2\pi \tag{2.4}$$

$$\mathbf{a_1} \cdot \mathbf{a_2^*} = 0 \qquad \mathbf{a_2} \cdot \mathbf{a_1^*} = 0 \tag{2.5}$$

If $\mathbf{a}_1$ and $\mathbf{a}_2$ are separated by an angle α the second equation 2.5 is only satisfied when the angle between reciprocal vectors $\mathbf{a}_1^*$ and $\mathbf{a}_2^*$ is (π - α). An schematic of the relationship between the real and reciprocal space for the common hexagonal surface is summarized in Figure 2.4a. Measuring the distance between the LEED spots (i.e. the reciprocal lattice vectors), it is possible to determine the atom arrangement in real space. Since the diffraction condition expressed in the equation 2.3, in a typical LEED pattern each diffraction spot coincides with the sum of integer multiples of $\mathbf{a}_1^*$ and $\mathbf{a}_2^*$ and is labeled using integer number (n_1, n_2).

An important benefit given by the extreme surface sensibility of LEED is the ability to study superstructures formed by absorbed atoms. Adsorbates or rearrangements of the surface atoms can lead to changes in the surface periodicity. In this case the unit cell differs from that of the ideal surface and its symmetry can be analysed studying the LEED pattern. A new set of lattice vectors $\mathbf{b}_1$ and $\mathbf{b}_2$ can be used to describe the new unit cell and the relationship with the original unit cell is given by:

$$\begin{aligned} \mathbf{b_1} &= m_{11}\mathbf{a_1} + m_{12}\mathbf{a_2} \\ \mathbf{b_2} &= m_{21}\mathbf{a_1} + m_{22}\mathbf{a_2} \end{aligned} \tag{2.6}$$

where the numbers m_{ij} are the coefficients of the superstructure matrix. A corresponding relationship in reciprocal space can be defined using the reciprocal lattice vectors:

$$\begin{aligned} \mathbf{b_1^*} &= m_{11}^* \mathbf{a_1^*} + m_{12}^* \mathbf{a_2^*} \\ \mathbf{b_2^*} &= m_{21}^* \mathbf{a_1^*} + m_{22}^* \mathbf{a_2^*} \end{aligned} \tag{2.7}$$

Applying the Laue equations (2.4,2.5) the relationship between the reciprocal and real space matrix can be obtained:

$$\begin{pmatrix} m_{11} & m_{11} \\ m_{11} & m_{11} \end{pmatrix} = \frac{1}{detM^*} \begin{pmatrix} m_{11}^* & m_{11}^* \\ m_{11}^* & m_{11}^* \end{pmatrix} \tag{2.8}$$

where M^* is the reciprocal matrix obtained from 2.7.

An example is illustrated in the left side of Figure 2.4b that shows a superstructure originated by an adsorbate. The right scheme of Figure 2.4b shows the reciprocal unit cells where the red dots indicate the position of diffracted beams corresponding to the initial (i.e. unreconstructed) surface while the adsorbed atoms give a set of additional spots as indicated by green triangles. According to the Wood notation[3], the superstructure is defined as (2×2) on hexagonal substrate.

If the adsorbate interacts weakly with the substrate, the lattice structure adopted from the new layer may be almost completely independent compared with that of the surface. In this case a complete new crystal structure is formed and the lattice vectors are irrationally related to the substrate unit cell. If an incommensurate adsorbed layer is formed on the substrate the combination between the two different periodicities can generate a set of new diffraction satellites (e.g. moiré pattern) around the substrate spots. Examples of this phenomenon are common in epitaxial growth and are easily investigated by LEED analysis. Although the LEED pattern gives information only about the in-plane unit cell, a complete structural determination is possible by means of LEED intensity versus energy (LEED-IV) analysis. Nevertheless, multiple-scattering calculations are necessary in order to interpret the LEED-IV data. Because we do not perform this application of the electron diffraction, we abstain from a more detailed explanation [25].

[3]Wood notation is frequently used in LEED analysis because it is shorter than the matrix notation [24]. This notation specifies the lengths of the $\mathbf{b}_1$ and $\mathbf{b}_2$ in units of $\mathbf{a}_1$ and $\mathbf{a}_2$. The rotational angle α between the two units cell is specified only if it is not zero. In LEED mode the notation is usually defined by the formula:
p / c $\left(\frac{|\,\mathbf{b}_1\,|}{|\,\mathbf{a}_1\,|} \times \frac{|\,\mathbf{b}_2\,|}{|\,\mathbf{a}_2\,|}\right)$ R α
where p and c indicates a primitive and a centered unit cell respectively.

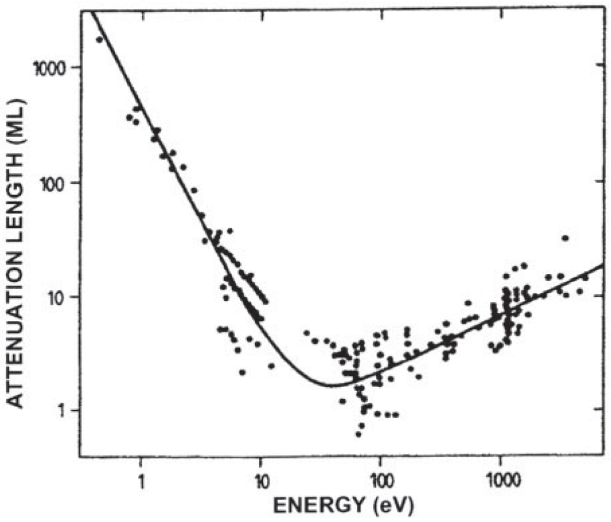

FIGURE 2.5: The Inelastic Mean Free Path (IMFP) curve shows the attenuation lengths (ML) of electrons in solids as a function of their energy (eV). The dots represent a set of experimental data while an interpolation formula is shown by the solid line. The image is reproduced from [1]

2.2.3 X-ray Photoelectron Spectroscopy

X-ray Photoelectron Spectroscopy (XPS), historically known with the acronym ESCA (Electron Spectroscopy for Chemical Analysis), is widely used to investigate the chemical composition of surfaces [2, 26, 27]. The technique was developed between the sixties and seventies by K. Siegbhan at the University of Uppsala, Sweden. XPS is based on the photoelectric effect and it is carried out by irradiating a sample with an x-ray beam and analyzing the energy of the emitted electrons. The x-ray photons penetrate the sample and interact with the atoms inducing electron emission by photoelectric effect (figure 2.6a). Due to the conservation of energy, the emitted electrons escape from the sample with a well-determined kinetic energy (KE), from which the binding energy can be extracted:

$$KE = h\nu - BE - \phi_s \tag{2.9}$$

where $h\nu$ is the photon energy, BE is the binding energy and ϕ_s is the spectrometer work function. The Binding Energy (BE) is XPS fundamental measure and it is approximately[4] the energy of the core-level from which the electrons come. Analyzing the kinetic energies and consequently the binding energies, photoemission peaks can be used to identify the elements present in the surface. Variations in the elemental binding energies, due to changes in the oxidation state or chemical environment (i.e., ligands), are called *chemical shift*.

[4] An approximation is needed because the intra- and extra-atomic relaxation events occur during the photoemission process modifying the electron binding energy.

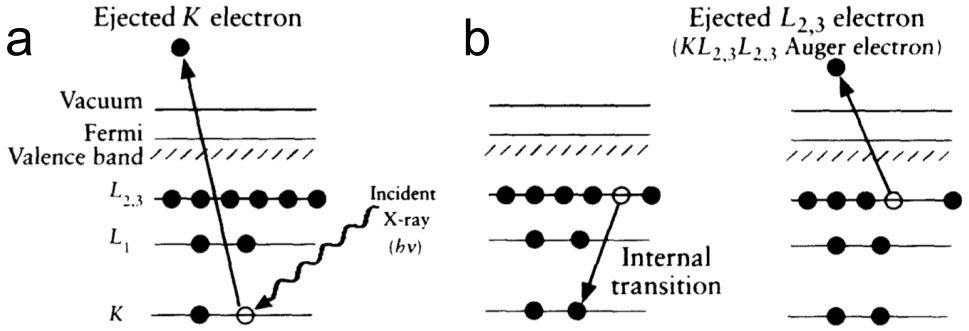

FIGURE 2.6: **a**. The XPS photoionization process for a model atom showing the ejection of a 1*s* electron induced by a photon absorption. **b**. Relaxation process of the ionized atom producing the emission of a $KL_{2,3}L_{2,3}$ Auger electron. Adapted from [2].

During the photoelectric process, Auger electrons are subsequently emitted due to the relaxation of the excited ions remaining after photoemission. In the Auger mechanism, a higher level electron fills the inner orbital hole, and a second electron is simultaneously emitted (Figure 2.6b). The kinetic energy of the Auger electron does not depend on the nature of the ionization source and it is approximately equal to the difference between the energy of the core vacancy (K in figure 2.6b) and the energy of the two outer electrons orbital ($L_{2,3}$ in figure 2.6b).

When the specimen is illuminated with an x-ray source, the radiation goes deep into the sample and ionization processes take place down to a depth of a few micrometers. However the mean free path of the electrons is limited according to the IMFP curve (Figure 2.5) and only those electrons that are originated within a few nanometers from the surface can be ejected without energy loss. These electrons contribute to the formation of the peaks in a typical XPS spectrum while the electrons that suffer inelastic loss processes produce the spectrum background. The kinetic energy of the electrons leaving the surface is determined by means of a hemispherical analyzer (HSA). The HSA works (see the schematics in Figure 2.7) as an energy filter so only electrons entering the analyzer with the appropriate energy will reach the detector. This energy can be expressed as:

$$E = e\Delta V \left(\frac{R_1 R_2}{R_1^2 - R_2^2} \right) \tag{2.10}$$

where E is kinetic energy, e is the electron charge, ΔV is the potential difference between the hemispheres and R_1 and R_2 are the radii of the outer and inner hemisphere respectively. Because the radii values are constant, the equation can be simplified as

$$E = ke\Delta V \tag{2.11}$$

where k is an analyser constant. In order to maintain a constant energy resolution $\frac{\Delta E}{E}$,

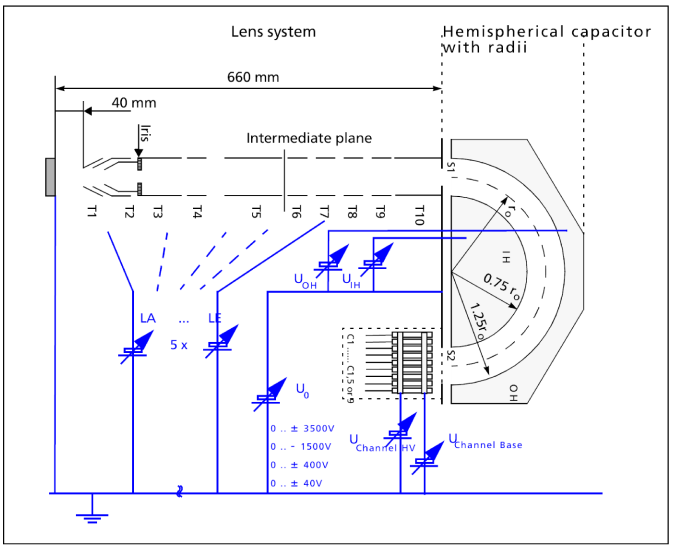

FIGURE 2.7: Schematics of the Phoibos 150 HSA main components. The schematics have been adapted from the SPECS^{TM} manual [3].

the energy that the electrons possess when they pass through the analyser, known as the pass energy, is fixed. Incoming electrons are accelerated or retarded to the pass energy before reaching the analyzer. Although small pass energy values provide higher resolution, the analyzer transmission decreases producing a lower count rate. The energy scanning is performed by applying a variable electrostatic field in an electrostatic lens system located before the analyzer entrance. This retardation voltage is varied from zero up to and beyond the photon energy. When the electrons reach the output plane of the analyzer they are detected by a series of electron multipliers (9 channeltrons in our setup, shown in Figure 2.7). The typical XPS spectrum is generated displaying the number of electrons for a given detection time versus the binding energy (see Figure 2.8).

The x-ray photoelectron spectrum

A typical XPS spectrum contains basically three kind of peaks. Two of them arise from the genuine photoemission processes and are usually denoted as *core-level* and *valence band* peaks. The third kind of peaks arise from Auger transitions occurring during the atomic relaxation subsequent to the photoemission process [27].

Core-level peaks give a direct representation of the electron configuration of the analysed atoms as described in the previous paragraph. Electrons coming from a s subshell produce a single peak while a doublet arises by electrons ejected from p, d, and f orbitals. The doublets are a consequence of the orbital degeneracy lifted by spin-orbit (S-O) coupling. The electron levels become separated in energy in two peaks when l>0 and are characterized by the number j (j = l + s). The relative ratios of the peak areas

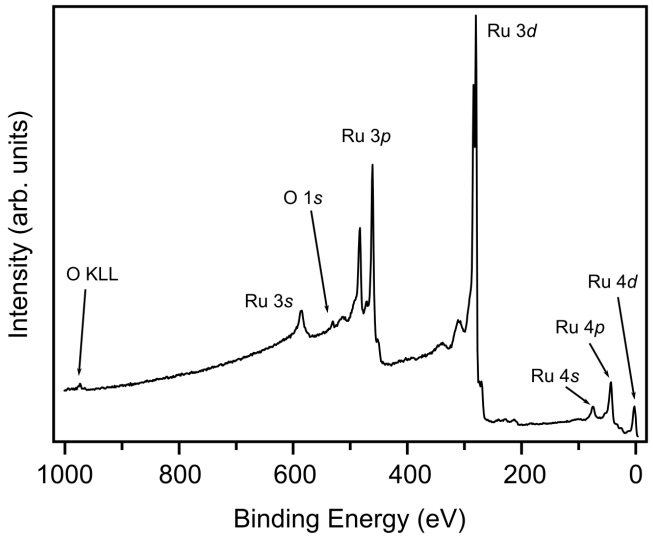

FIGURE 2.8: Survey XPS spectrum from the Ru(0001) substrate using Al K_α radiation. The peak assignment has been labeled.

TABLE 2.2: Spin-orbit splitting parameters

Orbital	j values	Area ratio
s	$\frac{1}{2}$	–
p	$\frac{1}{2}$, $\frac{3}{2}$	1:2
d	$\frac{3}{2}$, $\frac{5}{2}$	2:3
f	$\frac{5}{2}$, $\frac{7}{2}$	3:4

depend on the multiplicity of the corresponding electron state (2j + 1) and are given in Table 2.2.

Valence levels (or *valence band levels*) refer to the region at low binding energies (0–20 eV) which are generated by electrons ejected from de-localized or bonding orbitals. This region of the spectrum could be considered as fingerprint of the sample and consists of many closely spaced peaks giving rise to a band structure.

As explained in the previous section, *Auger series* rise from the radiationless decay mechanism taking place after the ionization processes. There are four main Auger series observable via XPS and they are KLL, LMM, MNN, NOO[5]. Because Auger peaks have a fixed kinetic energy, which is independent from the ionization source, they appear at different binding energies when the photon energy is changed (i.e. different anode material).

[5]The acronym identifies the initial and the final vacancy during the Auger transition according to the x-ray nomenclature.

Multiplet splitting and *shake-up satellites* are two example of typical secondary features that are commonly encountered.

Multiplet splitting of core-level peaks may occur when the compound presents unpaired electrons in the valence band. Emission of an electron from a core-level of an atom produces a vacancy. The coupling of the new unpaired electron of the core-level (s-type) with other unpaired electrons of the valence band can create a ion with several possible final state configurations and as many energies. This event produces a photoelectron line which is split asymmetrically into several components related to the several final configurations. Multiplet splitting effect can be observed also in the ionization of p levels but the result is more attenuated. In favorable cases, only a broadening of the p core-level peak is evidenced. *Shake-up satellites* have intensities and separations from the coupled core-level peak that are fixed to each chemical state. These peaks may appear when the outgoing photoelectron simultaneously interacts with a valence electron and excites it (*shake-up*) to an unoccupied higher-energy level. Thus, the core-level electrons experiment a slightly loss of kinetic energy giving a satellite structure a few electron volts below (but above on a binding-energy scale) the core level position.

2.3 Low-Energy Electron Microscopy

Low-Energy Electron Microscopy (LEEM) is a powerful technique developed by E. Bauer during the eighties [28–30]. This technique provides a real-space characterization of the sample surface. The fast acquisition time (in the millisecond range for a full frame) makes LEEM suitable for studying dynamical processes on surfaces: film growths, phase transitions, diffusion on surfaces, gas absorption or chemical reactions. The basic concept is relative simple: a crystalline sample[6] is illuminated by a monochromatic electron beam and the electrons reflected by the surface are collected forming a real space image of the surface. The typical LEEM instruments reach a lateral resolution of about 10–20 nm. Using a field emission electron source or, more recently, aberration correction (i.e., an electron mirror) the lateral resolution can be improved up to 2 nm. The instrumental aspects and experimental methodologies (i.e. alignment and operation) can be complex. Some they will be briefly discussed in the next subsection.

[6]Sample must be crystalline to give enough backscattered electrons.

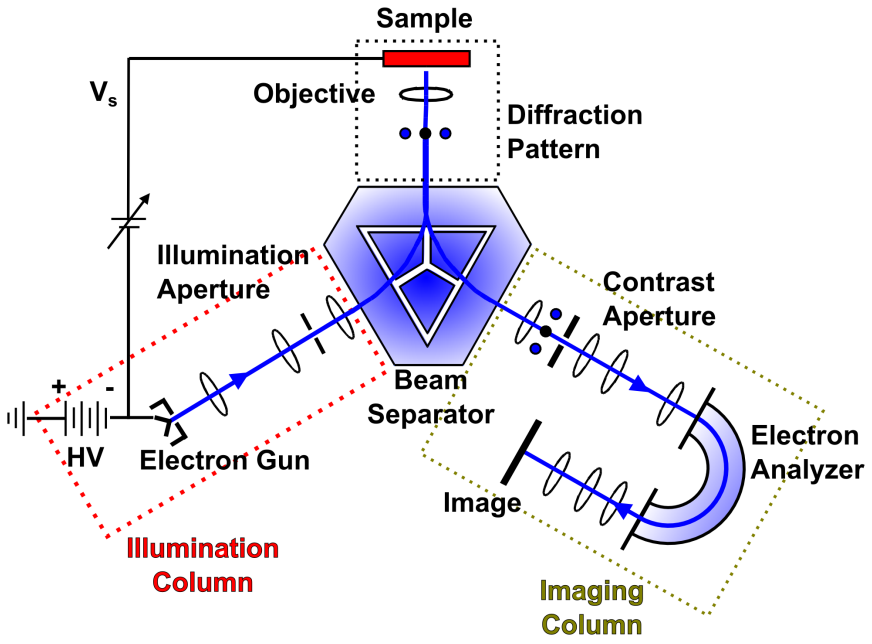

FIGURE 2.9: Simplified LEEM setup adapted from [4]. The electron beam (light blue line) generated in the illumination column is directed towards the sample surface (red rectangle). Reflected electrons are addressed oppositely to the imaging column. The image is generated when the electrons impinge the detector.

2.3.1 Experimental Setup

Figure 2.9 displays a schematic illustration of a LEEM microscope that consists in three fundamental parts: the illumination column, the beam separator and the imaging column. The electron beam is generated by an electron gun, often based on thermionic emission from a lanthanum hexaboride (LaB_6) crystal[7]. The emitted electrons are accelerated (up to 20 KeV[8]) and directed through the illumination column where a series of condenser lenses provide a parallel beam. Usually the beam has a diameter of several micrometers (10–100μm) and a set of illumination apertures are installed into the illumination column in order to reduce the illumination area on the sample.

A magnetic field created by the beam separator bends the electron beam in such a manner that the electrons arrive perpendicular to the sample surface. Before reaching the surface, the incoming electrons are decelerated passing through a strong electrostatic field created by the objective lens and the sample itself. Commonly the typical landing energy varies from 0 to 100 eV and it is called start voltage (S_v). After scattering from the sample the reflected beam is accelerated back into the objective lens in such a way that a diffraction pattern is formed in the lens back-focal plane.

[7]For the LaB_6 the minimum energy spread is 0.8 eV [2].
[8]The accelerating voltage (E) is maintained in a range between 15 and 20 kV to maximize the lateral resolution [31].

The electron beam passes through a sequence of lenses that allows to focus the real-space or the diffraction pattern and to magnify the resulting image. After the last imaging lens, the electron beam is amplified by a micro-channel plate detector before stopping on the phosphor screen. The image on a phosphor screen is collected by a CCD digital camera located outside the vacuum chamber. The image column is usually equipped with an aperture (*contrast aperture*) that allows to block most of the diffraction plane except for a selected diffracted beam.

Additionally a hemispherical imaging energy analyzer can be mounted in the imaging column. This energy filter allows considerable benefits during LEEM or LEED experiments because it avoids to image the usually unwanted inelastically emitted electrons. The hemispherical imaging energy analyzer is a fundamental part of the photoemission electron microscopy mode (see section 2.4).

It is important to remark that LEEM works only in ultra-high vacuum condition[9] in order to avoid electric arcs between the different parts of the microscope, and due to the requirement of clean, controlled surfaces.

2.3.2 Methods

In a LEEM microscope images are originated by several contrast mechanisms arising from the interaction of low-energy electrons with the sample surface. In a typical LEEM experiment the contrast aperture selects the specular diffraction spot (0,0) which is used to form the real-space image of the surface. This imaging method is also called *bright-field* and is likewise the most common operation mode in transmission electron microscopy (TEM). An example is presented in figure 2.10a in which a $Fe_3O_4(001)$ surface is shown. In the image a dislocation, with an out-of-plane Burgers vector, produces a series of spiral terraces (ligh gray areas) separated by steps 2.1 Å high (darker gray lines). The step contrast arises from phase contrast [32]. It is caused by Fresnel diffraction between electron waves reflected at the upper and lower part of the step.

In Figure 2.10b an image of Ru(0001) covered by bilayer-thick FeO(111) islands is shown. In this case the different contrast of the island is originated by a variation in the surface composition. The incoming electrons interact differently with the band structure of distinct materials producing changes in the electron reflectivity. In a first approximation (single scattering) the amount of reflected electrons would be associated with the electronic structure of the surface: when the density of available unoccupied electron states

[9] The illumination and imaging columns are housed in particular chambers maintained at $\sim 10^{-10}$ Torr. They communicate to the main chamber through a small aperture (several mm). The sample is located in the main chamber where a differential pumping system permits working under pressures in the 10^{-6} Torr range while keeping the electron gun and the detector system at UHV.

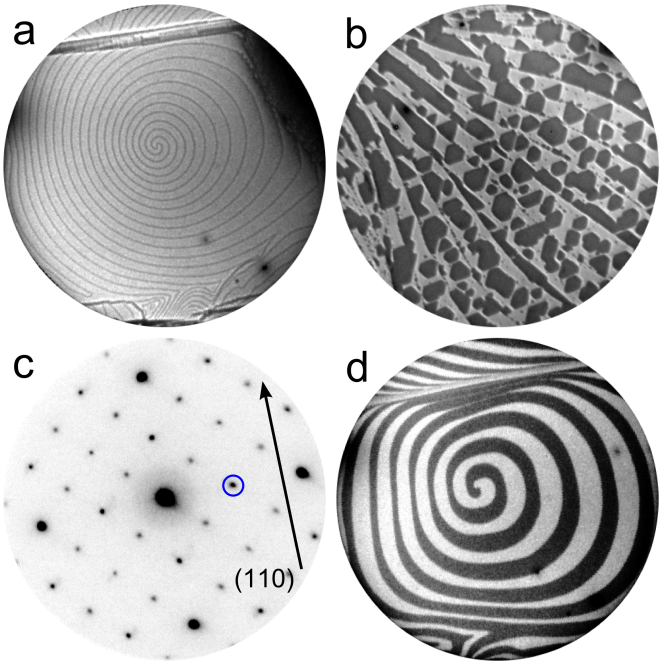

FIGURE 2.10: Examples of LEEM methods. **a**. *Bright-field* image of a $Fe_3O_4(001)$ spiral around a screw dislocation. The field of view is 20 μm and the S_v=10.8 eV. **b**. Image of FeO(111) islands (dark gray) covering a Ru(0001) surface (light gray). The field of view is 10 μm and the S_v=19.5 eV. **c**. LEED pattern showing a c(2×2) symmetry relative to the (1×1) symmetry of a $Fe_3O_4(001)$ surface acquired at 30 eV. **d**. *Dark-field* image of the same area of figure a using the blue circled LEED spot (1,0) in figure **c**. The field of view is 20 μm and the S_v=10.8 eV.

is low, the reflectivity value is high and viceversa. Moreover electron scattering processes can be used to measure the density of absorbed adatoms on the sample surface [33, 34]. If electrons are scattered by the absorbed atoms away from the specular beam direction, a decrease in electron reflectivity of the specular beam takes place.

LEEM microscopy allows achieving diffraction analysis as shown in Figure 2.10c. In LEED mode, the contrast aperture is removed and the diffraction plane is imaged by adjusting the imaging column lens. Reducing and choosing the illuminated area with the illumination aperture allows selected area diffraction measurements (μLEED). The LEED pattern then comes from a precise region of the surface making this operation mode an attractive LEEM improvement. Another advantage is given by the LEEM design which permits measuring the specular beam or its satellites, usually forbidden in a conventional diffractometer at normal incidence (as the specular beam is hidden by the electron gun). Thanks to the functioning of the objective lens [4], the LEED spots do not move towards the center when the beam energy is increased, contrary to what happen at a traditional LEED diffractometer. Figure 2.11 shows a comparison between different LEED patterns collected using a conventional diffractometer (a and c) and a LEEM microscope (b and d). In the first case the diffraction spots move towards the center of the screen when the beam energy increases allowing the detection of the

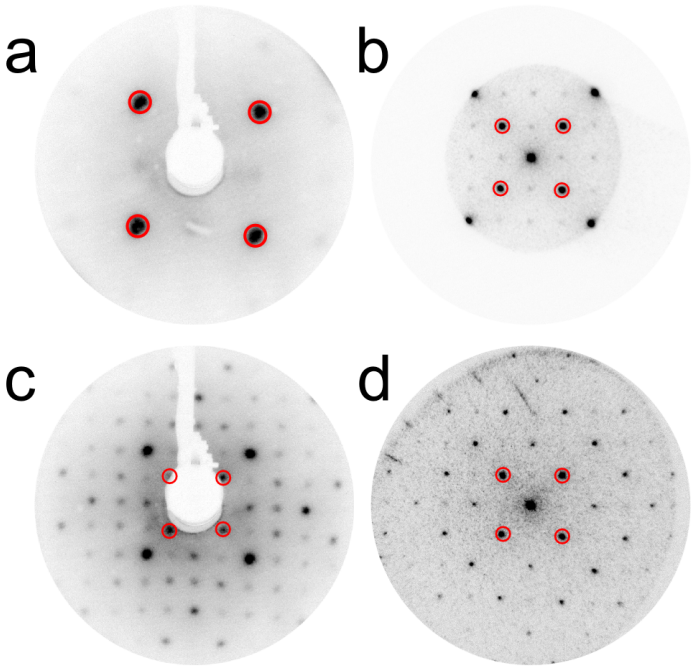

FIGURE 2.11: Examples of diffraction pattern obtained using a conventional LEED instrument (**a** and **c**) and a LEEM microscope (**b** and **d**). The LEED patterns have been collected from $Fe_3O_4(001)$ surface at 20 ev (a,b) and 100 eV (c,d). The first order spots have been indicated by red circles.

second and third order spots, while in the latter case the spots do not move and the the observed reciprocal space is usually limited to the second Brillouin zone.

By properly deflecting the illumination or the reflected beam, a diffraction spot different from the specular one can be used and a *dark-field* image results. This imaging mode is very advantageous because the real-space image is originated only from the part of the surface characterized by the selected diffraction spot (i.e. the selected structure). The *dark-field* mode allows to extract information from a surface with distinct structure domains, even if those structures are below the regular resolution limit of the microscope. An example is given in Figure 2.10d where a *dark-field* LEEM image of a $Fe_3O_4(001)$ is presented. The surface is composed of a spiral around of two types of terraces in which a distinct atom arrangement originates from a two-fold symmetry [35]. In Figure 2.10d, the bright areas corresponds to the terraces where the structure forms the selected diffraction spot (blue circle in Figure 2.10c).

2.4 X-ray Photoemission Electron Microscopy

In surface science, synchrotron-based x-ray photoemission electron microscopy (XPEEM) is one of the most important spectro-microscopy techniques [36–38]. By taking advantage of the tunability and polarizability of synchrotron radiation, XPEEM instruments can be used to carry out several x-ray spectroscopic investigations with a unique lateral resolution. X-ray absorption spectroscopy (XAS), x-ray photoelectron spectroscopy (XPS), and x-ray magnetic circular (or linear) dichroism (XMCD-XMLD) are some examples of the XPEEM capabilities. The combination with low-energy electron microscopy converts PEEM into a surface scientist's "ace in the hole" in which real-space imaging, diffraction and spectroscopy techniques are combined in a unique instrument.

The x-ray photoemission electron microscope is based on an analogous idea to the low-energy electron microscope (2.3). While LEEM works using the reflected electrons from an electron beam, XPEEM images a specimen collecting photoelectrons generated by x-ray radiation. It should be noted that the XPEEM of the Nanospectroscopy beamline differs from standalone XPEEMs since it is equipped with an illumination electron beam, i.e., LEEM and XPEEM capabilities are combined in a unique instrument.

In XPEEM, the sample surface is illuminated[10] with a synchrotron beam producing photoelectrons (see Figure 2.6). These electrons are accelerated by a strong electrostatic field in the objective lens creating a magnified image of the surface. The image containing information about the surface chemical composition is transferred to a two dimensional electron detector by a sequence of lenses. Likewise in LEEM, the image is recorded with a CCD camera.

The XPEEM microscope offers a series of spectroscopic techniques that can be divided in two groups. The first one is based on photon-induced electron emission where the emitted electrons have the characteristic energies of the elements in the sample. This method requires an energy filter, often an hemispherical electron analyzer located in the imaging column. The second group is based on the absorption of photons with energies characteristic of the material studied. In this case the energy filter is still necessary in order to improve the spatial resolution (PEEM suffers strong chromatic aberrations, so you get a blurred image otherwise).

We have to note that XPEEM, unlike LEEM, does not require a crystalline sample.

[10] In the Nanospectroscopy beamline setup the incoming x-ray beam forms an angle of 16° respect with the surface normal.

Methods

Several methods are included in the first group. Some examples are XPS imaging, selected area XPS or x-ray photoelectron diffraction (XPD). In order to carry out these techniques, the sample is illuminated with photons of fixed energy and the pass energy of the energy analyzer is scanned to obtain an energy-resolved spectrum of the photoelectrons. Example of an application of these techniques is illustrated in Figure 2.12 where the chemical properties of an ultra-thin film of a Bi/Fe/O compound has been investigated by XPEEM. Using the microscope in LEEM mode a real-space image of the surface showing irregular islands with different contrast is obtained (figure 2.12a). In order to get chemical information about the composition of the surface an XPS spectrum has been collected employing photoelectrons ejected from the selected area of Figure 2.12a (*selected area XPS*). The resulting Bi 4 $f_{\frac{7}{2}}$ spectrum shows two peaks corresponding to different Bi chemical states: metallic Bi at 157.0 eV and Bi^{3+} at 159.5 eV. At this point, *XPS imaging* mode has been applied to understand the island composition and the origin of each Bi signal. Two different images have been collected selecting only electrons with kinetic energies corresponding to the two XPS peaks maximum. Composing the resulting images, a picture with chemical sensitive contrast is produced (see Figure 2.12c) in which the light green contrast is given by metallic Bi while the red contrast corresponds to Bi^{3+}.

The second group of techniques employs x-ray absorption. XPEEM is used to measure the secondary electron emission during a photon-energy scan. When the photon energy matches a core level energy, the secondary emission intensity increases. This process results from the transition of core-level electrons into unoccupied band levels. Due to the large mean free path of the secondary electrons used (0–10 eV), XAS can be sensitive to the last ∼5 nm of the sample.

X-ray absorption frequently depends upon the orientation of the E vector of the electromagnetic radiation with respect to the sample. This *dichroic*[11] process is on the base of two special modes of XAS imaging: XMCD and XMLD. X-ray magnetic circular dichroism (XMCD) is a well-established method to probe the magnetic properties of ferromagnetic 3d transition elements. During the excitation of 2p electrons using circular polarized radiation the angular momentum ($\pm\ \hbar$) is transferred from the photon to the spin of the excited electron which is used to probe the unoccupied 3d levels in the spin-split valence band. During this process the secondary emission is proportional

[11] In optics, dichroic is usually referred to a material that does not adsorb equally a light beam having different polarizations.

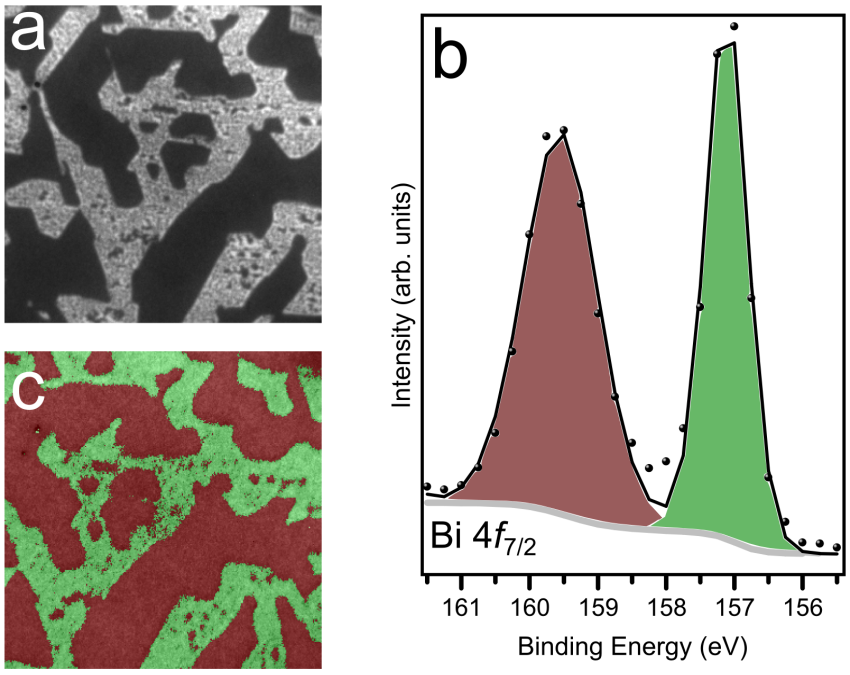

FIGURE 2.12: Examples of PEEM methods. **a**. LEEM images of ultra-thin film of mixed valence Bi compound on Ru(0001). The field of view is 2.8μm^2 and the S_v=54 eV. **b**. XPS Bi 4 $f_{\frac{7}{2}}$ spectrum collected from the entire area of figure a. The photon energy is 400 eV. **c**. Composite color image obtained from the superposition of two XPS images collected at 157 and 159.5 eV binding energy, respectively. The green contrast is relative to the metallic Bi signal (157 eV) while the red contrast is related to the Bi^{3+} (159.5 eV). The image represents the same region that figure a, the field of view is 2.8μm^2 and the photon energy is 400 eV.

to the dot product between the magnetization direction and the photon helicity vector. Consequently, local differences in the orientation of the in-plane magnetization[12] originate differences in the adsorption intensities which are used to image the magnetic domains. By collecting two XAS images using opposite beam helicities and calculating the pixel-by-pixel asymmetry, an XMCD image is obtained:

$$I_{XMCD} = I_{minus} - I_{plus} \tag{2.12}$$

In a typical XMCD image the magnetic domains with a magnetization component along the photon beam direction appear bright or dark while those aligned perpendicular to the beam direction appear grey.

The second dichroism-based technique is x-ray magnetic linear dichroism (XMLD). While XMCD uses circular polarized radiation in order to induce a photoelectron emission, XMLD works with horizontal and vertical linear polarization of the photons. XMLD is widely used in the characterization of antiferromagnetic materials.

[12]In the used XPEEM, due to the incidence angle between the x-ray beam and the sample surface, XMCD measurements are sensitive mostly to the in-plane component of the magnetization vector.

2.5 Sample Preparation and Details

All the presented results were obtained three different laboratories using different systems. At Sandia National Laboratories (Livermore, California) LEEM experiments have been carried out using a commercial Elmitec LEEM III microscope under the supervision of Kevin F. McCarty. The LEEM-PEEM experiments have been done at the Nanospectroscopy beamline of Elettra Synchrotron (Trieste, Italy) managed by Andrea Locatelli. The Nanospectroscopy beamline operates a commercial Elmitec SPELEEM III microscope [38]. The beamline at the third–generation synchrotron facility is served by a high photon flux beamline characterized by elliptically polarized photons in the range 50 eV to 1000 eV[13]. Finally, the "Surfmoss" system at the Instituto de Química Física "Rocasolano" (Madrid, Spain) was used for the STM, LEED and XPS measurements.

The experimental methods used for the development of this thesis were based on an *in situ* approach. This means that the samples have been prepared and characterized without exposure to an external environment (i.e. the samples have been maintained in UHV condition).

Commercial Ru(0001) crystals has been selected as substrate for all the experiments and typical UHV protocols have been used in order to clean the surface from impurities. Although it is maintained in UHV condition, the Ru crystal has carbon dissolved in the bulk that segregates to the surface forming graphene. It was usually cleaned by exposure to molecular oxygen (10^{-8} Torr range) at 900 K followed by rapid flashes at 1500–1600 K. If the Ru(0001) is completely covered by one or more atomic layer of carbon, an Ar^+ sputtering process is applied in order to promote the successive oxidation reaction. Flashing and annealing procedures were accomplished by electron bombardment where a white–hot W filament is biased at negative potential (1.0 KV) to the sample.

Iron oxides samples were prepared using home-made iron evaporators allowing the iron sublimation from a rod heated by electron bombardment. The evaporators that were designed and mounted during the thesis consist in a pure iron rod surrounded by a W filament (0.15–0.25 mm in diameter) placed within a water cooling jacket. Electron emission is obtained by applying filament currents in the 3/5 A range and the emitted electrons were extracted and accelerated from the filament to the iron rod using a 1.0–1.2 kV voltage. The electron emission is usually adjusted manually by changing the filament current in order to obtain acceptable sublimation rates. The iron flux varied from 3×10^{-4} ML s^{-1} to 5×10^{-3} ML s^{-1}.

[13] More information about the beamline description and specifications are available from the Nanospectroscopy beamline website [39]

The Fe doser was calibrated by measuring the time needed to complete an Fe monolayer on Ru(0001)[14]. This calibration procedure has been carried out using both STM and LEEM microscopes. The Fe doses and oxygen coverages are given in ML_{Fe}, defined as the ratio of Fe or O atoms to Ru(0001) surface atoms. The Fe fluxes have been measured before and after the experiments, and the change in the rate appears to be less than 10%.

The ultrathin films have been prepared by either a two-step preparation or direct oxygen-assisted deposition. The two step method consists in iron deposition at room temperature in UHV followed by oxidation operated at a temperature ranging between 800 K and 920 K in an O_2 background pressure between 1×10^{-8} and 5×10^{-6} Torr. In the direct oxygen-assisted deposition (O–MBE), the Ru(0001) has been maintained at a temperature varying from 800 K and 910 K and metallic Fe has been deposited in a background O_2 pressure (10^{-8}–10^{-6} Torr range). Because during the gas dosing the values of emission current change, they were kept constant by increasing the filament current. We assume that the iron flux does not change while the oxygen was introduced in the UHV system.

Additionally, if a stronger oxidation agent is needed, the thin film was annealed in a nitrogen dioxide (NO_2) atmosphere obtained by introducing the pure gas in the main chamber. In fact, NO_2 pure gas is a convenient precursor for atomic oxygen and allows efficient oxidation at near-UHV pressures, because it rapidly undergoes dissociation producing NO and atomic oxygen [41, 42]. Although this oxidizer presents several disadvantage (i.e., NO_2 is toxic by inhalation and favors the H_2O production when abundantly dosed inside the UHV chamber), it has been selected in order to obtain iron oxides of higher oxidation state. We remark that NO_2 was not used for the growth of iron oxide (NO_2-assisted MBE) in order to prevent the substrate oxidation [43, 44].

[14]The density of the first Fe layer under our growth conditions is the same as the underlying Ru, i.e., the growth is pseudomorphic [40].

Chapter 3

FeO(111) on Ru(0001)

3.1 Introduction

FeO wüstite crystallizes in the sodium chloride structure including four formula units in the cubic unit cell [12]. Oxygen anions form a close-packed fcc sublattice where the iron cations are inserted interstitially. FeO contains only Fe^{2+} cations that are octahedrally coordinated to O^{2-} anions. This iron oxide cannot exist as a stable phase at ambient conditions and wüstite usually exhibits a large deviation from stoichiometry expressed using the $Fe_{1-x}O$ formula[1]. This latter phase can be synthesized only at temperatures greater than 840 K. Below this temperature it disproportionates to metallic Fe and Fe_3O_4 [12]. The cubic lattice constant ranges from 4.28 to 4.31 Å depending on the iron vacancy content. When a vacancy ordering is experimented by FeO, the formation of magnetite-like clusters take place[2]. Along the ⟨111⟩ direction, wüstite consists of alternating layers of Fe^{2+} cations and O^{2-} anions, each arranged in an hexagonal lattice (see Figure 3.1). The O (111) planes form the cubic ABC stacking sequence with an interlayer distance of 2.5 Å. The interatomic distance between these planes is 3.04 Å which corresponds to the lattice constant of the hexagonal unit cell of each plane, as indicated in Figure 3.1a. The Fe–O bond length is 2.16 Å. Wüstite is paramagnetic at room temperature and exhibits antiferromagnetism below 203–211 K, when the electron spins become ordered ferromagnetically within the each (111) plane and the different (111) planes are coupled antiferromagnetically. The FeO Néel temperature depends on the concentration of defects in the structure.

FeO ultra-thin films were grown for the first time by Vurens *et al.* [46, 47] and its growth on metal substrates has been extensively studied for more than two decades. Although

[1] (1-x) value varies from 0.83 to 0.95 depending on the O_2 partial pressure and temperature [45].
[2] Magnetite is a more oxidized iron oxide that will be the subject of next chapter.

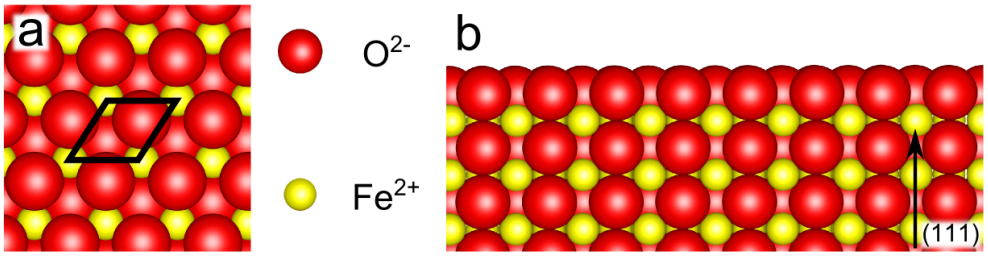

FIGURE 3.1: **a**. The top view of FeO(111) surface cut exposing a close-packed O plane. The surface unit cell is indicated. **b**. Side view of FeO(111) showing the same bulk truncated (111) structure terminated by an oxygen plane. Fe and O (111) planes forming the cubic stacking sequence of FeO(111) are visible.

interest in the FeO film was initially focused on heteroepitaxy [13] and the study of bulk iron oxide surface properties, the scientific community has more recently been attracted by the novel properties exhibited by FeO synthesized in ultrathin film form [48]. Because an ultrathin film consists of just a few atomic layers, often it manifests structural and electronic properties different from the bulk counterpart. Very recently it has been demonstrated experimentally and theoretically that FeO(111) nanometer-size islands supported on Pt(111) are much more active for low temperature CO oxidation[3] than clean Pt(111) [49–54]. Additionally, it has been proved that the enhancement effect of FeO thin films on platinum-based catalysts also influences other reactions, including the oxygen reduction reaction (ORR) [55] and the water-gas shift (WGS) reaction [56–58]. These facts disagree with the observed inactivity of oxygen-terminated FeO(111) surfaces toward different adsorbates [13, 59, 60] and raise the debate about the role of catalytically active sites in these type of oxide-on-metals systems. Structural defects and unsaturated sites are frequently suggested to be active centers responsible for a large variety of chemical reactions [25, 61]. In consequence different groups started to study and discuss the importance of coordinatively unsaturated ferrous (CUF) centers in the FeO(111) nanostructures supported on metals [48, 62–65]. It has been demonstrated that these CUF sites are confined to the periphery of the FeO nanoislands at the interface with the metal substrate [62] and enhance the catalyst activity by bonding to absorbed molecules and undergoing easily electron transfer processes.

The enhanced catalytic effects of FeO(111) supported on metals have been additionally attributed to a charge transfer between the metal substrates and the oxide nanostructures [49, 53, 66]. These mechanisms, usually considered for transition metal oxides, consist in the so-called strong metal-support interaction (SMSI) between metals supported on oxides. Introduced by Tauster *et al.* [67, 68], SMSI was associated with the formation of bonds between the noble metal and the oxide cations, the latter involving the formation of intermetallic compounds. Although SMSI has been studied in detail

[3]Preferential oxidation of CO in hydrogen atmosphere, (PROX)reaction.

in the last two decades, the discussion about its role in heterogeneous catalysis is still open [51, 69]. Therefore, it is conceivable that the promotional effect observed on these inverse catalysts[4] arises from a mutual cooperation between the formation of CUF sites and the SMSI effect.

The understanding of the role of FeO in these catalytic reactions and the ability to prepare precise FeO nanostructures become crucial aspects that stimulate the study of FeO growth and its properties on different substrates. Ultrathin FeO films were prepared on metal substrates such as Pt(111) [13, 70–72], Pt(100) [73], Cu(001) [74], Ru(0001) [40, 75–79], Au(111) [61, 80] or on oxide surfaces such as MgO(001) [81], and Y-stabilized ZrO_2(100) (YSZ) [82]. Usually, FeO has been grown using separate steps of depositing an ultrathin iron film at room temperature followed by oxidation at ∼900 K in a molecular oxygen atmosphere. The iron has been evaporated using molecular beam epitaxy (MBE) which allows to control the dosing rate precisely avoiding surface contamination. The sequence of deposition and oxidation can be repeated if thicker films are desired [13]. An alternative growth method is that based on oxygen-assisted molecular beam epitaxy (O–MBE), where the oxide is obtained by depositing iron in a background pressure of molecular[5] oxygen [84]. Using O–MBE, the surface is covered with a layer of chemisorbed oxygen before Fe arrives at the surface. Natural questions are then whether the two methods (MBE *vs* O–MBE) produce the same structures and morphologies and what factors control the growth of the FeO film.

In this chapter we study the initial stages of FeO(111) growth on Ru(0001). We begin by characterizing different FeO ultrathin films prepared using the conventional MBE method and comparing them with those produced by O–MBE. The FeO ultrathin film have been studied by STM, XPS and LEED and they exhibit similar chemical and structural properties. However, we find that the O–MBE growth is strongly controlled by the O_2 background pressure and the FeO film produced can be bilayer[6] in height, unlike the monolayer islands typically produced at the initial stage of Fe oxidation. To understand why FeO bilayers or monolayers are produced, we use LEEM to image the surface in real space monitoring the film growth. We propose that the oxygen coverage on the Ru(0001) drives whether single or bilayer growth mode takes place. Finally, by analyzing the temperature dependence of the FeO island nucleation density, we estimate the activation energy for surface diffusion of the Fe-O growth species [79].

[4] FeO nanostructured supported on noble metal surfaces.

[5] Atomic oxygen can be produced using a oxygen plasma generator. The technique is called oxygen-plasma-assisted molecular beam epitaxy (OPA–MBE) [83].

[6] In the following discussion, a perfect FeO(111) monolayer (ML) is referred to one Fe and one O atomic layer.

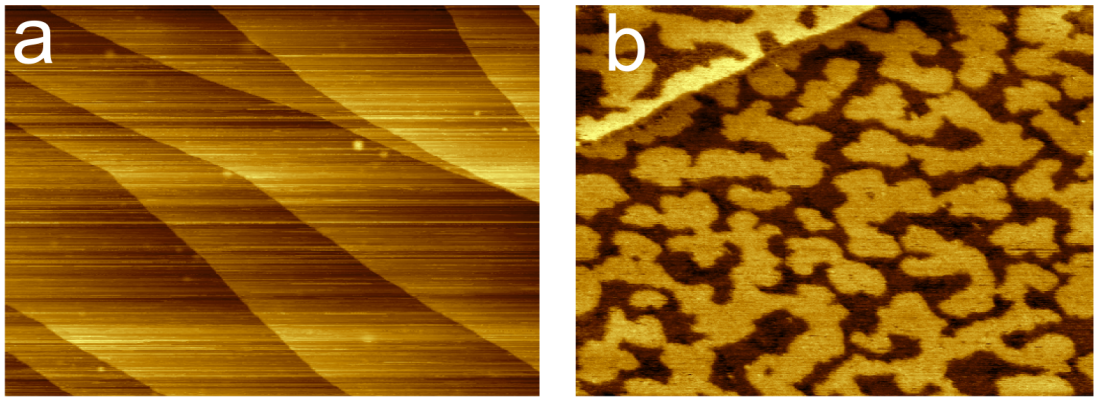

FIGURE 3.2: **a**. 500×365 nm^2 STM image of clean Ru(0001) surface in which mono-atomic steps separated by 2.7 Å are visible (I_t=0.9 nA and U_b=+1.33 V). **b**. 150×112.5 nm^2 STM image of 0.6 ML of Fe on Ru(0001) collected at I_t=8.3 nA and U_b=-0.49 V.

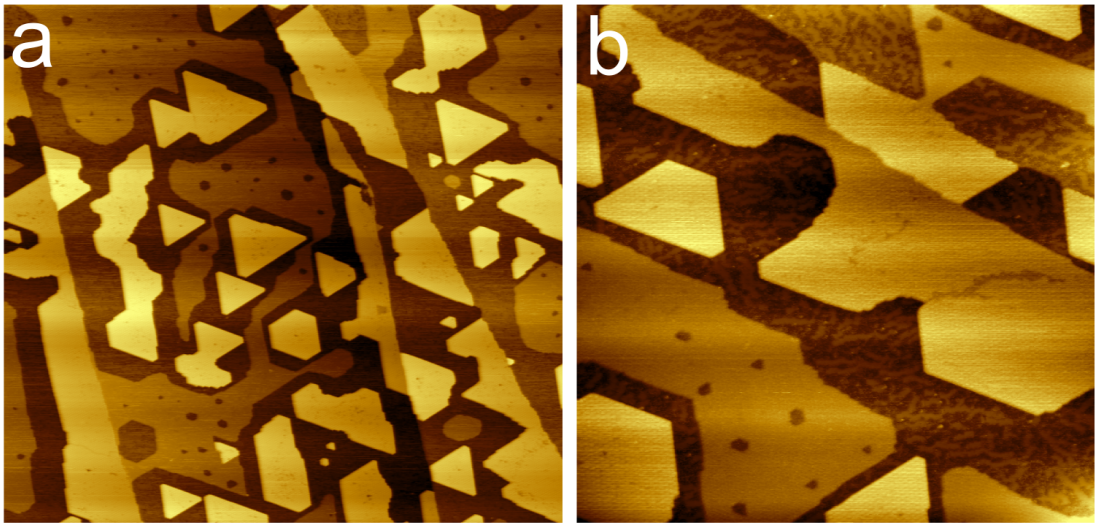

FIGURE 3.3: STM images displaying two different Ru(0001) regions covered by FeO(111). The surface consists of regular islands (2 ML of FeO) surrounded by a thinner layer (1 ML of FeO). Bright regular islands are 5.0 Å high while the surrounded areas have a thickness of 2.5 Å. **a**. 500×463 nm^2 image with I_t=1.9 nA and U_b=+0.81 V. **b**. 200×200 nm^2 image with I_t=1.0 nA and U_b=+1.00 V.

3.2 Growth of FeO(111) on Ru(0001) by MBE

We begin by characterizing a FeO film grown by depositing iron on Ru(0001) and oxidizing it afterwards by annealing in molecular oxygen atmosphere. In Figure 3.2a an STM image of a clean Ru(0001) surface after the cleaning procedures is shown. Several terraces separated by atomic steps are visible and the typical graphene contamination is absent (also confirmed by XPS and LEED, not shown). The measured step height is ∼2.14 Å which agrees with the distance between consecutive ruthenium terraces. Figure 3.2b shows an STM image of the Ru(0001) covered with 0.6 ML of Fe grown at

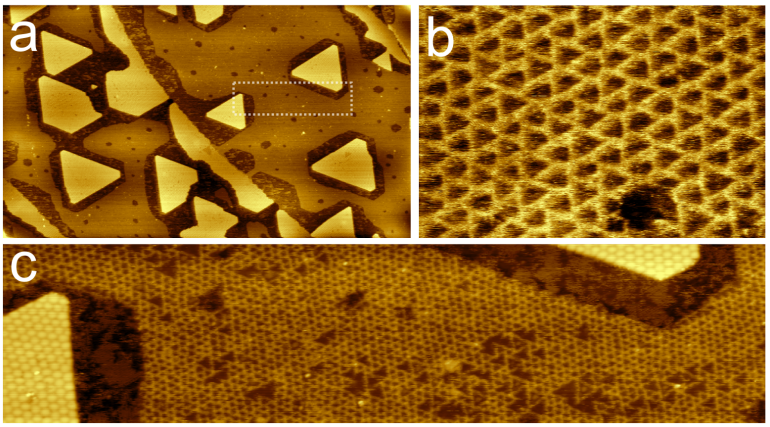

FIGURE 3.4: **a**. 500×285 nm^2 (I_t=0.6 nA and U_b=+1.10 V) STM image displaying Ru(0001) surface covered FeO(111). The surface consists of two-layer thickness islands (bright) surrounded by a thinner layer (one layer). **b**. 19×13.4 nm^2 STM image of the thinner layer showing regular triangular features (I_t=9.6 nA and U_b=-1.10 V). **c**. 150×35 nm^2 STM image of the region marked by a white box in Figure a (I_t=1.1 nA and U_b=+1.10 V).

room temperature in UHV. The deposition has been carried out at room temperature in order to avoid Fe/Ru alloying [85]. Irregular iron islands with a thickness of ∼2.0 Å and a width of tens of nanometers nucleate randomly on the terraces at these growth conditions. The diffraction measurement (not shown) presents a (1×1)–Ru(0001) pattern without additional spots which suggests that the structure of the layer is pseudomorphic with the Ru(0001) substrate [85].

In Figure 3.3 we show STM images of a film of FeO obtained by oxidation of 0.7 ML of Fe at 820 K and p_{O_2}=2×10^{-6} Torr. The surface is covered by two regions that exhibit different contrast (i.e. different thickness). While the step height of the thicker region is ∼5.0 Å, the thickness of the thinner region is ∼2.5 Å. These values agree with the interlayer distances previously reported for FeO [75–77]. According with this, thicker triangular shaped islands occupying 25% of the surface consist of two layers of FeO, while the thinner region covering irregularly a 50% of the surface is formed by 1 ML of FeO.

In Figure 3.4, the STM images show some details about the 1 ML region. While the 2 ML triangular islands exhibit an ordered structure, the top-most layer of the thinner region is characterized by the presence of triangularly shaped features. We tentatively assign the latter to a defective FeO layer due to the lack of oxygen during the oxidation step. In fact, these features on the FeO(111) surface have previously been interpreted as oxygen vacancy dislocation loops [5, 86].

Upon prolonged oxidation by repeating the previous oxidation step several times, the 2 ML islands grow in size and number (Figure 3.6a) and the 1 ML regions disappear.

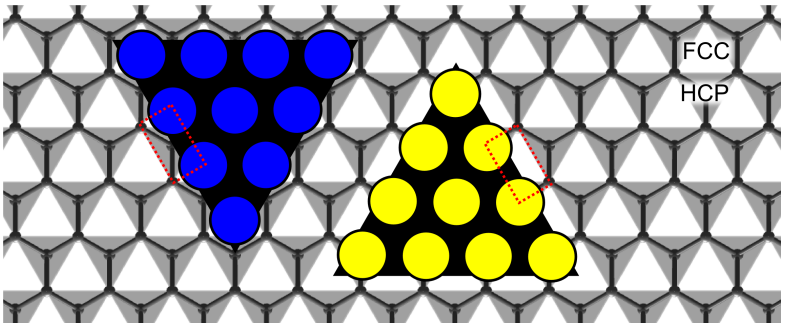

FIGURE 3.5: Ball model of the Ru(0001) surface. Two adatom islands nucleated on *regular* fcc and stacking-faults hcp sites have been depicted in blue and yellow, respectively. In the stacking-faulted island the step geometry (represented by a red dashed line) is maintained by the its rotation of 180° with respect to the regular fcc island.

As no further iron has been deposited during this step, the growth of the bilayer islands can only explained by "eating up" the monolayer FeO areas. The 2 ML FeO islands nucleate with a regular triangular shape and oriented along the compact directions of the Ru(0001) substrate. The triangles often exhibit the same orientation within the same terrace while they are rotated by 180° with respect to the islands in the adjacent terrace. This fact was previously observed on heteroepitaxial growth of metals on metal substrates and extensively discussed [87]. It was interpreted by invoking the influence of the hcp substrate in which consecutive terraces having opposite atomic orientations (180°-rotated) drive the orientations of the nucleated islands [88, 89].

Observing Figure 3.6a, an island is shown which is oriented in the opposite direction of most islands in the same terrace and touching an island with different orientation. A detail of the region between the two islands is shown in Figures 3.6b–c. The difference in the island orientation can be explained using the same arguments proposed for heteroepitaxial and homoepitaxial metal growth [87]. Figure 3.5 shows the presence of two possible nucleation sites in the Ru(0001) surface: fcc or hcp. Assuming the islands exhibit an equivalent geometry (i.e. equivalent crystallographic direction of the edges), those islands nucleating on the *erroneous*[7] absorption site (yellow balls in Figure 3.5) are rotated by 180° with respect to regular islands (blue balls in Figure 3.5), giving rise to a stacking fault on the former [90].

The nucleation probability of the "wrong" absorption site depends on the film/substrate combination, or can be induced by foreign adsorbates. A shift in the atomic rows would be expected if the islands have different stacking. Nevertheless, no such shift was detected using the high resolution STM image 3.6c. Thus, we are confronted with the paradox of islands with opposite orientations that seem to have the same stacking. We

[7]Since we do not have experimental determination of the preferred nucleation site, we have arbitrarily assuming that the *erroneous* site is the hcp in Figure 3.5.

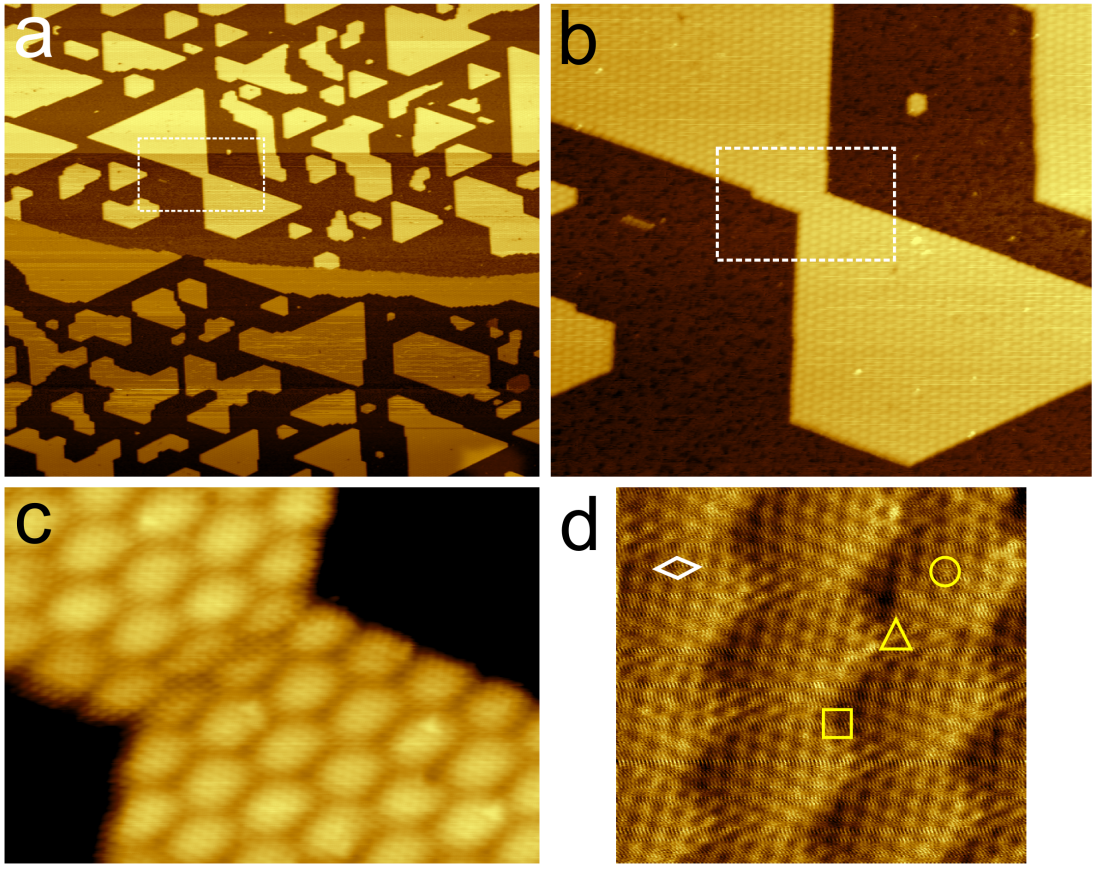

FIGURE 3.6: **a**. 400x352 nm^2 STM image of FeO(111) islands on Ru(0001). The regular islands are composed by two layer of FeO(111) and the thickness is 5.0 Å (I_t=2.9 nA and U_b=+0.90 V). **b**. 100x87 nm^2 STM image of the contact region (white box in a) of two FeO(111) triangular islands (I_t=2.9 nA and U_b=+0.90 V). The two triangular islands located in the same terrace are rotated 180° degrees oppositely to each other. **c**. High-resolution STM image (15x10 nm^2, I_t=10.4 nA and U_b=+0.39 V) of a detail marked with a white box in b. The ordered FeO(111) moiré pattern ("7 on 8" coincidence structure) is visible. **d**. Atomic resolution STM image of the upper island (5.8x5.3 nm^2, I_t=10.4 nA and U_b=+0.39 V). The moiré superstructure shows a periodicity of 22.2 Å and the unit cell of the FeO(111) film showing a lattice constant of 3.2 Å is marked in white . The location of the high-symmetry domains is indicated by the symbols:(□)FCC, (△)HCP, and (◯) TOP [5].

anticipate from the next section that further growth experiments using LEEM will help to solve this paradox (Section 3.3).

The two merged islands exhibit the same regular corrugation. The corrugation (i.e. moiré pattern) visible in the STM images (Figures 3.6b and c) has a periodicity of 22.2 Å and appears well-ordered. The lattice constant (see Figure 3.6d) is 3.2 Å. The atomic arrangement results from the coincidence of 7 FeO with 8 Ru atoms ("7 on 8" coincidence structure) [75]. The surface unit cell is slightly expanded compared with the FeO bulk value (3.04 Å). This in-plane relaxation presumably takes place in order to reduce the electrostatic surface dipole [91]. Summarizing, STM images confirm the formation of a well-ordered ultrathin film constituted by 2 ML of FeO(111).

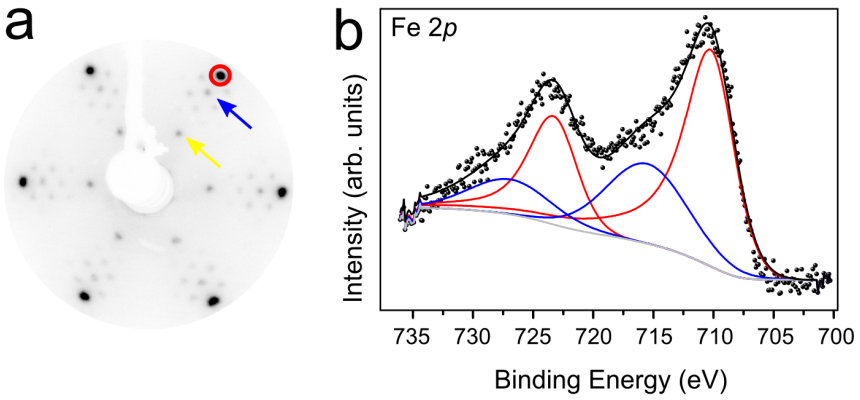

FIGURE 3.7: **a**. LEED image collected from one layer of FeO(111) on Ru(0001) at 50 eV. The diffraction pattern exhibits two series of hexagonally arranged spots: the brighter (1×1) structure marked with a red circle corresponds to Ru(0001) while a blue arrow marks that spots corresponding to the FeO(111). The FeO(111) diffraction spots are surrounded by *rosettes* of weak satellite spots. (2×2) hexagonal spots originated by ordered oxygen atoms chemisorbed on Ru(0001) surface are marked with a yellow arrow. **b**. Fe 2 *p* core-level XPS spectrum acquired from FeO. The experimental spectrum (black dots) has been fitted using a black solid line originated from the sum of the contribution of the main photoemission peaks (red) and the shake-up satellites (blue).

In order to confirm the long-range order of the FeO(111) film, the LEED pattern has been recorded. The assignment of the spots and the LEED pattern itself are displayed in Figure 3.7a. The brighter hexagonally arranged spots marked by the red circle correspond to the Ru(0001). (2×2) spots are originated from the chemisorbed oxygen as result of the exposure of Ru(0001) surface to molecular oxygen (yellow arrow in Figure 3.7a). The first-order diffraction spots marked by the blue arrow in the figure exhibit a separation that corresponds to an atomic spacing consistent with the measured on FeO(111) films by STM (3.2 Å). The satellite spots around the first-order spots can be explained by multiple scattering between the FeO(111) film with the Ru(0001) substrate or in terms of diffraction at the moiré structure observed in the STM images [75].

The Fe 2 *p* XPS spectrum acquired after the oxidation of a Fe ultrathin film is quite complex (Figure 3.7b). Its shape resembles quite closely that reported for the surface of bulk FeO [92] or FeO films [13, 93]. We fitted it considering a genuine photoemission spin-orbit doublet with binding energies of 709.9 eV (Fe $2p_{3/2}$) and 722.7 eV (Fe $2p_{1/2}$) with a FWHM value of 4.3 eV (red lines in Figure 3.7b). To account for the broadening due to multiplet splitting which is known to occur in the XPS spectrum of FeO and other iron oxides [94] we have used a large FWHM and added an asymmetry to the main photoemission peaks. It is also well-known that Fe^{2+} compounds show an intense shake-up satellite structure above (∼6.0 eV) the main photoemission lines [7, 92, 94]. These satellites are quite evident in the present case and were fitted with two peaks at

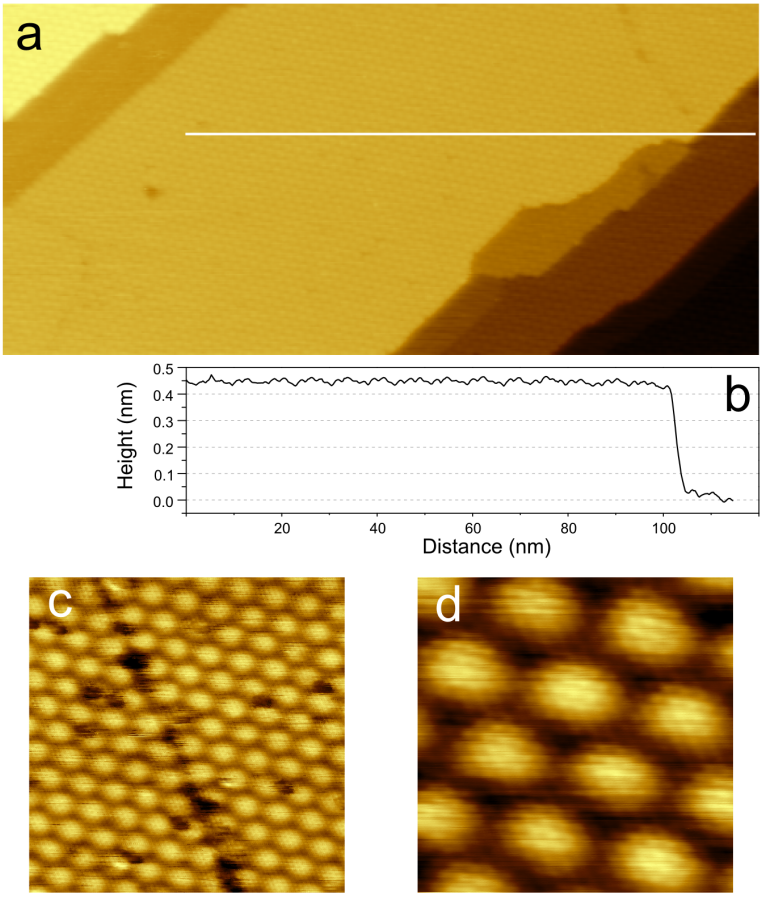

FIGURE 3.8: STM images of FeO(111) grown by O–MBE. **a**. Large-area STM image a bilayer film (147×70 nm^2, I_t=2.1 nA and U_b=+1.55 V). **b**. Profile along the white line in Figure a. **c**. (20×20 nm^2) STM image of the FeO moiré superstructure with a periodicity of 21.6 Å. A trench defect can be observed. (I_t=6.6 nA and U_b=+0.61 V) **d**. High resolution STM image of the FeO bilayer showing a surface unit cell of 3.4 Å (6 nm×6 nm, I_t=15.6 nA and U_b=-0.24 V).

715.1 eV and 726.2 eV (blue lines in Figure 3.7b). Additionally, the spin-orbit splitting energy (12.8 eV) approaches to values reported for the FeO phase [7, 92, 94].

3.3 Growth of FeO(111) on Ru(0001) by O–MBE

In this section the characterization of FeO(111) films grown by depositing iron on a hot substrate in an oxygen atmosphere is presented. Using STM, XPS and LEED measurements, we show that these films are structurally and chemically equivalent to the previous FeO(111) grown by further oxidation of iron metal ultrathin films. In Figure 3.8 several STM images are presented in which a film has been grown by oxygen-assisted MBE by exposing the substrate at 850 K to an Fe flux of 1.5×10^{-3} ML s^{-1} in 10^{-6} Torr of oxygen. The large-area STM image (Figure 3.8a) shows a nearly complete iron oxide film, which exhibits the typical FeO moiré superstructure. Figure 3.8c reveals

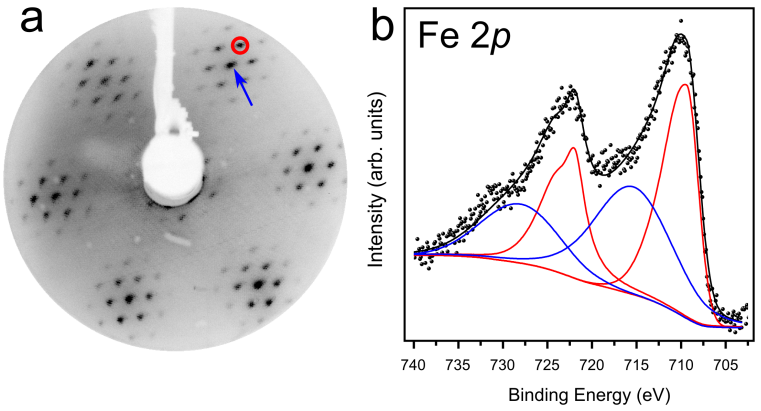

FIGURE 3.9: **a**. LEED and XPS from FeO(111) grown by O–MBE. In the pattern at 50 eV the Ru spots are marked with a red circle while the FeO with a blue arrow. **b**. Fe $2p$ core level spectrum. The experimental data (dots) has been fitted with $2p_{1/2}$ and $2p_{3/2}$ photoemission peaks (red lines) and *shake-up* satellites (blue lines).

an in-plane periodicity of 21.6 Å which agrees with those values observed on FeO grown by the two step preparation method [75, 76]. In the same Figure, localized defects are evident forming dark patches in the FeO superstructure. These irregularities have been observed in the FeO(111) grown on metals [13, 75] and have been interpreted as local atomic vacancies. A trench that has been observed in Figure 3.8c, can been interpreted as the merging of two FeO islands in which moiré superstructures were not aligned with each other. The measured thickness ($\sim$ 0.45 nm) is in reasonable agreement with the formation of a bilayer film of FeO on top of the Ru substrate (Figure 3.8b). Using the atomically resolved image (Figure 3.8b), the distances between the observed protrusions have been measured showing a surface unit cell (3.4 Å) that agrees reasonably with the value observed previously on FeO.

The LEED pattern presented in Figure 3.9a contains first-order spots whose separation (3.14 Å) is consistent with the values obtained by STM and with those values exhibited in the previous experiments (Figure 3.7a). The satellite spots around the first-order spots interpreted as FeO fingerprints are also evident.

Additionally, the Fe $2p$ XPS spectrum has been collected in order to determine the iron oxidation state. The spectrum reported in Figure 3.9b resembles quite closely that reported for the FeO(111) film grown by oxidation of an iron film (Figure 3.7b). We fitted it considering a photoemission spin-orbit doublet with binding energies of 709.5 eV (Fe $2p_{3/2}$) and 722.1 eV (Fe $2p_{1/2}$) and a linewidth of 4.0 eV. To account for the broadening due to multiplet splitting, we have added an asymmetric line shape two to the peaks. The shake-up satellite structures above the main photoemission lines are quite evident again and were fitted with two peaks at 715.8 eV and 728.6 eV.

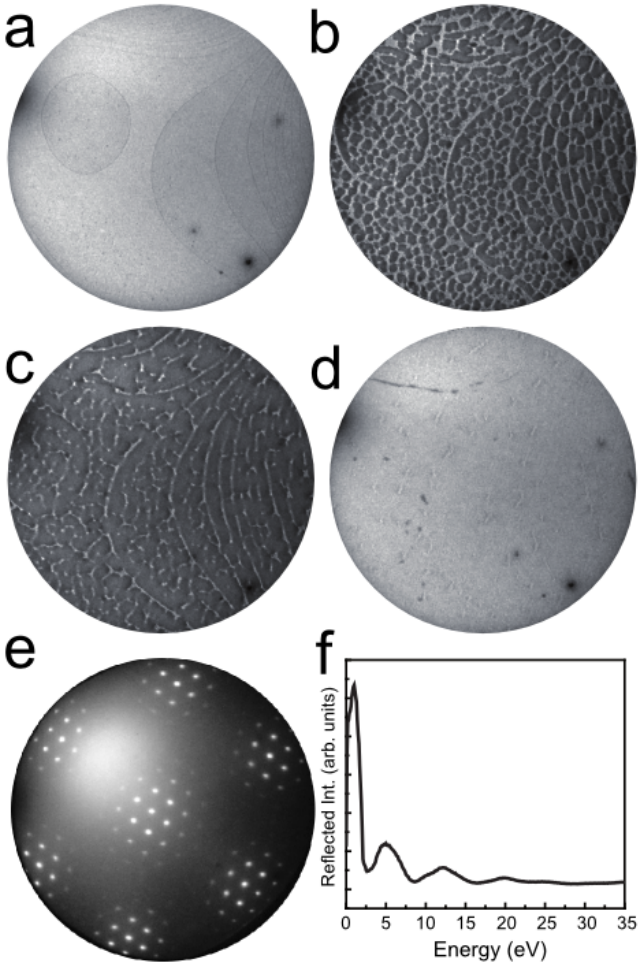

FIGURE 3.10: Growth of FeO(111) in 10^{-6} Torr oxygen at 800 K. **a**–**d**. LEEM images extracted from a sequence acquired in real time during iron oxide growth (after +0,+354,+574 and +938 seconds, respectively). The image field of view is 10 μm. The electron energy is 19.4 eV. Total amount of iron deposited is 1.4 ML_{Fe}. The dark lines in image a correspond to atomic steps of the Ru substrate. The FeO islands correspond to the dark regions in images b and c. In d the surface is covered by a nearly complete layer. **e**. LEED pattern of the final surface acquired at 42.3 eV. **f**. Electron reflectivity versus electron energy collected from the obtained surface.

In summary, all the techniques employed indicate that the FeO films grown by O–MBE are both structurally and chemically the same as those grown by sequential steps of Fe deposition and oxidation studied in the previous section 3.2. We anticipate that the formation of Fe_3O_4 has been observed also by O–MBE at later stages of the growth and it will be specifically treated in the next chapter.

Figure 3.10a–d show LEEM images collected during O–MBE growth of FeO. Ru(0001) steps are visible in the initial clean surface (see Figure 3.10a). Then oxygen is dosed in the chamber and the O_2 absorption process produces, at the electron beam employed, a decrease in the local electron reflectivity that darkens the image (not shown). When the oxygen density on the surface saturates (i.e. the reflected intensity reachs a plateau),

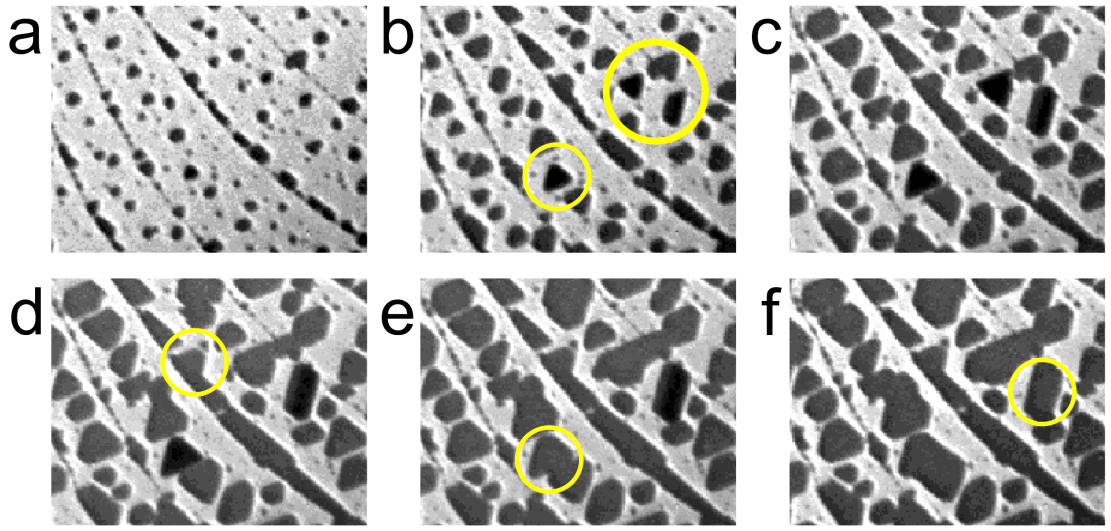

FIGURE 3.11: Growth of FeO(111) by O-MBE. **a**–**f**. LEEM images extracted from a sequence acquired in real time during iron oxide growth (after +41, +49, +57, +63, +66, and +68 seconds, respectively). The image field of view is 4.2x3.3 μm^2 and the electron energy is 19.0 eV.

iron deposition is started. The Fe atoms land on the surface, react with the oxygen and iron oxide islands nucleate both on the terraces and along the Ru(0001) steps (see dark areas in Figure 3.10b). The islands grow in size (Figure 3.10c) until they coalesce in a continuous film which covers the substrate (Figure 3.10d). The diffraction measurements obtained by LEEM (Figure 3.10e) reveal that the film is formed by FeO(111) and are in agreement with those recorded using a conventional diffractometer (Figure 3.9a).

In Figure 3.10f the change of the electron reflectivity[8] of the FeO surface with the electron energy has been depicted. This is measured by integrating the intensity of a selected area in a sequence of LEEM images acquired by scanning the incoming beam energy. The zero energy refers to the sample and the electron gun field at the same potential. These measurements at low energies have been referred to as very-low energy electron diffraction, VLEED [95]. Because the electron reflectivity is related to the unoccupied density of states of the surface, it can be used as a fingerprint of a given film or substrate [4]. In particular, we note that the observed curve is not only observed on FeO(111)/Ru(0001) systems [78] but also on FeO(111)/YSZ [82] and is very different from that of Fe/Ru(0001), (see Figure 8 of Ref.[40]). Given the total amount of iron deposited for a complete film (1.4 ML$_{Fe}$) and the difference in lattice spacing between metallic iron and FeO(111), the prepared film should be 2 ML$_{FeO}$ thick. As the images show only one stage of island nucleation followed by growth, we conclude that the islands initially nucleated under a O_2 pressure of 10^{-6} Torr are composed of two layer of FeO(111). This evidence is in agreement with the previous STM studies (Figure 3.8).

[8]The electron reflectivity can be understood as the intensity of the diffraction specular beam.

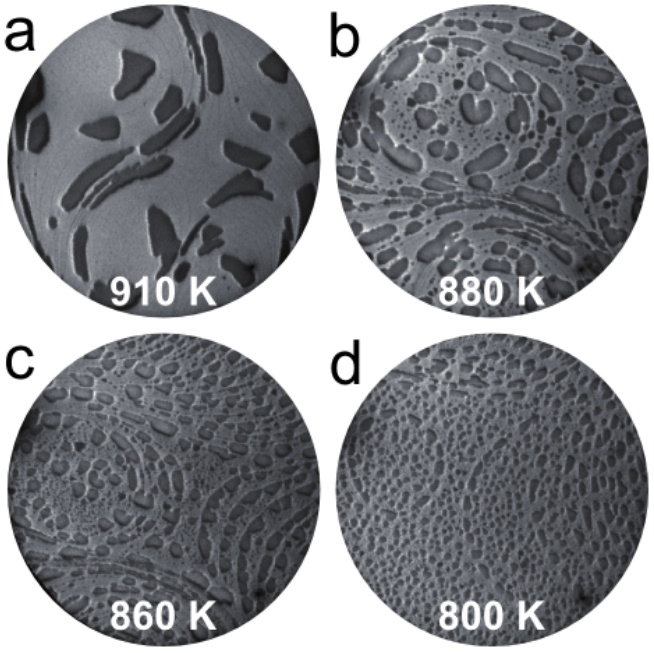

FIGURE 3.12: **a**–**d**. LEEM images acquired during the FeO growth at the labeled substrate temperatures. The images have been selected from each sequence to clearly show the differences in nucleation density. For each image the field of view 10 μm, the oxygen pressure is 10^{-6} Torr and the electron energy is 19.4 eV.

By monitoring by LEEM the initial stages of the FeO growth, we have been able to interpret the paradox of the FeO islands with different triangular shape albeit with the same stacking sequence (see Section 3.2). As shown in Figure 3.11a, LEEM images acquired during growth at Elettra LEEM, clearly show the nucleation of triangular FeO islands[9]. Those islands with opposite orientation within the same terrace, (see yellow circle in Figure 3.11b) exhibit a different contrast, i.e., the contrast is correlated with the stacking, assuming that the island shape reflect the stacking sequence. This correlation in reflected intensity has been observed in metal systems such as Co/Ru [96] or Ag/Ru [97]. But by monitoring the growth, we observe that these darker islands change their contrast when they merge with adjacent islands without changing shape (see Figure 3.11d, e, and f). This suggest that the stacking fault in the "wrong" island can be changed during growth. In fact, this removal of stacking faults during growth has been reported for metal heteroepitaxy, by Ling and co workers [97]. Summarizing, when an "erroneous" island is growing, its stacking fault can be healed by merging with a "regular" island.

According with this argument, we can explain the absence of atomic row shifts in the island with "wrong" orientation in Figure 3.6. Since it is touching another adjacent island most probably the stacking fault has been eliminated.

[9]That the shape is more triangular than in most experiment performed at the Sandia LEEM might be related to the slightly worse vacuum conditions [87]

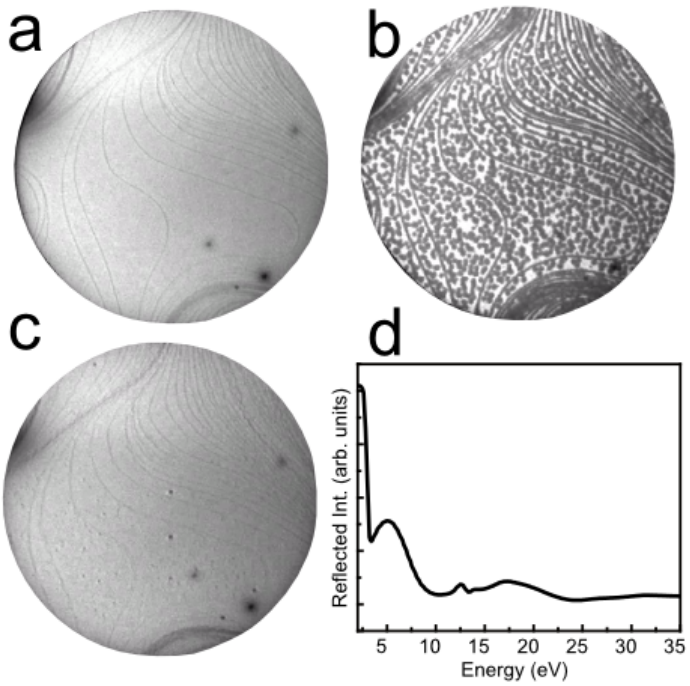

FIGURE 3.13: **a**–**c**. LEEM images of FeO film grown by OMBE at 10^{-8} Torr. Total amount of iron deposited is 0.75 ML_{Fe} (the time elapsed is +0, 262 and 514 seconds, respectively). In the final frame c, the surface is covered by a complete layer that has not altered the original substrate morphology. Sample temperature is 800 K. Field of view is 10 μm and electron energy is 18.3 eV. **d**. Reflectivity as a function of energy from the final film.

3.4 Influence of Temperature and Oxygen Pressure

In this section, we study the effect of temperature and oxygen pressure on FeO growth by O–MBE. As reported in the previous section, Fe deposition in 10^{-6} Torr of O_2 produces the nucleation and growth of bilayer-height islands which eventually coalesce covering the substrate completely. This phenomenon appears not to be affected by the substrate temperature in the range studied (800–910 K). However, temperature strongly influences the island densities, as shown in Figure 3.12. While at 910 K there are 3.4×10^7 islands cm^{-2}, at 800 K the island density increases to 1.3×10^9 islands cm^{-2}. At higher temperatures, the island nucleation is mostly located at the substrate step edges.

Oxygen pressure has a strong influence on both island height and nucleation density. First, we discuss the effect on the island height. Figure 3.13 shows growth at lower O_2 background pressure, 10^{-8} Torr. At first glance, the image sequence seems to be similar to growth at the same temperature (800 K) but higher pressure (10^{-6} Torr, Figure 3.10): islands nucleate and then grow until they cover the surface. But there is a important difference between them: while a complete FeO film is formed after dosing 1.4 ML_{Fe} at 10^{-6} Torr, only ~0.7 ML_{Fe} is necessary to produce a closing film

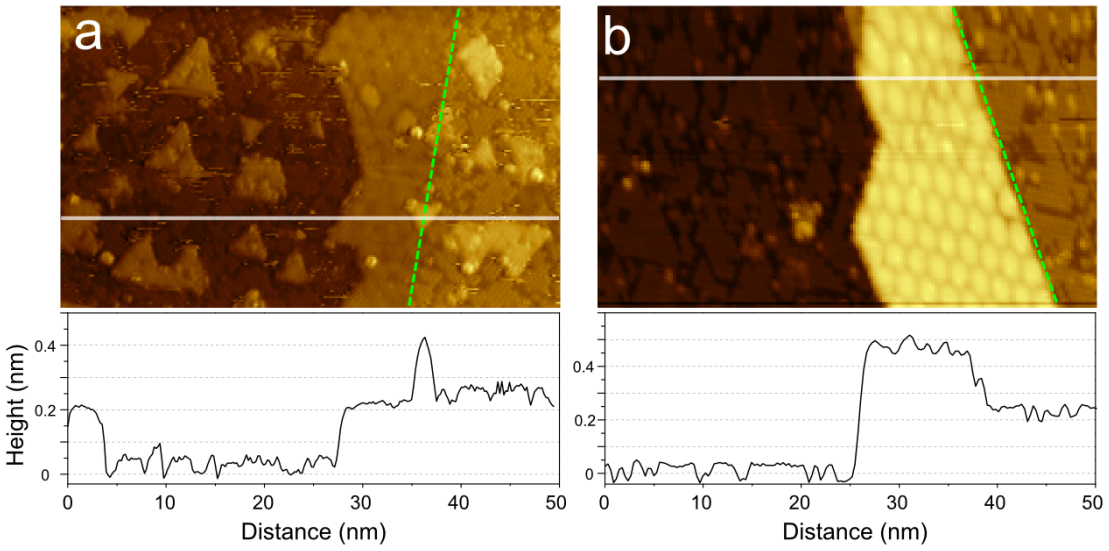

FIGURE 3.14: STM images of FeO grown by OMBE under two different pressures: **a**, Under 5×10^{-8} Torr O_2 (I_t=1.2 nA and U_b=+1.6 V), and **b**, under 7×10^{-7} Torr O_2 (I_t=1.0 nA and U_b=+2.0 V), respectively. Both images are 50 nm×30 nm in size. In both, a green dashed line marks the location of the monoatomic Ru substrate step, and the cross section between successive terraces (white lines) are shown below.

at 10^{-8} Torr. Furthermore, the electron reflectivity curves from the films grown at each different pressure are quite different (compare Figure 3.10f and Figure 3.13d), indicating the different nature of the two films. Considering the difference of lattice spacings of pseudomorphic Fe and FeO, the coverage for complete films corresponds to ∼2 ML_{FeO} and ∼1 ML_{FeO} for 10^{-6} Torr and 10^{-8} Torr, respectively. Thus, the LEEM results indicate that the mechanism of FeO growth is strongly influenced by the O_2 background pressure, monolayer-height islands nucleate at lower pressure and bilayer-height islands are obtained at higher pressure.

The evidence of the pressure effect is directly proved by STM measurements. In Figures 3.14, STM images have been collected from initial O–MBE growth at 5×10^{-8} Torr (a) and 7×10^{-7} Torr (b). The difference in island height as a function of pressure is observed in the profiles under each image. In Figure 3.14, corresponding to a pressure of 5×10^{-8} Torr, islands are observed both on the Ru terraces and wetting the downward side of the Ru monoatomic step showing a thickness of 0.22 nm. In contrast, for higher pressures (7×10^{-7} Torr), FeO islands are two layer height (they appear higher than both the lower Ru terrace and the upper terrace on the right side of the image). Additionally, patches of a (2×2) structure are present on the Ru substrate presumably corresponding to adsorbed oxygen.

The study of the oxygen pressure dependence has been concluded analyzing the FeO growth at 10^{-7} Torr. At intermediate pressures, the nucleation mechanism is more complex, as shown in Figures 3.15. Although the islands start to grow in bilayer mode, they

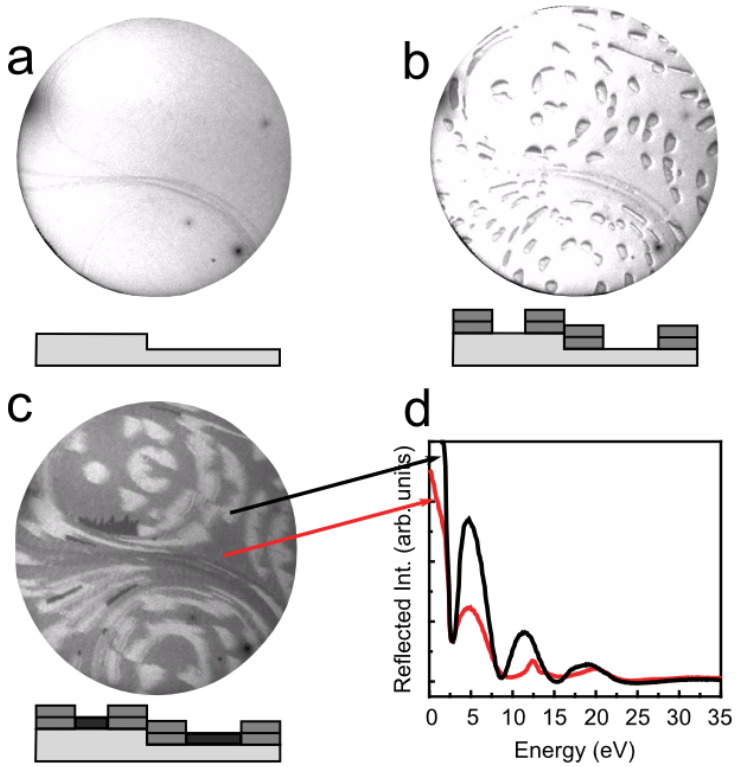

FIGURE 3.15: **a**–**c**. LEEM images of FeO grown by OMBE at 800 K in an O_2 background pressure of 10^{-7} Torr. Total amount of deposited iron is 1.1 ML_{Fe}. Field of View 10 μm and the electron energy is 18.0 eV. The time elapsed is 0, 120 and 744 seconds, respectively. The schematics below the images illustrate the cross-sectional morphology of the bare substrate (a), bilayer thick FeO (b), and monolayer plus bilayer thick FeO (c). **d**. Electron reflectivity versus electron energy from 1 ML (red) and 2 ML (black) regions of the final film.

switch to monolayer mode when the film is almost complete. The electron reflectivity (see Figure 3.15d), identifies the areas that correspond to FeO bilayer or monolayer. As shown in Figure 3.15c, the complete film is not homogeneous, consisting of monolayer (dark grey) and bilayer (medium grey) regions.

Next we consider the effect of temperature on the island density for different oxygen pressures (see Figure 3.16). The trend is similar to the previously presented study at the higher pressure (10^{-6} Torr, Figure 3.12): the island density decreases with increasing temperature. We conclude that at a given temperature the island density is the lowest at the intermediate pressure of 10^{-7} Torr.

Summarizing, FeO(111) growth operated using O–MBE exhibits two modes depending on the selected oxygen pressure. At 10^{-6} Torr, the growth proceeds always through bilayer islands. At 10^{-7} Torr, while the islands are initially bilayer, the growth switches to mononalyer islands. Finally, at 10^{-8} Torr, only monolayer growth regime is observed.

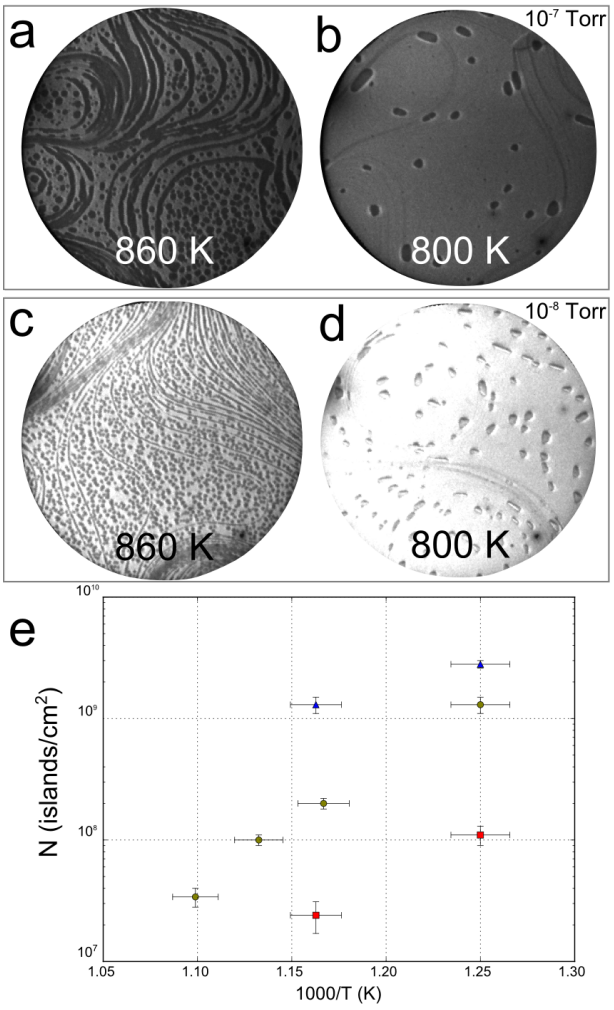

FIGURE 3.16: **a**–**b**. LEEM images acquired during the growth of FeO at 860 and 800 K respectively (p_{O_2}=10^{-7} Torr). **c**–**d**. Same but under a pressure of 10^{-8} Torr of oxygen. The field of view is 10 μm. **e**. Plot of the island densities versus inverse temperature. The symbols correspond to the data at the different pressures: green circles for 10^{-6} Torr, red squares for 10^{-7} Torr and blue triangles for 10^{-8} Torr.

The island density decreases with the temperature and the influence of oxygen pressure is non-monotonic: the fewest islands nucleate at an intermediate oxygen pressure (10^{-7} Torr).

3.5 Discussion

We introduce the FeO(111) growth on Ru(0001) showing how the oxidation of an iron ultrathin film in molecular oxygen pressure leads to the formation of well-ordered FeO nanostructures. Deposition of submonolayer amounts of iron and subsequent oxidation yields the formation of 1 ML and 2 ML regions that evolve to two monolayer height FeO regular islands under prolonged oxidation. STM and LEED measurements confirm

that FeO(111) is laterally expanded in the initial stages and the growth on Ru(0001) is not pseudomorphic. XPS analysis are in agreement with the formation of a typical Fe^{2+} compound. Moreover the STM images show that the 2 ML regions have been fed by the 1 ML regions during a prolonged oxidation. Thus, we can interpret this event by assuming that FeO appears stabilized by the formation of 2 ML thick islands at our experimental condition. Further, FeO(111) has been grown by oxygen-assisted MBE and its growth on Ru(0001) has been studied by STM, LEED, XPS and LEEM. We establish that a FeO phase grown using this different technique is structurally and chemically equivalent to the oxide produced by depositing and oxidizing Fe.

The O–MBE method presented an unexpected result: the morphology of the film changes from *bilayer* islands that coalesce to a continuous film at 10^{-6} Torr to *monolayer* islands at 10^{-8} Torr. While, at intermediate pressures (10^{-7} Torr), the film initially nucleates as a bilayer to switch to monolayer growth when it is closing. These results are surprising because the monolayer and bilayer exhibit the similar structure and composition. So a modification in the O_2 background pressure is not reflected in a stoichiometry change but a variation in the film morphology (i.e. thickness) occurs. At lower pressure, the supply of molecular oxygen barely keeps up with the incoming iron atoms, with an arrival ratio of 5:1[10], and might be assumed to be insufficient in order to maintain the FeO stoichiometry. This phenomenon might be driven by the Ru(0001) substrate, which on one hand readily catalyzes the O_2 dissociation [98] and on the other acts as a reservoir of atomic oxygen during the iron deposition. We next propose an explanation for the striking role of oxygen pressure on morphology.

In O–MBE, the FeO–free Ru substrate is covered by adsorbed oxygen and the oxidation reaction probably takes place when Fe atoms reach the surface and interact with the adsorbed atomic oxygen. The key to understand the role of the O_2 pressure on FeO thickness can be found comparing the areal density of the adsorbed oxygen with the oxygen contained in monolayer and bilayer FeO, respectively, as we next elucidate. The areal density of oxygen in a FeO monolayer is a factor of 0.72 less than the density of Ru atoms in the surface layer. If the adsorbed oxygen concentration is lower than 0.72 ML_{Fe}, forming a monolayer island of FeO reduces the oxygen density on the ruthenium. On the contrary, if the oxygen density is higher than 0.72 ML_{Fe}, then forming a monolayer *increases* the oxygen density. But this increase in density is hindered taking in account two considerations. First, the oxygen density on ruthenium is limited: one oxygen atom per ruthenium atom [99]. Second, even for lower densities O–O interactions on Ru are repulsive, as shown by the decrease of the oxygen binding energy as a function of coverage [99, 100]. Consequentially, we propose that if the oxygen density is sufficiently high, the growth of monolayer FeO is hindered because this increases the density of

[10] This value can be compared to the 500:1 at the highest pressure employed.

adsorbed oxygen. Instead, FeO bilayers, with an oxygen density of 1.44 ML_{Fe} (due to the two oxygen planes of the bilayer), grow and produce a decrease in the adsorbed oxygen.

The proposed mechanism is supported by some evidences. Data from two methods show that the concentration of adsorbed oxygen is near the calculated value (0.72 ML) to select either monolayer or bilayer growth mode. First, after cooling to room temperature, STM images reveal (see Figure 3.14a and b) that FeO islands grown by O–MBE are surrounded by regions of chemisorbed oxygen producing a (2×2) structure on Ru. An oxygen concentration above about 0.75 ML exhibits a (2×2) arrangement labeled as $(2 \times 2) - 3O$ [101]. Second, a rough estimate from the reflectivity changes during FeO growth gives a similar oxygen density [79]. We do note, however, that oxygen densities around 0.75 ML appear to be slightly high for our continuous or sequential exposure to 10^{-7} Torr oxygen, for which we estimate doses in the range of 10 L [98–100].

In 10^{-7} Torr, the FeO growth switches between the two proposed mechanisms (bilayer and monolayer growth mode). This phenomenon can be rationalized by decreased oxygen concentration on the ruthenium caused by the smaller sticking coefficient of oxygen atoms on FeO compared with that of the ruthenium surface. This difference in sticking coefficient suggests that maintaining the oxygen concentration required to complete a uniform bilayer may be difficult at lower oxygen pressures.

The study of the island density as a function of the temperature and pressure reveals also a striking result. While at a given pressure the density decrease with temperature, O_2 pressure play a role, as easily detected in Figure 3.16. On one hand, the island densities are lower at the intermediate pressure, 10^{-7} Torr. On the other, the slope in the logarithmic plot shown in Figure 3.16e is more similar for 10^{-7} and 10^{-6} Torr than for 10^{-8} Torr. This latter effect might be associated to the bilayer versus monolayer growth regimes. Further studies are required to understand this complex behavior.

Meanwhile, we can interpret the results at a given oxygen pressure in terms of the simple nucleation and growth models that have explained the density decrease of metal and semiconductor islands with increasing temperature [102–104]. It is reasonable consider that the incoming Fe atoms reach the Ru surface and react forming a sort of oxygen-iron species that diffuse on the surface before interacting with an already nucleated island or another analogous object. In the former case, the island grows while a new island nucleates in the latter case. This consideration drives to two growth regimes [102]: the initial nucleation mode, where the number of islands keeps increasing, followed by the growth regime in which the already nucleated islands keep spreading. Under this simple model, increasing the temperature causes faster surface diffusion of the oxygen-iron complex, allowing them to explore larger areas, which results in fewer nucleated islands.

We remark that even in homoepitaxial growth this model can be too simple and it is much more simple for heteroepitaxial or bi-component oxide growth. Nevertheless, we would estimate the main energy barrier involved by assuming the simplest nucleation model [103] for the highest pressure condition. Then the island area is disregarded (as well as the bilayer thickness) and the critical nuclei is considered to be a dimer. The following formula describes the relationship between the island density (N) and the diffusion coefficient (D_S):

$$N^3 \sim \frac{R\theta}{D_S} \tag{3.1}$$

where R is the rate of arrival of iron atoms and θ is the coverage. Using the experimental island densities, D_S has been solved and the plot of Figure 3.17 has been generated. Assuming that the diffusion of the iron (or iron-oxygen complex) on the surface follows as Arrhenius from

$$D_S = D_{S_0} \exp \frac{-E_S}{kT} \tag{3.2}$$

where D_{S_0} is a pre-factor and E_S is the diffusion barrier (eV), T the temperature and k the Boltzmann constant, the dependency of D_S should follow the line shown in Figure 3.17. It corresponds to a diffusion barrier of (5.9 ± 0.5) eV which is much larger than the typical diffusion barriers for surface diffusion on metals, while it is in the expected range for surface diffusion on oxides [105]. Nevertheless, it is reasonable to conclude that the model is too simplistic and it cannot describe the FeO growth process in detail. This fact is reflected by obtaining an unrealistic diffusion prefactor (10^{37} cm^2 sec^{-1}). As directly observed in Figure 3.16e, the estimated energy barrier is much smaller (i.e. smaller slope) for the lowest pressure of 10^{-8} (2.2 eV), while the intermediate pressure value is closer to the high pressure case (4.5 eV).

3.6 Summary

In this chapter we start introducing the characteristics of the FeO(111) ultrathin films on Ru(0001) prepared by the oxidation of a metallic precursor. Briefly, a investigation of the chemical and structural properties of this iron oxide has been presented. Following, we have studied the initial stages of the FeO growth on Ru(0001) performed by oxygen-assisted MBE. We have observed that in an excess of oxygen ($\sim 10^{-6}$ Torr), FeO nucleates in bilayer islands, which eventually coalesces covering the entire surface. A strong influence of the oxygen pressure has been observed, thus at 100 times lower oxygen pressure, FeO grows in monolayer form. At intermediate pressures ($\sim 10^{-7}$ Torr), the initial islands grow as a bilayer but eventually switch concluding the nucleation as a monolayer. We interpret the role of the oxygen pressure by considering how the concentration of oxygen adsorbed on the Ru changes concurrently its incorporation into

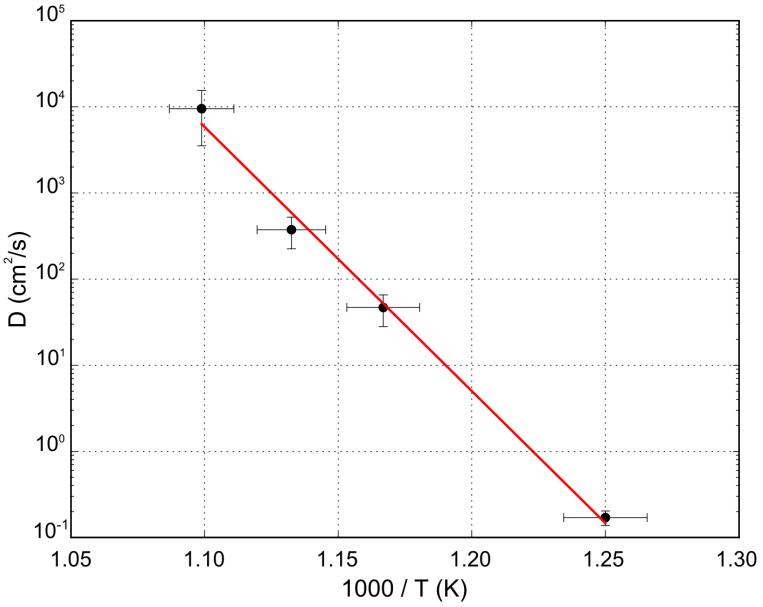

FIGURE 3.17: Plot of the surface diffusion versus inverse temperature, as extracted from a simple nucleation model (see text) and the nucleation data corresponding to an oxygen pressure of 10^{-6} Torr.

the forming film. Monolayer FeO formation can either decrease or increase the density of the adsorbed oxygen. The latter case, which occurs at high concentrations of adsorbed oxygen, increases above a critical density. Consequently, the monolayer growth is suppressed leading to exclusive bilayer growth. The island density is influenced by the temperature, thus an increase of substrate temperature produces a decrease of the number of islands. But the evolution of this aspect as a function of the oxygen pressure is not monotonic, underlying the complexity of the FeO system.

Chapter 4

$Fe_3O_4(111)$ on Ru(0001)

4.1 Introduction

Magnetite (Fe_3O_4) is the oldest known magnetic material. Historically refereed to as lodestone[1], this iron oxide and its magnetic properties have been known since the ancient Greeks [106]. In fact, its name and that of the phenomenon of magnetism, may be derived from *Magnesia*, a region in Thessaly (Greece) where the lodestone could be discovered.

The structure of magnetite (see Figure 4.1) is an inverse spinel and was established by Bragg and Nishikawa in 1915 during the first application of the x-ray diffraction technique [12]. Magnetite has a face-centered cubic unit cell based on 32 O^{2-} ions which form hexagonal layers along the [111] direction. The iron cations contained in

[1]Lodestone refers to the magnetic "version" of magnetite found naturally.

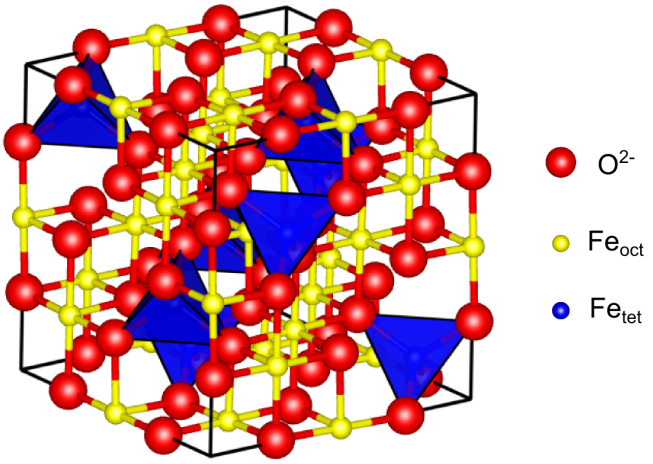

FIGURE 4.1: Ball-and-stick model of the magnetite structure. The atoms are labeled as reported in the right side and the unit cell is outlined. Only the tetrahedral sites have been shaded.

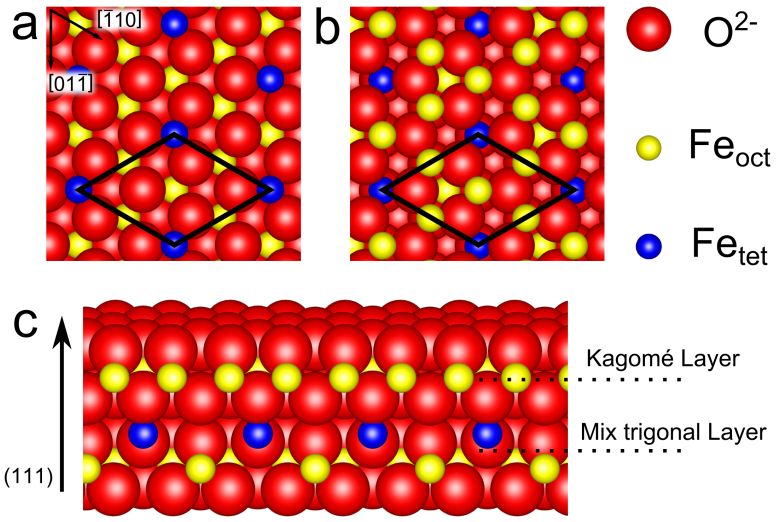

FIGURE 4.2: Magnetite layer structures along the (111) direction. Two types of Fe–O layer are shown: Mix-trigonal layer (**a**) and Kagomé layer (**b**). The two surface unit cells and the crystallographic directions have been outlined. **c**. Side view of Fe_3O_4. The (111) layer sequence with tetrahedrally coordinated irons (blue spheres), with octahedrally coordinated irons (yellow spheres) and with oxygen atom (red spheres) is indicated.

the Fe_3O_4 are nominally divalent and trivalent and are located in interstitial sites. A fraction of the Fe^{3+} cations (blue spheres in Figure 4.1) are placed in tetrahedral sites, also called A sites, while the octahedrally coordinated positions (B sites) are populated by a mixture of Fe^{3+} and Fe^{2+} ions (yellow spheres in Figure 4.1). In stoichiometric magnetite divalent and trivalent iron cations occupy equally the octahedral interstices, i.e. $Fe^{2+}_{oct}/Fe^{3+}_{oct}= 0.5$. The formula can be written as:

$$\left(Fe^{3+}\right)_{tet}\left(Fe^{2+},Fe^{3+}\right)_{oct}\left(O^{2-}\right)_4$$

where the cations subscripts define their position. Along the [111] direction of the crystal structure, the hexagonal oxygen planes form a cubic ABC stacking sequence. Between the O(111) planes two types of Fe layers are present. The first type is the Kagomé layer in which $\frac{3}{4}$ of the octahedrally coordinated sites are occupied by divalent and trivalent cations (see Figure 4.2b). The second type is formed by three hexagonal (mix–trigonal layer) Fe layers. Within the mix–trigonal layer only $\frac{1}{4}$ of all sites are occupied, as displayed in Figure 4.2a. Figure 4.2c summarizes the Fe_3O_4 stacking sequence along the [111] direction and show the alternation of Kagomé and mix–trigonal layer.

Fe_3O_4 is ferrimagnetic at room temperature and has a Curie temperature $T_c \simeq 858$ K [107]. The room temperature easy axes of magnetization are the <111> lattice directions [12]. The first order anisotropy constant changes using upon cooling to 130 K, temperature below which the easy axis flips to the <100> direction [108]. The ferrimagnetic order has been explained by the antiferromagnetic coupling between the A and B

sublattices. Cations are coupled ferromagnetically within the octahedral (B) and the tetrahedral (A) sites (blue dashed line in Figure 4.3) while the two Fe^{3+} occupying adjacent A and B sites are antiferromagnetically coupled (black dashed line in Figure 4.3). Thus, the incomplete cancellation of the two B site magnetic moments by the antiparallel A site cation moment results in ferrimagnetism.

In spite of intensive efforts dedicated to study magnetite, surprisingly, an agreement has not been reached concerning its magnetic moment, and orbital and spin components. It usually considered that octahedral and tetrahedral site orbital moments are antiparallel. Thus, the expected net orbital moment vanishes as result of the balance of the partial (A and B sites) orbital moments [109]. Moreover, the net magnetic moment arises from the unpaired octahedral Fe^{2+} cations, which present a spin moment of $\sim 4\mu_B$ arising from four uncompensated parallel spins. Most theoretical works are consistent these arguments, presenting a spin moment of 4 μ_B and a very small (i.e., quenched, ~ 0 μ_B) orbital moment in bulk magnetite [110–113]. However, widely differing experimental measurements of these values have been reported, mostly based on x-ray magnetic circular dichroism (XMCD). A large unquenched orbital moment of 0.67 μ_B together with a spin moment of 3.68 μ_B have been reported by Huang *et al.* [112]. Goering *et al.* suggested that these results were erroneous [114] and proposed a vanishing small orbital moment with a spin moment of 3.8 μ_B [115]. Later, Goering *et al.* demonstrated the importance of the surface sample preparation in the XMCD measurement finding a reduced spin moment by up to 50% from the bulk value. Their argument of changes in the electronic and magnetic properties of magnetite induced by surface preparation methods [116] disagrees with the enhanced value of 7.7 μ_B reported by Arora and co workers [117]. Thus, the results published so far remain controversial, with vanishing and non-vanishing orbital moments (see Table 4.1). Goering has recently tried to clarify this invoking several arguments: the data treatment, the sample stoichiometry and the presence of impurities [109]. In particular, he suggests that even small variation in the magnetite stoichiometry could preclude the balancing between the orbital moments at A and B sites, resulting in a non vanishing total orbital moment.

At room temperature, Fe_3O_4 is a bad conductor but exhibits a high conductivity ($10^3 < \sigma < 10^4$ $\Omega^{-1}m^{-1}$), at least compared to the rather low values of normal spinels ($\sim 10^{-5}$ $\Omega^{-1}m^{-1}$) [122]. The conduction mechanism is attributed to electron exchange (*hopping*) between Fe^{2+} and Fe^{3+} ions in octahedral positions, according to the relation:

$$Fe^{2+}_{oct} - e^- \Leftrightarrow Fe^{3+}_{oct}$$

Thus only the $3d$ electrons of the Fe ions located in the B site would contribute to the transport phenomena [123]. Below room-temperature the reduction of the electron

Sample	Orbital m_{orb} (μ_B)	Spin m_{spin} (μ_B)	$\frac{m_{orb}}{m_{spin}}$	Ref.
8 nm Fe_3O_4/MgO/GaAs(100)	0.47	2.84	0.17	[118]
2.5 nm Fe_3O_4/$BaTiO_3$(001)	0.44	1.20	0.37	[119]
bulk Fe_3O_4	0.65	3.68	0.18	[112]
bulk Fe_3O_4	0.51	3.54	0.14	[120]
bulk Fe_3O_4	-0.001	3.90	-0.00026	[115]
bulk Fe_3O_4	<0.03	1.7	<0.0018	[116]
bulk Fe_3O_4	0.06	4.08	0.03	[121]
Theory	0.06	4	0.015	[112]
Theory	0.43	4	0.108	[112]
Theory	0.02	3.7	0.005	[113]
Theory	0.05	3.9998	0.013	[111]

TABLE 4.1: Spin (m_{spin}) and orbital (m_{orb}) moment of the magnetite from the literatures.

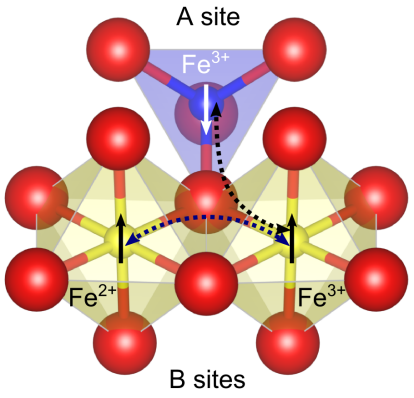

FIGURE 4.3: Crystallographic and magnetic configuration of magnetite. Two octahedral (B sites, yellow) Fe^{2+} and Fe^{3+} cations together with a tetrahedrally coordinated (A site, blue) Fe^{3+} cation are shown. The oxygen atoms are represented as red spheres. Blue dashed line outlines the ferromagnetic interaction between two octahedrically coordinated iron cations. Black dashed line depicts the antiferromagnetic coupling between two different sites (A and B).

mobility produces a drastic decrease of the conductivity. This *metal-insulator transition* (MIT) that occurs at $T_v \simeq 120$ K[2] was discovered by Verwey in 1929 [125]. Together with the sharp drop in electrical conductivity, Verwey found that magnetite undergoes a structural distortion. In fact, stoichiometric magnetite undergoes a first-order phase transition when it is cooled below T_v [126]. Different diffraction studies have shown that the low temperature phase has a monoclinic Cc symmetry [127, 128].

[2]The Verwey transition temperature is strongly influenced by its stoichiometry. Verwey and Haayma systematically investigated how the stoichiometry affects the variation of the transition temperature and observed that introducing octaedral (i.e. iron) vacancies, a lowering of the critical temperature from 120 to 100 K [122, 124] is observed.

The MIT phenomenon was interpreted by Verwey and co-workers as an order-to-disorder transition of the octrahedrally coordinated iron cations involved in the electronic conduction [129]. It can be explained as an electronic localization on the B-site cations in which a long-range charge ordering of divalent and trivalent irons occurs. Although intensive experimental and theoretical efforts have been dedicated to determine the origin of the Verwey transition, it remains a long-standing problem in solid-state physics with conflicting information as to whether the electronic transition is driven by the structure distortion, or viceversa [108, 122, 130–132].

Magnetite is predicted not only to have negative spin polarization[3] but also to exhibit a half-metallic behavior with complete spin polarization at the Fermi level (E_F) [113, 134–136]. Fe_3O_4 is characterized by an unusual band structure (see Figure 4.4) in which there is a gap in the majority spin band at the Fermi level but not in the minority spin band. One minority spin electron per formula unit occupies energy levels just below the E_F and takes part of the previously mentioned thermal hoping [6, 137]. Because there is only one spin band at E_F, magnetite is -100% spin-polarized. Although the spin-down character of the electrons at the E_F was theoretically as well as experimentally confirmed by early experiments, further spin-polarized photoemission measurements produce highly disparate results in which polarizations range from -40% to -80% for Fe_3O_4 single crystals [136, 138]. Several factors have been invoked in order to explain these contradictory results, including variation in the oxide stoichiometry or strong electron correlation effects. Nevertheless, the half-metallic behavior of magnetite is still a reason of discussion in the scientific community.

Magnetite was also one of the first materials in which the magnetoelectric effect was studied. Early results suggest that, at very low temperature (∼4.2 K), a static electrical polarization can be induced by applying an external magnetic field [139, 140]. Thus, magnetite has been included in the group of multiferroic materials, i.e. materials in which ferroelectricity and magnetism coexist and can be controlled [141].

Magnetite thin films

The attractive properties of magnetite and the trend of nanotechnology to reduce the thickness and/or lateral size of devices to the nanoscale, motivate the growth of Fe_3O_4 ultrathin films [142, 143]. This interesting iron oxide has been grown by many groups in the last decades using different deposition techniques [molecular-beam epitaxy, pulsed laser deposition (PLD), sputtering]. Although the selection of an adequate deposition

[3] The spin polarization is positive (negative) if the majority (minority) spin at the Fermi level is parallel to the bulk magnetization ([111] direction in magnetite). Negative spin polarization, however, has rarely been observed [133].

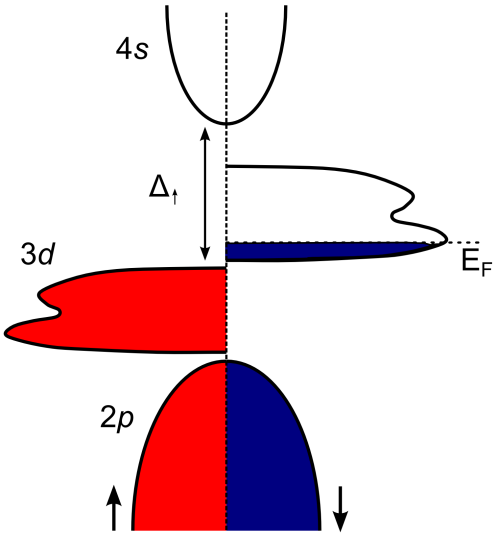

FIGURE 4.4: Schematic density of states for magnetite [6]. A band gap is present in the majority (↑) spin band. The conduction is operated by minority (↓) electrons, which occupy narrow localized states to the E_F.

technique is important, the substrate choice can also be crucial for the preparation of magnetite thin films with desired characteristics. A quick review of the literature reveals that MgO has been selected by the scientific community as one of the best substrates because its structural match with Fe_3O_4 [117, 133, 144–165]. Nevertheless, magnetite growth has been effectively carried out on a variety of different substrates, including metals (Pt [166–175], W [176], Ag [177]), oxides (ZnO [178], STO [141, 179–181], Al_2O_3 [182–184], YSZ [185, 186]) or semiconductors (GaAs [187–191], InAs [192], GaN [193]).

There is a consistent trend in the literature showing that the properties of magnetite thin films differ markedly from those expected for the bulk counterpart. Several studies on Fe_3O_4 thin films report an unsaturated magnetization at high fields [155]. This anomalous behavior seems to be an intrinsic property of magnetite films which is apparently independent of the particular deposition technique [162, 194, 195]. However, values of the extrapolated anisotropy constant are not high enough as to justify the lack of saturation. These effects are accompanied by a superparamagnetic behavior when the thickness of the film is reduced to the nanometric scale [153, 156, 184].

Recently, we reported that Fe_3O_4/STO:Nb(001) films grown by PLD exhibit a robust well-defined easy axis along the in-plane <100> direction [181]. This observation disagrees with the <110> direction[4] usually reported in the literature for thin films [161, 196, 197]. These anomalies in thin film magnetic properties appear together

[4]The <110> direction is expected for the surface of a magnetite single crystal because it corresponds to projection of the <111> bulk easy axis onto the <001> surface.

with an increase in the electrical resistivity and a variation or even disappearance of the Verwey transition [148, 198].

Several groups convincingly attributed these thin film behavior to the films microstructure and the formation of *antiphase boundaries* (APBs) during the Fe_3O_4 film growth. APBs, observed by different microscopy techniques [150, 157, 162, 199], are natural growth defects resulting from the mismatch of the film/substrate structure. According to a layer-by-layer growth mechanism, magnetite islands nucleate on the substrate surface and eventually coalesce into a closed layer. When the layer is complete, the resulting oxygen sublattice is continuous but an improper stacking sequence of the cation lattice occurs in most cases. Thus, APBs can be interpreted as an interruption of the Fe_3O_4 cation chains in a continuous oxygen lattice creating new magnetic exchange interactions. Because many possible types of APBs are present, each characterized by a specific atomic arrangement, different exchange phenomena are originated across these defects. Although the magnetic coupling across them can be antiferromagnetic (AF) [149, 157, 162], ferromagnetic coupling has also been observed [200]. These APBs may pin down magnetic domain walls, making the film saturation difficult to achieve by applying an external magnetic field. Moreover, the role of the AF-coupled APBs on the electron transport has also been studied. The observed increase in resistivity with decreasing thickness is explained by the formation of these inhomogeneities. APBs act as scattering centers, which interfere with the electron propagation producing a decrease of the conductivity [148].

The observation of magnetoresistance in Fe_3O_4 thin films [147, 153, 159, 201], absent in bulk crystals, is also caused by the presence of AF-coupled APBs. Upon application of a magnetic field, the orientation of the spins at these boundaries can be changed favoring the conduction across the APBs [149]. A detailed review about these effects arising on magnetite thin films has recently been prepared by Moussy [202].

In this chapter we examine the properties of nanometer-sized Fe_3O_4 crystals grown on Ru(0001). Conflicting reports are available in the literature about the magnetic properties of ultrathin magnetite. While some studies report that magnetite films close to 3 nm thickness exhibit a well defined magnetic structure [117, 171, 190, 193], others indicate that clear signs of superparamagnetic behavior are observed at the same thickness [144, 153, 156, 184, 203, 204].

We begin by characterizing several $Fe_3O_4(111)$ films grown by a conventional MBE method. STM, LEED and XPS reveal that magnetite can be obtained by prolonged oxidation of the metastable FeO phase, according to previous works on Ru(0001) [40, 75]. Latter we present the growth of nanometer-sized magnetite islands by O–MBE monitored in real-time by LEEM. By means of spectroscopic and diffraction techniques,

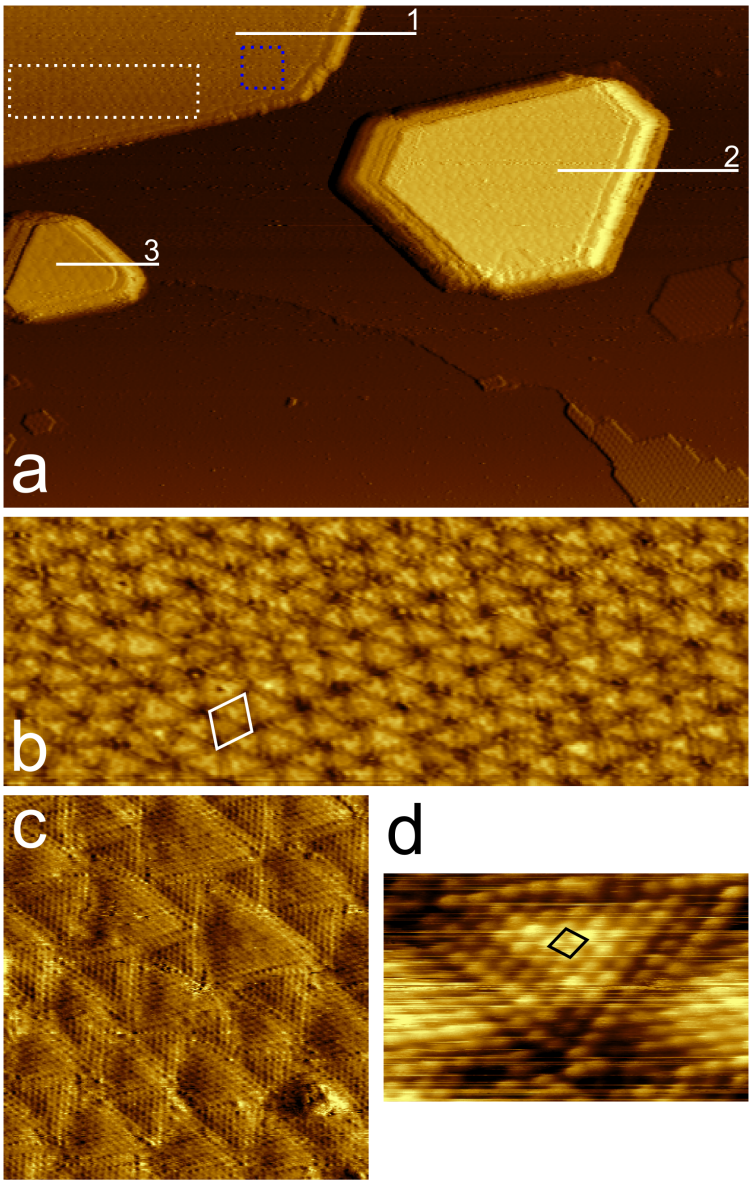

FIGURE 4.5: **a**. 250×68 nm^2 STM image showing three different Fe_3O_4 islands on Ru(0001) surface(I_t=1.0 nA and U_b=+1.90 V). The steps marked with 1, 2 and 3 are 2.1 nm, 3.0 nm and 4.4 nm in height, respectively. **b**. 58×21 nm^2 STM image showing the upper island surface (white box region in figure a) collected at I_t=1.2 nA and U_b=+1.90 V. The superstructure periodicity is 32.2 Å (marked in white). **c**. 17×17 nm^2 (I_t=1.6 nA and U_b=+1.70 V) high-resolution image of a different region marked by a blue box in Figure (a). **d**. Atomic resolution STM image of a triangular feature in Figure (b). The unit cell marked in black has a lattice constant of 3.6 Å (4×2.5 nm^2 I_t=2.1 nA and U_b=+1.65 V).

the $Fe_3O_4(111)$ crystals have been characterized and stable magnetic domains have been imaged. Then, by analyzing the attenuation of the XPS signal of the substrate, their thickness has been estimated. Moreover, orbital and spin moment of magnetite have been measured and discussed. Finally, a brief study of the role of the iron flux of O–MBE for the growth of magnetite has been presented.

4.2 Growth of $Fe_3O_4(111)$ on Ru(0001) by MBE

In this section we present the characterization of nanometer-thick magnetite islands, prepared using the MBE method. When 1.2 ML of iron is deposited on Ru(0001) and subsequently oxidized at a high temperature of 920 K in p_{O_2}=2×10^{-6} Torr, FeO is not longer stable [75, 205]. These films have been characterized by STM, LEED and XPS.

In Figure 4.5a, a large-scale STM image of the surface showing the Ru(0001) covered with three regular islands is shown. Compared with the previous experiments (see Chapter 3), the surface remains mostly uncovered and the islands are characterized by a greater thickness, ranging between 2.1 nm and 4.4 nm. The island overlayer changes drastically and the typical FeO moiré superstructure is absent. As shown in figure 4.5b, the island exhibits a different superstructure characterized by six triangular features hexagonally arranged. The observed corrugation presents a periodicity of 32.2 Å. This new superstructure is not very well ordered as shown in Figure 4.5c in which the presence of different triangular-shaped features is observed. A high-resolution STM image recorded on this region shows protrusions forming a 3.6 Å hexagonal lattice.

Since these different surface arrangements cannot be directly associated with a single FeO(111) termination, other regions of the sample have been studied. Figure 4.6a shows a large-area STM image that depicts a different nanometer-thick island. A hexagonal island has nucleated on top of a triangular-shaped island and the two regions are characterized by different superstructures. Figure 4.6b shows a detail of the hexagonal region that presents a similar irregular arrangement of triangular protrusions shown in Figure 4.5. Figure 4.6b is characterized by a defective region where protrusions with a 5.2 Å periodicity can be seen. This value can be associated with a strong contraction of the Fe_3O_4 surface unit cell if compared with the bulk value (6 Å [75]).

We can speculate about the origin of the irregular superstructure observed in the STM images from Figures 4.5 and 4.6. In fact, different studies report the phenomenon of *biphase ordering* on $Fe_3O_4(111)$ for different experimental conditions. A large superstructure similar to ours (Figure 4.5b and 4.6b) has been interpreted as the nucleation of ordered regions of $Fe_{1-x}O(111)$ in the topmost layer of Fe_3O_4 [168, 206–208]. Thus,

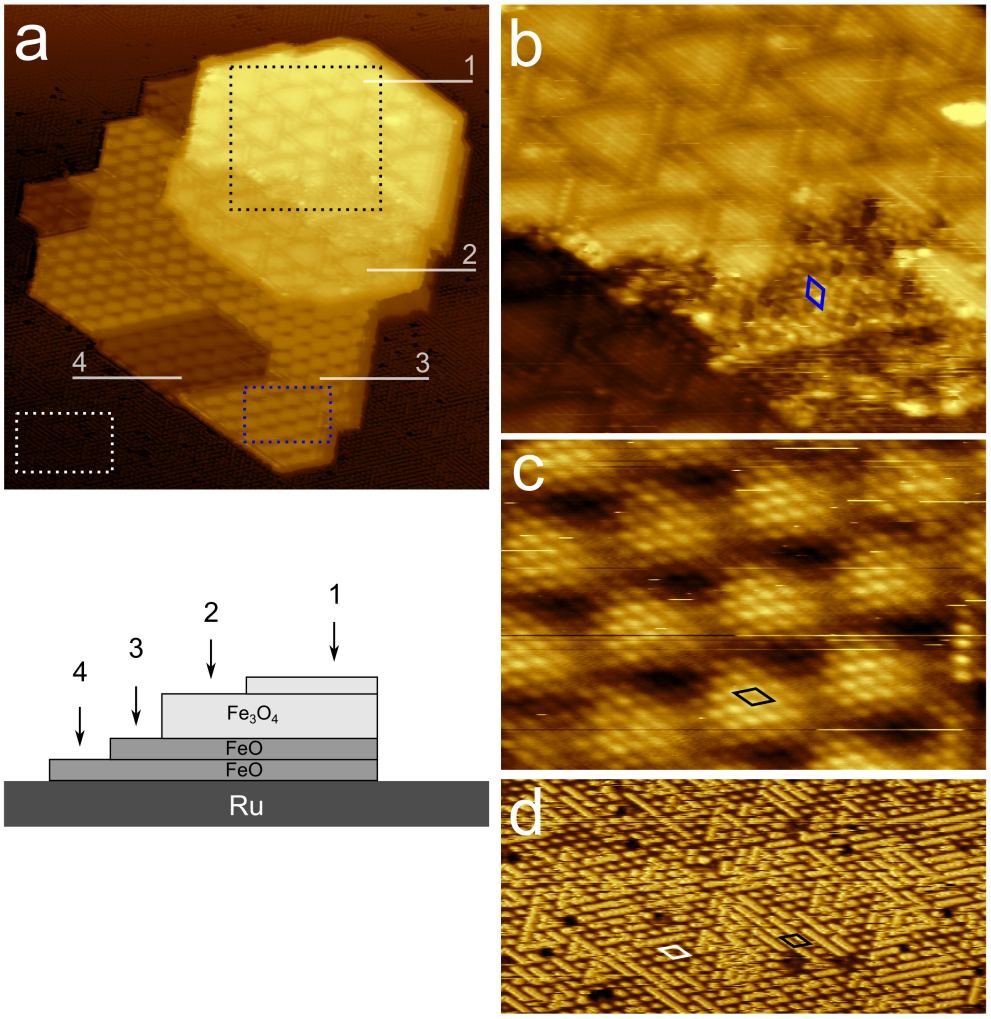

FIGURE 4.6: **a**. 50×50 nm^2 STM image of a bi-phase iron oxide island on Ru(0001) surface (I_t=2.33 nA and U_b=+1.7 V). The thickness of the terraces marked with 1, 2, 3 and 4 is 1.15 nm, 0.90 nm, 0.50 nm and 2.55 nm, respectively. **b**. High-resolution STM image of the upper terrace marked by a black box in figure a (18.2×16.3 nm^2 I_t=2.3 nA and U_b=+1.7 V). The surface exhibits a superstructure created by triangular irregular features. **c**. Atomic resolution STM image marked by a blue box in Figure (a). The typical FeO(111) moiré superstructure has a cell length of 21.5 Å. The lattice constant is 3.6 Å and is marked in black (10.9×9.5 nm^2, I_t=1.3 nA and U_b=+1.7 V). **d**. Atomic resolution STM image of the Ru(0001) region marked by a white box in figure (a). The Ru(0001) appears covered by atomic oxygen producing a (2×2) and (2×1) structures (unit cells are marked in white and black, respectively). The lattice constant is 5.4 Å (20.9×10 nm^2, I_t=2.3 nA and U_b=+1.7 V). The schematic helps the comprehension of the STM images.

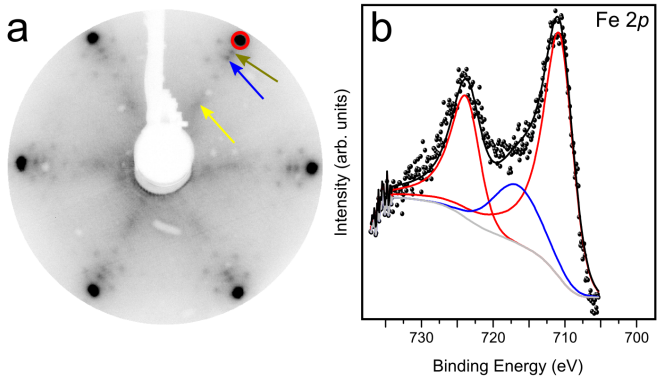

FIGURE 4.7: **a**. LEED patterm collected from the surface containing FeO and Fe_3O_4 species. Three series of hexagonally arranged sets are present. The stronger (1×1) structure is marked with red circle and corresponds to the substrate. The two weak hexagonal (1×1) patterns are relative to the FeO(111) (blue arrow) and to the Fe_3O_4(111) (green arrow). The FeO pattern exhibits the typical moiré structure surrounding the first-order spots. A blurry (2×2) hexagonal structure is marked by a yellow arrow. **b**. Fe 2*p* core-level XPS spectrum acquired from FeO + Fe_3O_4. The experimental spectrum (black dots) has been fitted using a black solid line originated from the sum of the contribution of the main photoemission peaks (red) and the shake-up satellites (blue).

we interpret the islands with triangular features as a *biphase* termination of Fe_3O_4, probably due to an insufficient supply of oxygen to reach an unreconstructed surface termination. Additionally, the presence of an atomic arrangement of 3.6 Å, close to that of the FeO(111) surface unit cell (3.2 Å) can be used to explain the magnetite reconstruction and the nucleation of $Fe_{1-x}O$(111) regions.

Figure 4.6c shows a detail of the thinner film on which the Fe_3O_4 is nucleated. The underlying layer exhibits the characteristic FeO moiré with a periodicity of 21.5 Å and using the atomically resolved image the surface unit cell has been measured (3.3 Å).

In consequence by observing the surface by STM we suggest the coexistence of two different iron oxide species nucleating on Ru(0001). These results have been confirmed by spectroscopy and diffraction measurements. The Fe 2*p* XPS spectrum acquired from the observed surface (Figure 4.7b) is slightly different when compared to the previous FeO spectrum 3.7. The binding energies of the main photoemission peaks are higher (710.8 eV for Fe $2p_{3/2}$ and 723.9 eV for Fe $2p_{1/2}$) than those recorded from FeO what suggests that, although iron is predominantly in the form of Fe^{2+}, the film contains also some Fe^{3+}. The characteristic Fe^{2+} shake-up satellite at ∼715 eV has a lower intensity that in the spectrum of FeO(111) suggesting too the presence of Fe^{3+} contributions. The increase of the spin-orbit splitting energy (13.1 eV) confirms this idea [7, 92, 94]. The occurrence of two different iron oxide phases, FeO(111) and Fe_3O_4(111), is also indicated by the LEED pattern shown in Figure 4.7a. The most intense (1×1) hexagonal structure marked by a red circle corresponds to the Ru(0001) substrate. The first-order diffraction

spots indicated by a blue arrow describe a surface unit cell of 3.15 Å that combined with the satellite spots (20.0 Å) proves the presence of FeO(111). Between the Ru(0001) and FeO(111) spots, a new set of (1×1) spots can be observed (marked by a green arrow). The surface unit cell is slightly smaller (2.95 Å) if compared to that of FeO(111) and can be regarded as a Fe_3O_4(111) O–O interatomic distance within magnetite layers [40, 75, 78]. Furthermore, blurry spots with a (2×2) periodicity can be observed (yellow arrow in figure 4.7a) and explained by taking in account two contributions. The first corresponds to the iron sublayers in magnetite (111) that form a (2×2) overlayer with respect to the close packed oxygen layers in the Fe_3O_4 structure (see Figure 4.2a and b). The second contribution can be interpreted as that corresponding to chemisorbed oxygen on Ru(0001). This explanation is corroborated by the STM results (Figure 4.6c) where O(2×2)/Ru(0001) and O(2×1)/Ru(0001) phases are clearly identified by the atomic resolved image in Figure 4.6d [209, 210].

Discussion

By means of microscopy, spectroscopy and diffraction techniques, we demonstrate the possibility of obtaining a very thin Fe_3O_4(111) crystals on Ru(0001). STM images reveal that some islands, probably nucleated on top of an FeO(111) buffer layer, exhibit a height lower than 1 nm. According with the (111) stacking sequence of magnetite, they are formed by ∼3 oxygen planes and could be considered to be at the unit cell limit. This result is unexpected: previously Ketteler and co workers using thermodynamic arguments [75, 76], suggested that the stabilization of magnetite phases occurs only when more than one unit cell is reached. They conclude that the minimum FeO film thickness for such a stoichiometry conversion to magnetite is 4 ML_{FeO}. Our study clearly establishes that a magnetite-like phase (i.e., 2×2 LEED periodicity, bi-phase termination, Fe^{2+}+Fe^{3+} XPS spectra) can be stabilized when the number of FeO layers is lower than 4 ML_{FeO}.

4.3 Growth of Fe_3O_4(111) on Ru(0001) by O–MBE

In this section, the growth of Fe_3O_4(111) by O–MBE has been studied and discussed. We have grown the iron oxide films in 3.8×10^{-7} Torr of molecular oxygen maintaining the substrate at 900 K. As reported previously (Chapter 3), initially FeO islands start to nucleate and grow on Ru(0001). When the entire surface has been covered by the FeO wetting layer, a 3-dimentional growth of islands has been observed on top of the wetting layer. This nucleation mode makes difficult to obtain ultra-thin crystals without actually monitoring the film growth, as we do here.

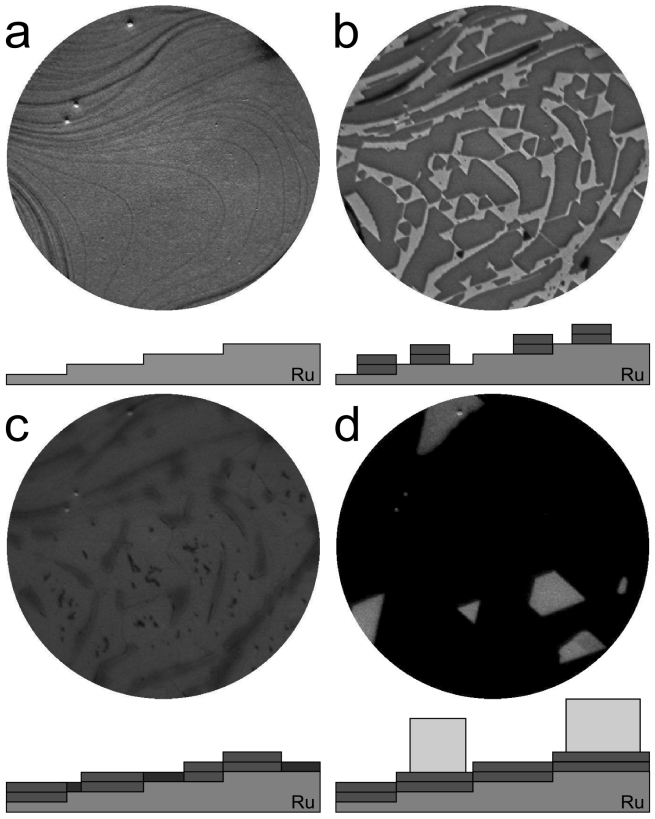

FIGURE 4.8: **a**–**d** Selected LEEM images from a sequence acquired during the growth of the magnetite crystals. The first three frames show the completion of the FeO bilayer, while the last frame shows the final film with magnetite crystals with well-defined edges. The field of view is 10 μm and the electron beam energy is 19 eV. The schematics below each LEEM images explain the surface morphology of the clean Ru (a), FeO bilayer regions (b), FeO bilayer/monolayer regions (c) and final surface (d).

In Figure 4.8 several frames are presented from a LEEM movie obtained by monitoring the film growth. Because the experiment has been carried out in the 10^{-7} Torr range (see the discussion in the Section 3.5), the FeO initially grows in bilayer mode (Figure 4.8b) and switches to mono-layer regime when the substrate is almost covered (Figure 4.8c and see also the Chapter 3). When the FeO completely wets the substrate, further iron is deposited and a change in the electron reflectivity has been registered. This variation is followed by the nucleation of large (up to several micrometer) triangular islands on top of the film (Figure 4.8d). At first glance, LEEM images reveal that the two structures (wetting layer and triangular islands) have a different character because the contrast (i.e. reflected electrons) is distinct at selected energies (19 eV). This fact has been demonstrated by diffraction and spectroscopy analysis that are shown in Figures 4.9 and 4.10.

LEED allows a rapid characterization of several iron oxide phases [13]. Figure 4.9 shows two diffraction patterns which exhibit a very similar unit cell size, 0.297–0.320 nm. The wetting layer shown in Figure 4.9a has a (1×1) hexagonal pattern combined with

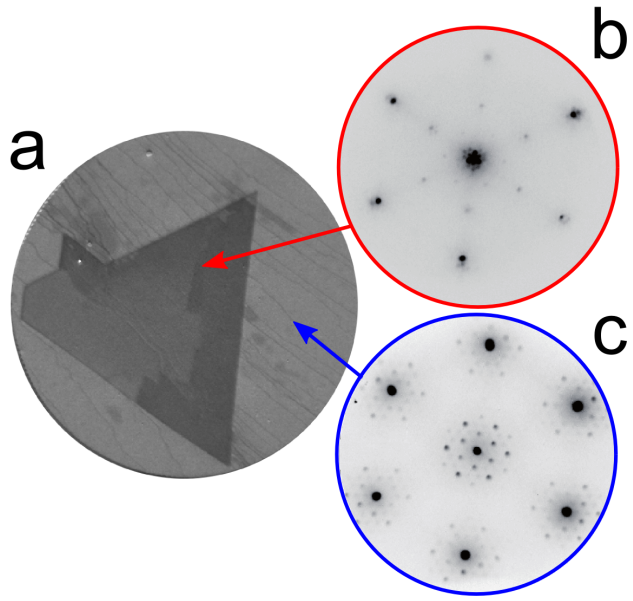

FIGURE 4.9: **a**. LEEM image of a magnetite crystal (the field of view is 4 μm and the electron energy is 8 eV). In the right side, two diffraction pattern are shown: the upper LEED pattern circled in red (**b**) has been collected from the bright island while the lower one circled in blue (**c**) corresponds to the surrounding wetting layer. In both cases the electron energy is 28 eV.

extra satellite spots, suggesting a FeO(111) surface (Figure 4.9c). In contrast, the large triangular crystal has a (2×2) LEED pattern, suggesting the Fe_3O_4(111) oxide surface. The island's oxygen lattice spacing obtained from LEED is the same as the wetting layer, 0.32±0.04 nm.

To unambiguously identify the nature of the triangular crystal, Fe 2*p* core level XPS spectra were recorded from the surface using a photon energy of $h\nu$=825 eV and collecting the photoelectrons having an E_k = 90–120 eV (Figure 4.10). For comparison, the inset presents the same Fe 2*p* spectra collected from several iron oxide compounds obtained using a conventional laboratory XPS instrument[5]. The spectrum from the wetting layer (Figure 4.10, top) presents the same features as the reference FeO film, confirming that the surface is complete covered by FeO. In contrast, the main photoemission peaks in the Fe 2*p* spectrum from the triangular crystal (Figure 4.10, bottom) appear at higher binding energies than those in the wetting-layer spectrum, suggesting that the average Fe oxidation state is higher in the crystal than in the surrounding layer. The characteristic shake-up satellite of exclusive Fe^{3+}-containing phases (i.e., the peak at 718–719 eV) is not evident in the crystal's spectrum. The spectrum shows the features that correspond to a mixed Fe^{2+}-Fe^{3+} compound shown in the middle of the

[5]In the inset. The upper spectrum is relative to a FeO layer by oxidation of an Fe film grown by MBE; the middle spectrum corresponds to a film that contains both Fe^{2+} and Fe^{3+} cations [7]; the bottom spectrum was obtained from a pure α-Fe_2O_3 powder.

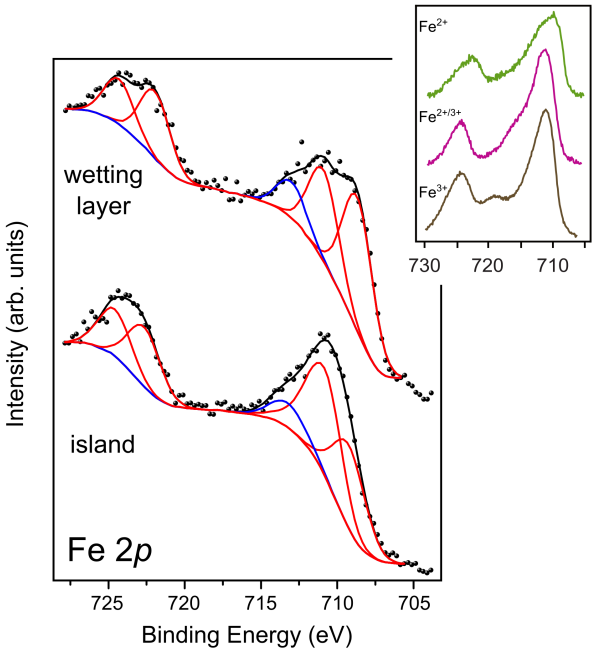

FIGURE 4.10: Fe 2*p* core-level x-ray photoelectron spectra acquired from the surface. The upper (lower) spectrum has been collected from the wetting layer (island). Experimental data (black dots) have been fitted using a black solid line originated from the sum of main photoemission (red lines) and shake-up (blue lines) contributions. The inset helps to a facile comprehension of the differences between FeO (green), Fe^{2+}/Fe^{3+}-containing compound (purple) and hematite (gray) XPS spectra. A non-linear background has been subtracted from the reference spectra [7].

inset in Figure 4.10, indicating that the crystal is a mixed valence iron oxide. This is consistent with the presence of magnetite phase and in agreement with the LEED measurements. Because the iron Fe spectrum has to be fitted using several components, its interpretation is not trivial and we cannot evaluate precisely the Fe^{3+}/Fe^{2+} ratio in the crystal[6].

Study of the magnetic properties

Taking advantage of the LEEM/PEEM capabilities [37, 211], we use the XMCD technique to reveal in-situ the magnetic order of the individual magnetite crystals. To measure the x-ray absorption (XAS) spectra for the magnetite crystal, an image of the secondary electron emission was collected while the photon energy was scanned over the Fe $L_{3,2}$ x-ray absorption edges (690–730 eV) in two different scans using opposite x-ray helicities. An example of a XAS image, acquired close to the Fe L_3 absorption edge, is shown in Figure 4.11a. The image intensity from the area corresponding to the magnetite crystal of Figure 4.9a was integrated and averaged for the two x-ray helicities, giving the XAS spectrum shown in Figure 4.12. The spectrum provides further support

[6]Magnetite is often non-stoichiometric.

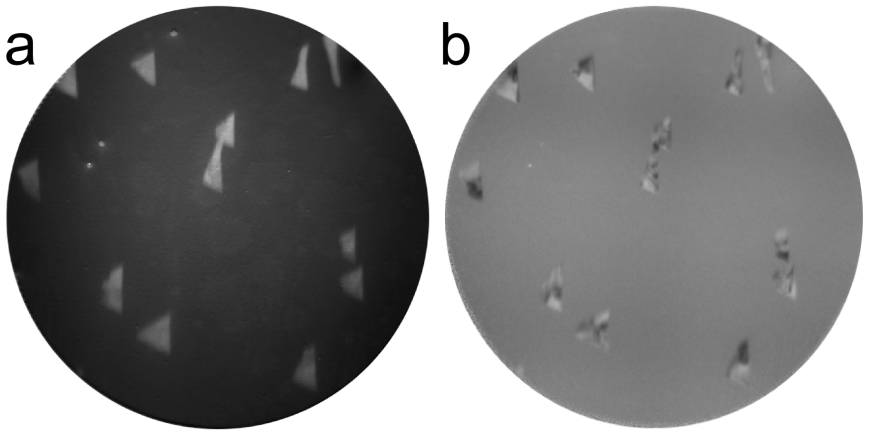

FIGURE 4.11: Large area XAS (**a**) and XMCD (**b**) images at 705.8 eV. In Figure b the XMCD signal is appreciable only at the crystal while the wetting layer has not magnetic circular dichroic contrast. The field of view is 30 μm.

that the observed triangular crystals are composed by magnetite [113, 182, 212]. As previously reported, a significant XMCD signal at the shoulder before the maximum of the L_3 XAS spectra has been observed in magnetite bulk samples as well as in thin films [112, 115, 213].

Taking XAS images at this photon energy (705.8 eV) with diffent helicities and subtracting them pixel by pixel results in the XMCD image of Figure 4.11b that shows well separated triangular crystals (all of which exhibit magnetic domains). The uniform gray intensity of the FeO wetting layer indicates that it has no magnetic circular dichroic contrast. We thus do not find any ferromagnetic order such as the one reported on FeO(111)/Fe(110) [214], in agreement with the antiferromagnetic order expected both in bulk FeO[7] and in ultra-thin FeO films [215]. However, the magnetite crystals show a clear dichroic contrast, proving that they have non-zero local magnetization. The magnetic domain arrangements (see Figure 4.12 and 4.13) are intricate, with long straight domains walls oriented along the {112} directions of the magnetite crystal. The two opposite domains marked as $M+$ and $M-$ (black and white in Figure 4.12) have a similar magnitude of the magnetization component along the illumination direction of the photon beam. The magnetization pattern persists during annealing up to 520 K, where changes of the surface topography are already detected.

In order to calculate the XMCD spectrum, only the area that corresponds to a given domain in a XAS image with a given helicity should be selected: a different XAS spectrum can be collected for each specific combination of domain type ($M+$, $M-$) and x-ray polarization ($P+$, $P-$). Thus, four different spectra were acquired: $I(+M,+P)$, $I(-M,+P)$, $I(+M,-P)$, $I(-M,-P)$. To avoid non-magnetic signals, the $I(+M,+P)$

[7] FeO is antiferromagnetic with a Néel temperature ranging between 203–211 K [12].

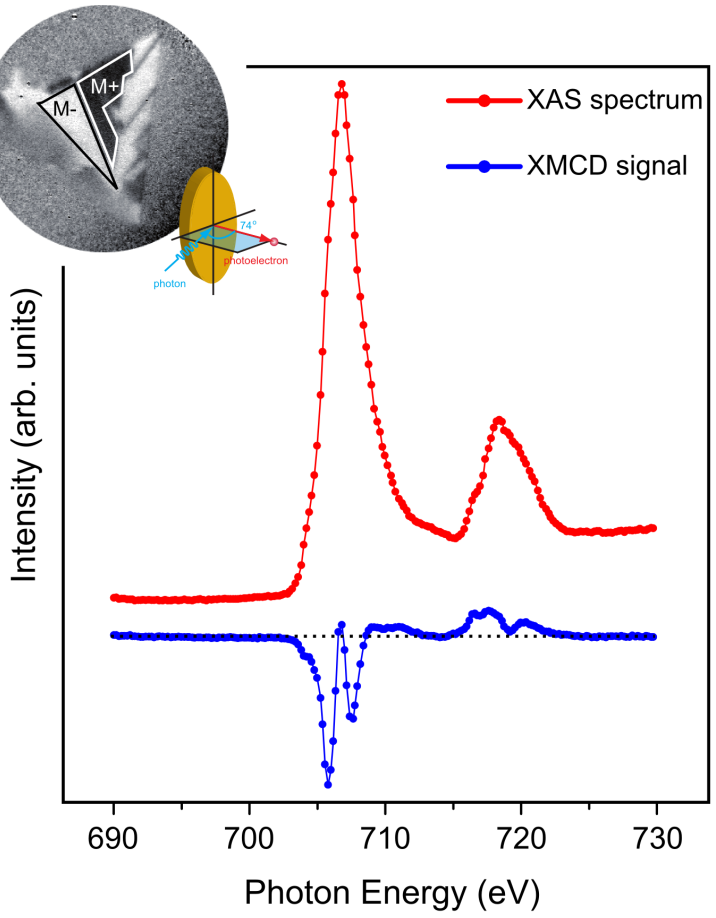

FIGURE 4.12: Fe $L_{3,2}$ x-ray absorption spectrum from the magnetite crystal (red line). The XMCD signal depicted in blue has been calculated using two opposite magnetic domains that have been indicated in the XMCD image on top-left. The inset describes the experimental geometry.

and $I(-M,+P)$ curves were subtracted together, as were the $I(+M,-P)$ curve and the $I(-M,-P)$ one. Then each of the two difference spectra for $+P$ and $-P$ are subtracted from one another, after normalizing by the difference in XAS intensity in the wetting layer to account for illumination differences. The result is the XMCD spectra presented in Figure 4.12 and 4.13b.

The resulting XMCD spectrum shows the typical three-peak structure of a magnetite-like spectrum [115, 216]: a negative peak at 705.8 eV mostly due to the contribution of Fe^{2+}_{oct} cations, a positive peak at 706.8 eV assigned to Fe^{3+} in tetrahedral position and finally another negative peak at 707.6 eV assigned to Fe^{3+}_{oct} cations [212, 213]. Acquiring XMCD images at energies corresponding to each of the peaks (see Figure 4.13a), the domains are imaged with the same contrast for each negative peak, and with reversed contrast for the positive peak. The opposite sense of the XMCD peaks from octahedral and tetrahedral sites reveals their mutual antiferromagnetic coupling. Thus, the observed magnetite crystals are ferrimagnetic like their bulk counterpart. When compared with

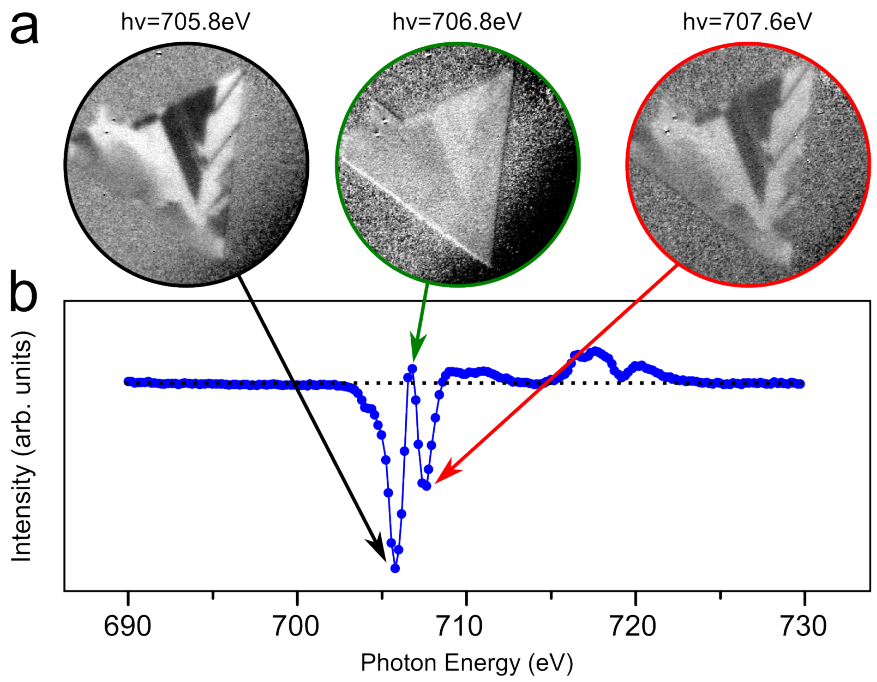

FIGURE 4.13: **a**. XMCD image sequence acquired at each of the peaks marked with arrows on the calculated $L_{3,2}$ XMCD spectrum (**b**). The field of view of the XMCD images is 4 μm.

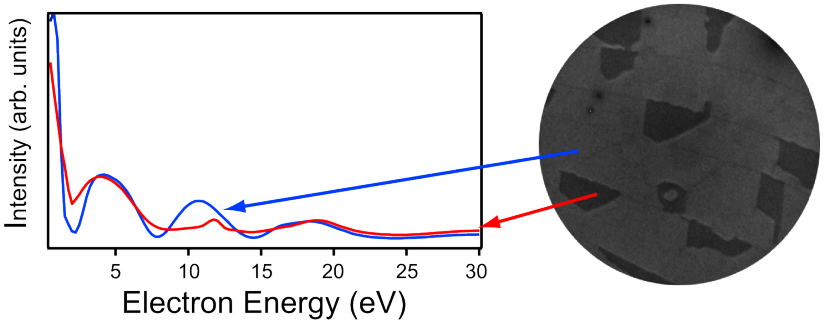

FIGURE 4.14: Electron reflectivity curves recorded from two regions of a continuous FeO film. The blue curve collected from the majority area (which appears light gray in the LEEM image on the right side) is attributed to a FeO bilayer. The red curve rises from the minority region (which appears in dark gray in the same LEEM image) is attributed to a single layer of FeO. The field of view of the LEEM image is 4 μm and the electron energy is 16.8 eV.

the reference spectrum [115], the tetrahedral peak is smaller and the octahedral Fe^{2+} peak is slightly larger. These small deviations may arise from contributions from the underlying FeO wetting layer or from an incomplete unit cell [159].

Thickness estimation

In this subsection, we explain how we measure the average thickness of an individual magnetite island. We take advantage from the 40-nm real-space resolution of PEEM in order to measure the attenuation of the photoelectrons emitted from the Ru $3d$ core level of the substrate when emerging through individual magnetite crystals. This procedure requires an accurate value of the mean free path of the electrons emerging from the surface at a given kinetic energy. For 400 eV photons the electrons from the Ru $3d_{5/2}$ core level exhibit a kinetic energy of E_k=120 eV. The attenuation of a single FeO layer was evaluated by comparing the spectral area of the Ru $3d_{5/2}$ core level from Ru measured through a FeO bilayer (2 ML_{FeO}) and through a single FeO layer (1 ML_{FeO}), as depicted in Figure 4.15a. The bilayer and single layer areas of FeO have been previously characterized, and are easily distinguished not only by the difference in the substrate core level attenuation but by their electron reflectivity (see Figure 4.14). The FeO bilayer (blue curve in Figure 4.14) exhibits an extra peak that is absent in the monolayer curve (red curve in Figure 4.14). We note that oscillations in the electron reflectivity–energy curve arise from the interface between electrons reflected from the film/substrate and film/vacuum interfaces, with each additional peak indicating one additional layer [217].

Using the experimentally determined mean free path for 120 eV electrons in FeO[8], the thickness of the Fe_3O_4 crystal was estimated to be 3.1±0.3 ML_{FeO} (see Figure 4.15c)). Considering the relative density of the Fe–O layer in magnetite and in FeO[9], and the thickness of the Fe–O layer in magnetite (0.242±0.06 nm[13]) yields a thickness for the magnetite of 1.0±0.4 nm[10].

To put this value in context, we note that the thinnest magnetite film grown on a metal substrate (with a similar FeO interface layer [13]) reported to date with a well defined bulk-like local magnetite structure, determined by Mössbauer spectroscopy, was around three times thicker that our islands [171]. In contrast, films of similar thickness have been reported to show a marked superparamagnetic behavior as described in the introduction. In fact, Eerenstein *et al.* [153] reported a superparamagnetic behavior in a 1.8 nm magnetite grown on spinel[11] films and invoked the presence of APBs in order to explain it. In our case we have no evidence of the presence of APBs and we consider their presence highly unlikely because our crystals are isolated from each other and arise from single nuclei. Indeed the formation of APBs has been observed in continuous layers resulted from the nucleation of several indipendet crystals. Thus, we suggest that our

[8] 1.25±0.02 ML_{FeO}

[9] Same oxygen density, 25% smaller iron density for magnetite.

[10] The larger relative error for the thickness in nm is due to the conservative estimate of the influence of the relative density of magnetite Fe–O layers in magnetite and FeO.

[11] MgO and $MgAl_2O_4$.

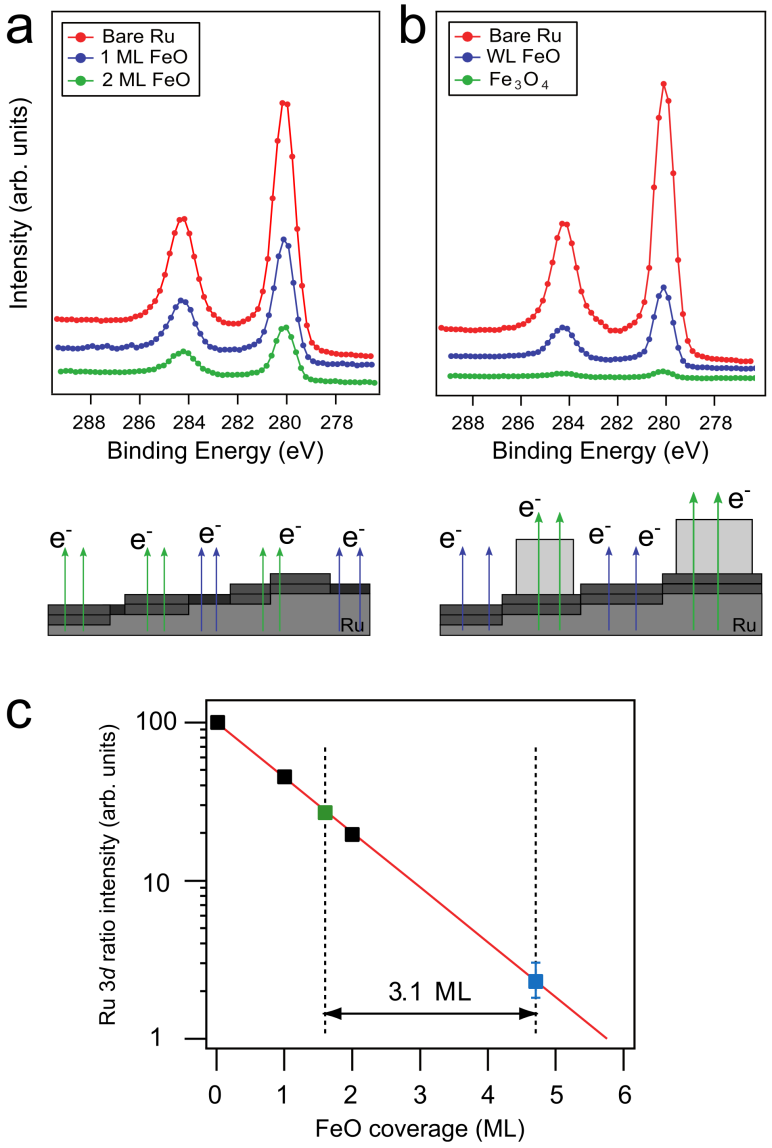

FIGURE 4.15: Determination of the magnetite crystal thickness. **a**. Ru 3*d* XPS spectra recorded from clean Ru, through a FeO monolayer and FeO bilayer, respectively. **b**. Ru 3*d* XPS spectra collected from clean Ru, through the Fe_3O_4 crystal and its surrounding wetting layer, respectively. The schematics below each spectra explain the experimental thin layer configuration. **c**. Semilogaritmic plot of the relative Ru XPS $3d_{5/2}$ peak area recorded from the different films versus coverage expressed in number of FeO layers. The black squares correspond to the values obtained from *a*. The calculated mean free path is 1.25±0.03 ML_{FeO} (red line in the semilogaritmic plot). The green and blue squares are relative to the values obtained from the spectra in **b** and correspond to the wetting layer and the magnetite crystal, respectively (error bars from the wetting layer are within the symbol size). The additional thickness of the magnetite crystal does not depend on the particular wetting layer thickness.

"single crystal" of magnetite present stable magnetization at room temperature (and even heating to 520 K) because it lacks APBs.

Orbital and Spin moments calculation

XMCD allow an element-selective separation of the spin and orbital contributions to the total magnetic moment of magnetic surfaces [112, 115, 218–220]. Thus, m_{orb} and m_{spin} can been calculated by applying the sum rules on the XMCD spectrum and averaged ($[-P]+[+P]$) XAS spectrum of Fe $L_{2,3}$ edges based on the Equations 4.2 and 4.1.

$$m_{orb} = -\frac{4q}{3r}N^h \tag{4.1}$$

$$m_{spin} = -\frac{(6p-4q)}{r}N^h \tag{4.2}$$

The p, q, and r values have been determined from the integration of the XAS and XMCD spectra, as described in Figure 4.16 while the N^h value, (N^h ~13.5±0.2), has been taken from the literature [112] and represents the total number of Fe $3d$ holes per formula unit. In order to discard non-magnetic contributions, an arctangent based step function has been subtracted from the averaged XAS spectrum [112].

For the orbital moment, the estimated value is m_{orb}=0.23 μ_B, while m_{spin}=1.25 μ_B for the spin moment, giving a total moment of $m_{orb+spin}$=1.48 μ_B. Although the total moment is quite smaller than most reported values (see Table 4.1), the resulting ratio, $\frac{m_{orb}}{m_{spin}}$=0.184, agrees well with some of the reported work. According with the discussion of Goering [109], the last results of Hari Babu and co workers [119], and the fact that the crystal has a thickness of ~1 nm, the reduced total moment might be explained by surface and interface effects. In fact, (i) the crystal surface presents a reconstruction in which the stoichiometry differs from Fe_3O_4 (*biphase* termination) and (ii) there is a FeO wetting layer underneath. The first argument could be considered in order to interpret the non-vanishing orbital moment. In fact, a variation of the stoichiometry and crystallographic structure can lead to a non-vanishing orbital moment [109]. While the second idea could suggest an interface interaction in which the Fe^{2+} cations of magnetite can be antiferromagnetically coupled with those of the wetting layer. This effect might to explain the smaller value of the spin moment.

The role of the iron flux

In this section we discuss the role of the iron flux during the iron oxide growth by O–MBE. In the previous Section 4.3 we observe the formation of nanometer-thick islands.

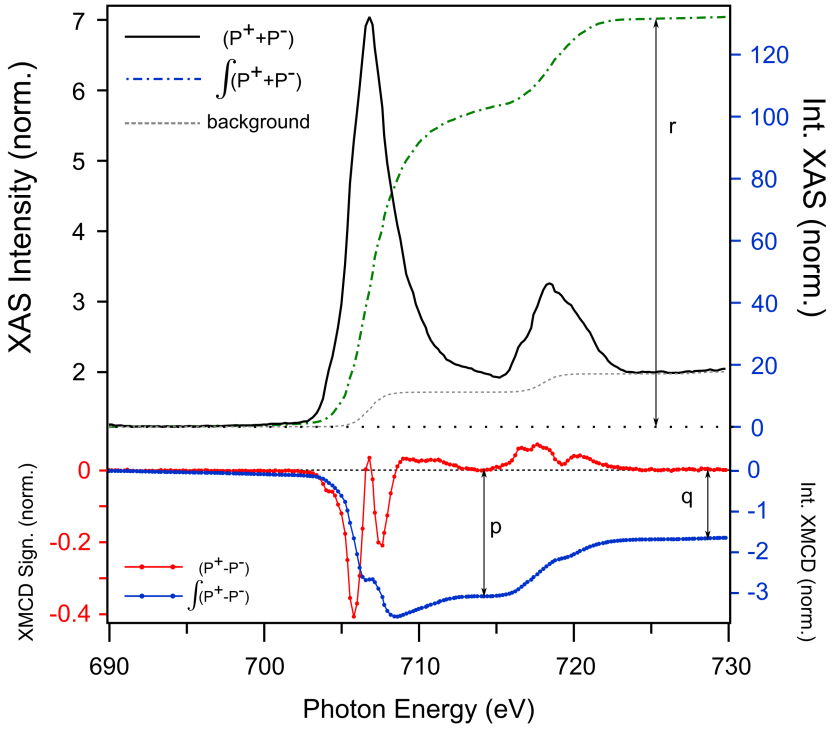

FIGURE 4.16: $L_{2,3}$-edge summed XAS (black) and XMCD (red) curves of Fe_3O_4 has been collected from the island shown in the Figure 4.3 inset. Their integration curves have been depicted in green and blue, respectively. The dotted gray line is the two-step-like function for the edge-jump removal before the integration of the summed XAS spectrum. The p, q, and r are the three integral values needed in the sum-rule analysis.

When further iron deposition takes place, an unexpected event has been observed by means of LEEM. In the first frame of Figure 4.17 several magnetite islands which appear light gray nucleate on the FeO wetting layer (darker gray). Following the growth, we observed a decrease of the island size (see the white arrows in Figure 4.17b) and, later, the complete disappearing of the magnetite islands has been registered. Further iron deposition produces a change in the electron reflectivity of the wetting layer (see Figures 4.17d and e) and it is followed by the nucleation of new triangular islands (blue arrows in Figures 4.17e and f).

Although, at first glance, these new islands might be interpreted as a renewed nucleation of magnetite crystals, diffraction and spectroscopic analysis reveal a surprising result. The LEED pattern (not shown) collected from the dark islands does not exhibit the (2×2) structure typical of $Fe_3O_4(111)$, and the spectroscopic analysis, summarized in Figure 4.18, suggest the presence of Fe^{2+} cations, exclusively. Moreover, the XPS Fe $2p$ core-level spectrum of the wetting layer shows a modest contribution that can be attributed to metallic iron and the XMCD image of the surface reveals a uniform gray intensity[12], i.e., they lack of magnetic contrast. All together, these results suggest

[12] Although a XMCD contrast is slightly observed in the corner of the smallest island shown in Figure 4.18, it is not comparable with that observed previously in the magnetite islands 4.13.

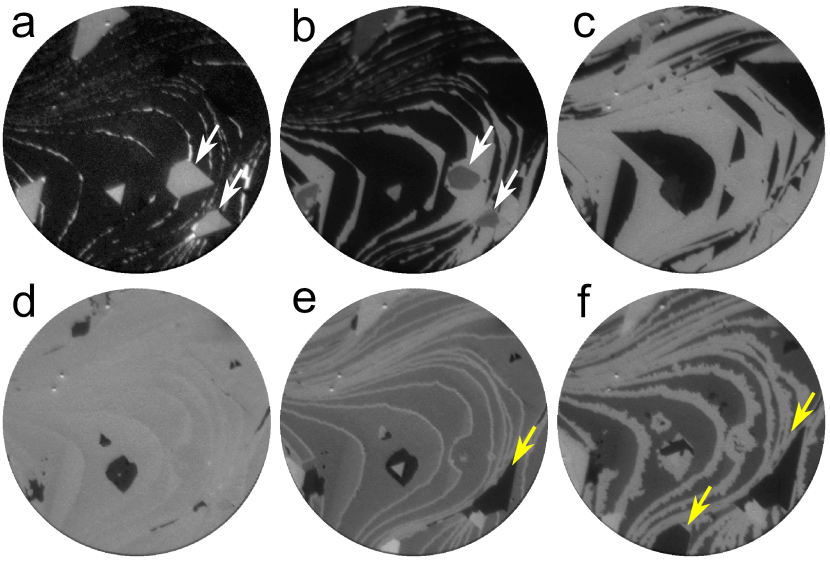

FIGURE 4.17: **a**–**f** Selected LEEM images from a sequence acquired during the growth of the magnetite crystals. The first three frames show the de-wetting of the magnetite islands, while in the last frames, a change of contrast is observed together with the nucleation of black irregular islands. The field of view is 10 μm and the electron beam energy is 19 eV.

that, under these experimental conditions, magnetite is not the stable phase and the subsequent Fe produces FeO islands.

This unexpected transition leads us to study the growth of the iron oxide phases as a function of the iron flux during the O–MBE experiment. Maintaining a fixed substrate temperature (∼870 K) and oxygen pressure (5×10^{-6} Torr), several growth experiments have been performed varying the iron flux.

First, a very low iron flux (3.2×10^{-4} ML s^{-1}) has been used in order to grow the sample. In this case the arrival ratio between the supplied oxygen atoms and the incoming iron atoms is 2400:1. The resulting iron oxide film is presented in Figure 4.19a, showing small irregular islands nucleated on the substrate after the dosing of 4.65 ML_{Fe}. Since the LEED pattern collected from the surface exhibits a (2×2) structure with a cell parameter of 2.97 Å, the results are compatible with the formation of small magnetite islands. Moreover, due to the absence of the typical FeO LEED pattern and the presence of the Ru(0001) LEED spots, the bright region surrounding these islands can be interpreted as ruthenium covered by absorbed oxygen.

Then, the iron flux has been increased up to 1.3×10^{-3} ML s^{-1} leading to an arrival ratio of 595:1. Under these conditions, the previously reported growth mechanism takes place, with triangular Fe_3O_4 islands nucleating on top of a FeO wetting layer (Section4.3). After the depositing of 7.5 ML_{Fe}, the iron oxide film appears composed by two phases (see

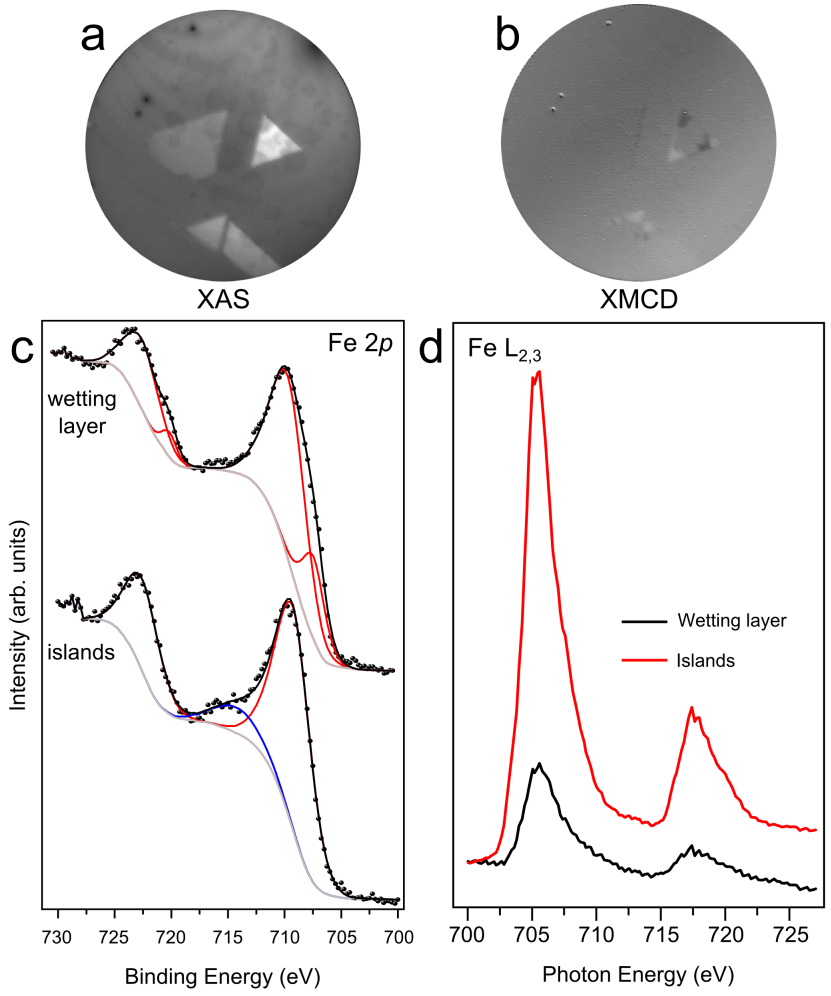

FIGURE 4.18: Summary of the spectroscopic measurements carried out for the iron oxide film described in Figure 4.17. **a** and **b**. XAS and XMCD images recorded at 705.0 eV and the field of view is 10 μm. **c**. Fe 2*p* XPS spectra recorded from the wetting layer and the islands. The experimental data (black dots) have been fitted using main photoemission (red lines) and shake-up (blue line) contributions. **d**. Fe $L_{2,3}$-edge XAS spectra collected from the islands and the surrounding region.

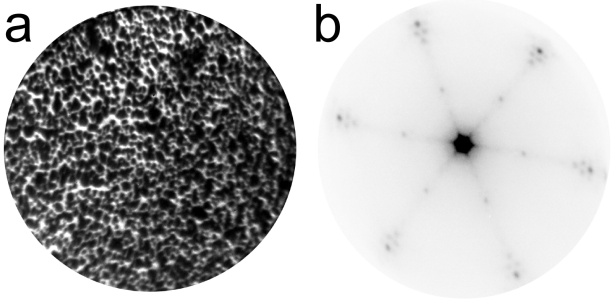

FIGURE 4.19: **a**. LEEM image shows magnetite islands nucleated on Ru(0001). The field of view is 10 μm and the electron energy 26.5 eV. **b**. LEED pattern collected from the same region. The unit cell parameter is 2.97 Å.

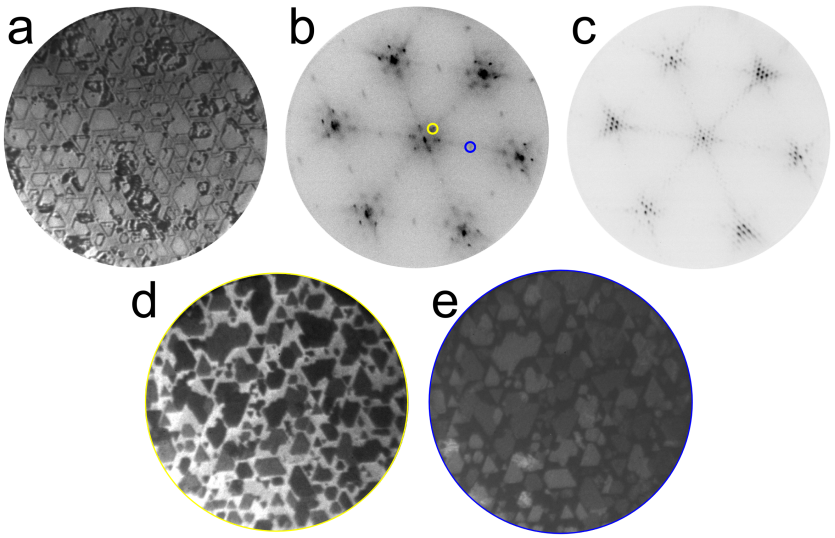

FIGURE 4.20: **a**. LEEM image shows magnetite triangular islands nucleated on Ru(0001). The field of view is 10 μm and the electron energy 13.0 eV. LEED patterns collected from the wetting layer (**b**) and an island (**c**) at 57.6 eV. *Dark-field* images collected using the diffraction spots labeled by yellow (**d**) and blue (**e**) circles, respectively. In both images, the field of view is 10 μm and the electron energy is 20.7 eV.

Figure 4.20a). Indeed, LEED patterns collected from the islands and the surrounding regions indicate that the former is characteristic of magnetite while the latter corresponds to FeO (see Figure 4.20b and c). Moreover, *bright-field* images recorded using the LEED spots characteristic of each phases confirm this interpretation (see Figures 4.20d and e). The comparison of these results with the previous experiment[13] in which magnetite islands disappear and FeO islands are grown at a later stage, suggests that the growth mechanism can be strongly influenced by the iron flux.

When the iron flux is increased up to 5.0×10^{-3} ML s^{-1}, the growth mechanism changes again and the formation of new nanostructures is observed. In Figures 4.21a and b, two LEEM images of stripe-shaped nanostructures growing on a wetting layer are presented. While the LEED pattern of the surrounding layer correspond to FeO (see Figure 4.21c), we were not able to interpret the diffraction pattern of the stripe structures (see Figure 4.21d).

The growth experiment has been repeated in another LEEM/PEEM[14] and a XAS-/XMCD analysis have been carried out. The XMCD image (see the inset in Figure 4.22) collected from the surface suggests the presence of ferromagnetic order and be consistent with magnetite. However, the XMCD spectrum exhibits only one peak at the L_2-edge (blue line in Figure 4.22), and corresponds to metallic iron [220].

[13] We remark that the iron flux in the early experiment was 2×10^{-3} ML s^{-1}.

[14] This experiment has been carried out in collaboration with A. Quesada, I. Kruz and co workers at the LEEM-PEEM beamline of the BESSY synchrotron facility.

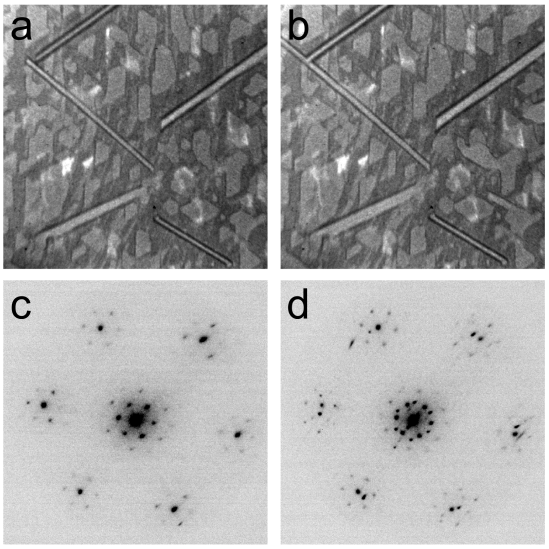

FIGURE 4.21: Monitoring of the stripes growth. LEEM images have been collected after dosing 20.3 (**a**) and 22.5 (**b**) ML_{Fe}. The field of view is 7 μm and the electron energy is 6.8 eV. Diffraction pattern collected from the stripe (**d**) and the surrounding region (**c**), at 50 and 40 eV, respectively.

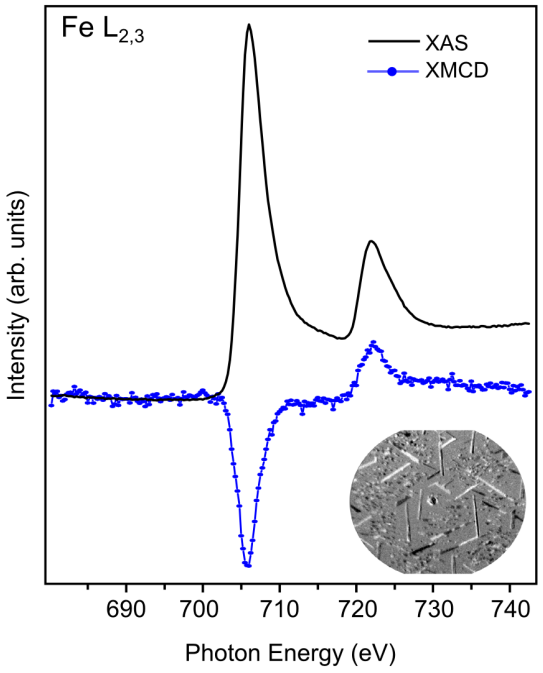

FIGURE 4.22: XAS (black) and XMCD (blue) Fe $L_{2,3}$-edge spectra recorded from a stripe. The inset shows an XMCD image of the surface. The field of view is 20 μm and the photon energy is 708.2 eV.

The formation of metallic iron nanostructures can be explained considering that the iron atoms that reach the surface cannot be oxidized at these experimental conditions. Moreover the arrival ratio of the oxygen molecules respect with the incoming iron atoms is about fifteen times lower (155:1). Different arguments can be proposed in order to explain these growth mechanisms. Considering the first experiment, the growth begins with the formation of a FeO layer and the further nucleation of magnetite islands. In the initial stages, iron atoms can be easily oxidized by the atomic oxygen chemisorbed on Ru(0001). The sticking coefficient on FeO and Ru are expected to be different: oxygen is not expected to be easily dissociated on the FeO surface. Thus, the iron atoms reaching the surface should have lees oxygen available compared to iron landing on Ru as in the initial stages of the growth. In the following stages of the growth, the magnetite stoichiometry could not be maintained leading to the decomposition of magnetite and the growth of FeO islands. When the iron flux is decreased, the magnetite stoichiometry can be preserved as it has been shown in Figure 4.20.

4.4 Summary

In this chapter we have introduced the properties of magnetite ultra-thin crystals grown on Ru(0001) prepared by oxidation of a metallic precursor. Using STM, LEED and XPS we have established that magnetite can be a stable iron oxide phase even when the film thickness is ∼1 nm. Then, we have grown one-nanometer-thick crystals of iron oxide on Ru(0001) using a different deposition technique (O–MBE). The growth has been observed by LEEM. By means of LEED, XPS, and XAS we have characterized *in-situ* the film establishing that the nanometer-thick crystals are magnetite-like. XMCD reveals that individual crystals have ferrimagnetic order up to 520 K.

Taking into account all these results we can confirm that magnetite's robust magnetism can be preserved at the nanometer limit if the growth is controlled and Fe_3O_4 crystals free of APBs and grown from a single nuclei is obtained.

We have then estimated the orbital and spin moments of the magnetite islands. Although the resulting magnetic moment is reduced relative to the bulk value, we proposed that the influence of an underlying FeO layer and the magnetite surface reconstruction might be the origin of the reduced moment.

Finally, the growth of iron oxide has been carried out at different iron fluxes. These results suggests that, the stoichiometry of the iron oxide is strongly affected by the iron flux during an O–MBE experiment.

Chapter 5

Oxidation Mechanisms in Iron Oxide Ultrathin Films

5.1 Introduction

In the previous chapters the principal properties of wüstite (FeO) and magnetite (Fe_3O_4) have been introduced. Now, we briefly offer a description of α–Fe_2O_3 and γ–Fe_2O_3. These two polymorphs of the Fe^{3+}-containing iron oxides have attracted much attention due to their chemical and physical properties.

Hematite (α–Fe_2O_3)

α–Fe_2O_3 is the most thermodynamically stable iron oxide polymorph under ambient conditions. As represented in Figure 5.1a, hematite exhibits a corundum lattice (i.e., a rhombohedrally centered hexagonal structure), characterized by a close-packed oxygen arrangement in which $\frac{2}{3}$ of the octahedral sites are occupied by Fe^{3+} cations [12]. Two Fe^{3+}_{oct} cations are followed by one vacant in the (001) basal planes while the tetrahedral sites remain unoccupied. The lattice parameters are a=5.0356 Å, c=13.7489 Å and the unit cell accommodates six formula units. The arrangement of cations produces pairs of $Fe(O)_6$ octahedra that share edges with three neighboring octahedra located in the same plane. Moreover, these $Fe(O)_6$ pairs share one face with an octahedron in the adjacent plane. This face-sharing along the *c*-axis introduces a distortion in the cations sublattice, so Fe atoms in octahedra with shared faces are repelled along the direction normal to the (0001) basal plane. As depicted in Figure 5.1b, the octahedron is trigonally distorted producing two types of Fe–O bonds with different length [221, 222].

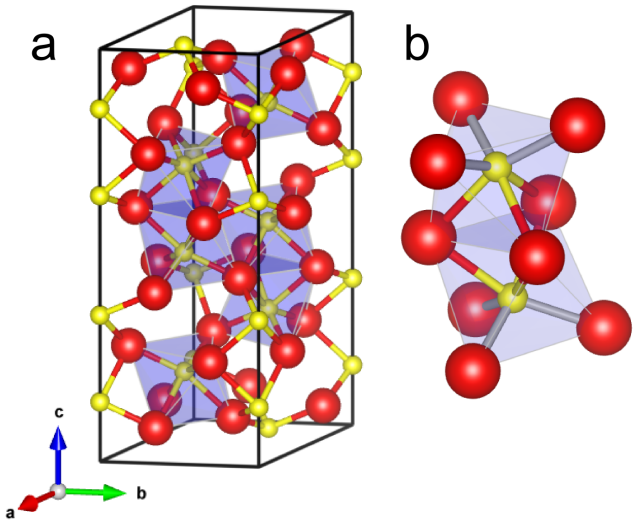

FIGURE 5.1: **a**. The unit cell of hematite shows the octahedrally coordinated Fe_2O_9 dimers forming chains along the c direction. **b**. A detailed view of one Fe_2O_9 dimer shows how the electrostatic repulsion of the Fe^{3+} cations produce long (gray) and short (red-yellow) Fe–O bonds. In both figures iron cations (oxygen anions) are depicted in yellow (red) colors.

The arrangement of the oxygen anions and the iron cations naturally influences the orientation of the spin moment of the iron atoms and thus the hematite magnetic properties. While hematite is paramagnetic above 956 K, at room temperature it is antiferromagnetic. Because the basal plane accommodates two interpenetrating antiferromagnetic sublattices that are not exactly antiparallel, a weak ferromagnetic behavior occurs[1]. Hematite undergoes a phase transition to a complete antiferromagnetic state at 260 K, the Morin temperature (T_M). At room temperature, the spin alignment shows the trivalent iron cation antiferromagnetically coupled across the shared octahedral faces along the *c*–axis (dashed blue line in Figure 5.2a). Above the Morin temperature, the competition between the weak magnetic anisotropy of the trivalent iron cations and the dipolar anisotropy produces a spin reorientation along the trigonal or *c*–axis of the rhombohedral lattice (see Figure 5.2b) [223]. However, the magnetic behavior of hematite, including the values of T_M and T_N, can be affected by several factors, such as external conditions (pressure or magnetic fields), lattice defects, impurities, or surface phenomena [221].

Although the catalytic activity of hematite has been studied in several reactions (water gas shift reaction (WGSR) [56] or CO hydrogenation [224–227]) during the last three decades, new attention has been devoted to this iron oxide phase because its possible application in photocatalysis. Photoelectrochemical (PEC) cells have the ability to convert the sun radiation in stored chemical energy through the dissociation of water into O_2 and H_2. As in conventional water electrolysis, oxidation takes place at the anode

[1]This deviation is called parasitic ferromagnetism. In hematite this effect is due a spin canting angle of $<0.1^\circ$ between its sublattices.

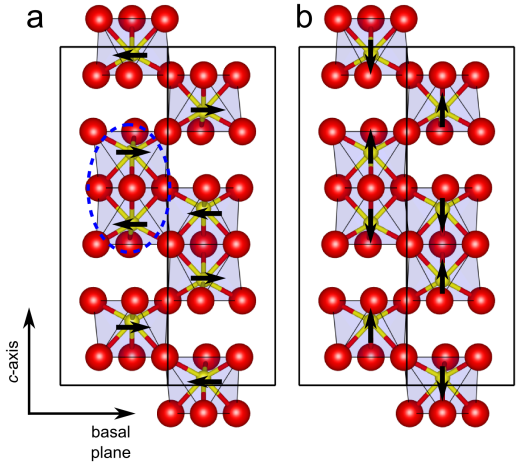

FIGURE 5.2: Spin ordering in hematite above (**a**) and below (**b**) T_M=260 K. The oxygen anions are represented by red spheres while the iron cations by yellow spheres. The unit cell, the octahedral sites and the *c*-axis have been outlined.

and the reduction occurs at the cathode. One or both electrode are semiconductors in which photogenerated carriers operate the water splitting reaction [222].

Because its semiconductor character with an band gap of approximately 2.0–2.2 eV, α–Fe_2O_3 has been considered a suitable material for PEC. In addition, its optical properties with broad absorption in the visible range, an appropriate valence band position proper for water oxidation, a thermodynamic stability coupled with its abundance and non-toxicity make hematite a promising material for the preparation of photo-electrodes for photoelectrochemical cells [228–232].

At the same time, specific limitations that prevent a high solar light harvesting efficiency such as low rate constant of water oxidation, the short hole diffusion length, and poor conductivity are being addressed. In this regard, deposition of ultrathin hematite film on specific conductive nanostructures has be suggested [233] in order to improve the efficiency of the electrodes [232, 234–236]. Despite these inconveniences, Sivula and co workers are optimistic and define hematite as unique and an obvious choice for the production of photo-electrodes [222].

From a strictly surface science point of view, α–Fe_2O_3 surfaces have been prepared and investigated starting either from bulk crystals [206, 237, 238] or thin films [13, 83, 93, 203, 239–243]. Since the common surface techniques usually require a conductive specimen (i.e. are based on the electron-surface interactions), the analysis of a non-conductive surface is severely hampered. In order to overcome this inconvenience, the preparation of α–Fe_2O_3 is frequent in thin film form on a metal substrate by two methods: (i) the oxidation of a metallic Fe film in molecular oxygen atmosphere [13, 241], or (ii) the direct growth of hematite using atomic-oxygen-assisted MBE [70, 83, 242, 244, 245].

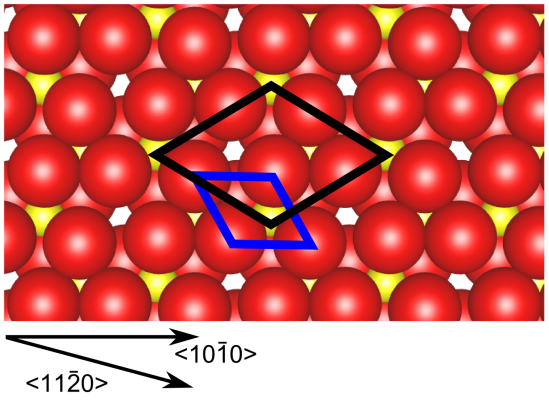

FIGURE 5.3: Atomic arrangement of the α–$Fe_2O_3(0001)$ unreconstructed surface. The surface unit cell of hematite is outlined in black color while the unit cell of the oxygen lattice in blue color. The oxygen atoms are represented by red spheres while the iron atoms by yellows spheres. The crystallographic directions in real space are indicated.

Because the first method requires high O_2 partial pressures (10^{-3} Torr range [13]) that sometimes are not compatible with UHV conditions, the latter method is preferred for the preparation of hematite thin film because it operates at lower pressures.

By means of the preparation of hematite thin films, new information on structural changes of these films occurring during oxidation or reduction have been described, until then unexplored using surface science techniques. Great interest has been dedicated to the α–$Fe_2O_3(0001)$ surface (represented in Figure 5.3) and its properties when prepared or treated in ultra-high vacuum conditions [168, 206, 246, 247]. Although hematite is the most stable iron oxide phase, its surface composition and structure depends markedly from the preparation methods. It has been demonstrated that a well-defined stoichiometric surface is difficult to obtain when hematite (both bulk and thin film) is cleaned in UHV by following the common protocols (i.e., Ar^+ sputtering and annealing in O_2). Instead, a non-stoichiometric "biphase" is commonly observed consisting of islands of hematite and $Fe_{(1-x)}O$. The coexistence of these two oxide phases has been observed for the first time by Condon and co workers and has been called *biphase ordering* [168, 206, 248, 249]. Although the initial results have been interpreted in terms of the coexistence of hematite and magnetite phases, the formation of a $Fe_{1-x}O$ phase seems to be more favorable respect the formation of magnetite. However, the interpretation remains an open question and still is under debate, such as demonstrated by recent experimental [246] and theoretical studies [250].

Maghemite (γ–Fe_2O_3)

"Magnetic-hematite" was discovered in the early 19^{th} century by the pioneers of solid-state chemistry and distinguished from the hematite exactly for its magnetic character [251]. Lately called maghemite, γ–Fe_2O_3 exhibits a similar structure to that of Fe_3O_4. Both maghemite and magnetite present a spinel crystal structure, but while the latter contains Fe^{2+}/Fe^{3+} cations, in maghemite all the iron cations are trivalent and the charge is balanced by the inclusion of vacancies [12].

The maghemite unit cell is cubic with a parameter a=0.834 nm and contains 32 oxygen anions, and $21\frac{1}{3}$ trivalent cations. Considering that these vacancies are confined to octahedral interstices, maghemite structure can be summarized by the formula relative to the spinel structure:

$$\left(Fe^{3+}\right)_8 \left[Fe^{3+}_{5/6}\square_{1/6}\right]_{16} O_{32} \tag{5.1}$$

where $\square$ represents atomic vacancies, and the brackets ( ) and [ ] designate tetrahedral and octahedral sites, respectively. Depending on the degree of long-range order in the distribution of the cation vacancies, the macroscopic symmetry of the crystal varies from cubic to tetragonal. The ordering of the iron vacancies in the octahedral holes has been the subject of research for several decades and, unfortunately, is not yet completely understood [252–255]. In particular, the role of the preparation conditions in the distribution of these vacancies is unclear.

The maghemite structure influences also the electric behavior. As described previously, the conduction mechanism in magnetite is driven by electron hopping between trivalent and divalent cations octahedrally coordinated. Because of the absence of Fe^{2+} cations in the maghemite structure, the conduction is hindered making the material an insulator[2].

Maghemite magnetism is due to the two sublattices of Fe octahedrally and tetrahedrally coordinated coupled ferromagnetically within the same sublattice. Thus, maghemite has a ferrimagnetic character that arises from antiparallel coupling between the two different sublattices. The measurement of maghemite's Curie temperature is difficult because it transforms to hematite at temperatures close to 700–800 K. Despite this, T_C has been estimated to be in the range 820–986 K. Due to its ferrimagnetic behavior at room temperature, γ–Fe_2O_3 has long been used as a magnetic recording material [257, 258]. Synthetic maghemite particles absorbed in a polymeric matrix have been adopted as coating of tapes and disks from 1950s until ca. 1990. These single-domain particles were preferred to magnetite particles (with better magnetic properties) because magnetite ones undergo oxidation to hematite.

[2] At room temperature a maghemite thin film exhibits a resistivity value of $\sim 10^4$ Ω cm, which is several orders of magnitude higher than magnetite's resistivity [256].

Although γ–Fe_2O_3 has largely been used as a recording material, less efforts have been dedicated to the preparation and study of this iron oxide phase, using a surface science approach. Certain aspects of maghemite properties remain unclear or conflicting because difficulties of access to bulk single crystals. Thus, a proposed solution is the preparation of well-ordered, stoichiometric and high-purity epitaxial thin films [83, 203, 240, 244, 259–261]. As in the case of hematite, surface science studies were initially devoted to describe the experimental conditions required for maghemite synthesis, while lately to the application of maghemite in spintronic devices. Due to its magnetic and electrical properties, γ–Fe_2O_3 has been suggested as candidate to substitute materials with a low T_C for the fabrication of magnetic tunnel junctions [255, 260].

Nevertheless, the preparation of high quality maghemite films is not trivial due to its metastable character, i.e. maghemite transforms irreversibly into hematite. Thin film structures have usually been prepared by unconventional MBE techniques such as NO_2-assisted MBE, O_3-assisted-MBE or oxygen-plasma-assisted-MBE. Indeed these techniques allow to operate at lower temperatures and partial gas pressures (i.e. far from the thermodynamic equilibrium) avoiding the formation of the more stable hematite phase. Usually, the preparation of γ–Fe_2O_3 films has been carried out by the oxidation of previously grown magnetite films. It is well established in magnetite oxidation that, under adequate conditions, Fe^{2+} cations migrate towards the surface where an oxidation reaction takes place. This mechanism occurs together with the formation of octahedral vacancies and the subsequent transformation into maghemite. The oxidation process is reversible and has been observed both in bulk [12] and in thin films [262, 263].

We have to remark that surface science studies about iron oxide thin films often ignore the possibility of maghemite formation. An example is given by the study of magnetite film oxidation reported by Deng and co workers [243]. In their discussion, only the hematite phase was considered because according to the authors, it is the stable iron oxide in bulk, excluding the possible formation of the gamma phase. Their arguments are only based in the assumption that maghemite is metastable. This example disagrees with experimental evidence that demonstrate how metastable iron oxide phases might easily be rendered stable when prepared in ultrathin film form. Fortunately, the literature shows several surface science works in which also metastable phases, like maghemite, have been identified [84, 259, 264, 265].

5.1.1 Oxidation Mechanisms

As anticipated in the introduction and in the previous chapters, the different transformations of iron oxides have been the subject of many studies. Considering the wide range

of magnetic and electric properties exhibited by iron oxides (summarized in Table 5.1), the prediction of which phase is more stable under a particular experimental condition becomes crucial when a desired characteristic is required.

An example is provided by the interesting discussion about the Fe_3O_4 crystal oxidation [266–268]. Colombo and co workers interpreted this oxidation reaction as a two-step process [269, 270]. The first step is a topotactic reaction leading to the intermediate phase, $Fe_{(3-x)}O_4$. During the second stage, the disordered samples oxidize readily to maghemite, and hematite formation only occurs when α–Fe_2O_3 particles or stacking faults are present. On the other, Gallagher and co workers, proposed a different mechanism based on the diffusion of iron cations [266, 267]. They observed that magnetite particles underwent directly a phase transformation to hematite without observing the formation of maghemite. Because no traces of hematite were detected by Gallagher, he suggested that the mechanism of the magnetite oxidation is sensitive to the purity and grain size of the sample. In fact, Colombo used a natural crystal (probably with impurities) while Gallagher used a pure synthetic magnetite crystal.

Formula	Oxygen lattice	Nominal iron valence	Magnetic order	O-O lateral distance (nm)	Electric behavior
FeO	fcc	2+	AFM	0.305	Ins.
Fe_3O_4	fcc	2+/3+	FM	0.297	Cond.
γ-Fe_2O_3	fcc	3+	FM	0.295	Ins.
α-Fe_2O_3	hcp	3+	canted-AFM	0.295	Sem.

TABLE 5.1: Summary of iron oxides characteristics (adapted from Ref.[12] and [13]). Ins: insulator. Cond: conductor. Sem: semiconductor. AFM: antiferromagnetic. FM: ferrimagnetic.

Although most of the published results are based on powder or polycrystalline samples, the oxidation mechanism has recently been studied from the surface science point of view using oriented magnetite crystals [35, 271]. In particular, we been studied the oxidation of a (001) magnetite crystal. By monitoring its morphology during exposure to oxygen at ∼900 K by LEEM and its composition by Raman spectroscopy, we have observed that magnetite is being converted to hematite without the formation of a maghemite phase [35].

As we already described, the preparation of thin film may stabilize iron oxide phases that are metastable in bulk, such as FeO or maghemite. For example, the oxidation reaction of FeO thin film has extensively been investigated by Weiss *et al.* [13]. Moreover, magnetite to maghemite transformations in thin films on Pt(111) [50], Ag(111) [272] or W(110) [273] have also been studied. Nevertheless, the study of oxidation (reduction) reactions on iron oxide thin films remains a challenging work.

Considering the complexity of iron oxide systems in thin film form, a single spectroscopy or structural measurement does not provide enough information in order to get an unequivocal description of these systems. Therefore, an experimental approach combining microscopy, structural and spectroscopic techniques, is appropriate, such as suggested by the words of R.M. Cornell and U. Schwertmann in their reference book *"The iron oxides"* [12].

> *"Ideally, a phase transformation should be investigated using a combination of techniques which enable changes in composition, structure, surface area, morphology and porosity of the solid phases and in the composition of the solution to be monitored, together with the reaction kinetics. This type of comprehensive investigation is rare for iron oxide interconversions; in most cases only one or two of the above aspects of the transformation have been considered."*

In the previous chapters we introduced the growth mechanism of FeO(111), Fe_3O_4(111) and FeO/Fe_3O_4 phases on Ru(0001) using MBE and O–MBE. Thereafter, we characterized them using a combination of several surface-sensitive techniques. In this chapter a combination of nanometer-resolution characterization tools allows to illustrate the oxidation pathways of the different iron oxides.

5.2 Experimental Results

Film Morphology and Structure

We start preparing a Fe_3O_4/FeO system on Ru(0001) using O_2-assisted MBE at 900 K and with a iron flux of 0.2×10^{-3} ML min^{-1}. As reported in the previous chapter, the growth mechanism proceeds at the given pressure (1×10^{-6} Torr), by the initial nucleation of small FeO islands (see Figure 5.4b). The coalescing of these islands produces a complete FeO layer. In the final stages of the sample preparation, the nucleation of micrometer wide triangular islands is observed (see Figure 5.4d).

Nevertheless, electron diffraction analysis were repeated in order to check the structure of the different surface regions. We confirmed by selected area LEED that the wetting layer is composed by FeO(111) (see Figure 5.5b) while the islands have the Fe_3O_4(111) common structure (see Figure 5.5c). The FeO satellites have a real-space distance of 18 Å while the integer spots correspond to an hexagonal unit cell of 3.2 Å. At the island (see Figure 5.5c), the integer spots are located at the same position as the wetting

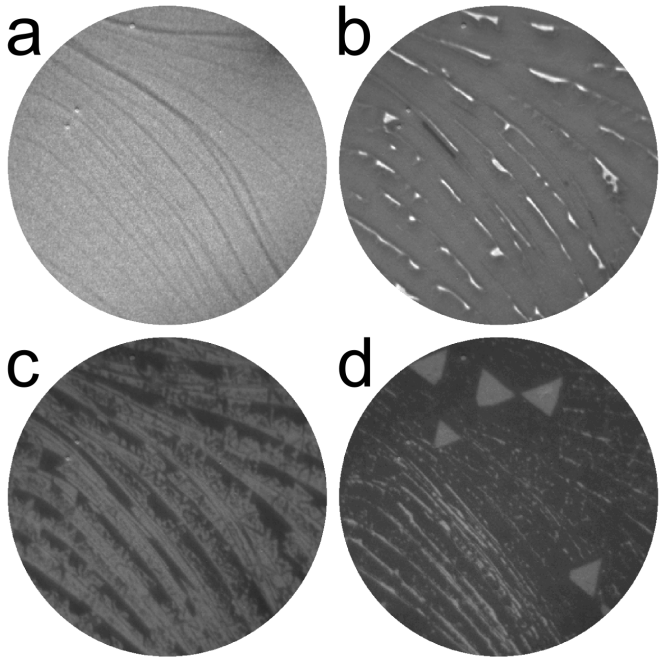

FIGURE 5.4: **a**–**d** LEEM images collected during the growth of Fe in O_2 background. The field of view is 10 μm and the beam energy is 19.0 eV. The deposited amount of iron is 0, 1.7, 2.0 and 2.3 ML_{Ru}.

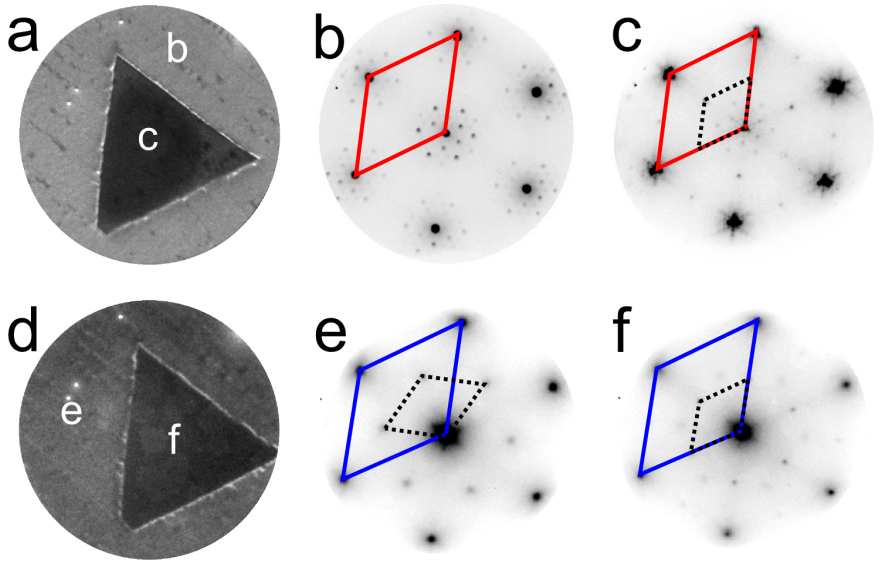

FIGURE 5.5: LEEM images from the as-grown (**a**) and the oxidized (**d**) island. LEED patterns registered from wetting layer (**b**), as-grown island (**c**), oxidized wetting layer (**e**) and oxidized island (**f**). LEEM field of view is 4 μm and the electron energy is 4.5 eV. LEED patterns have been collected at 30 eV (b,c) and 48 eV (e,f). The reciprocal in-plane unit cells have been depicted.

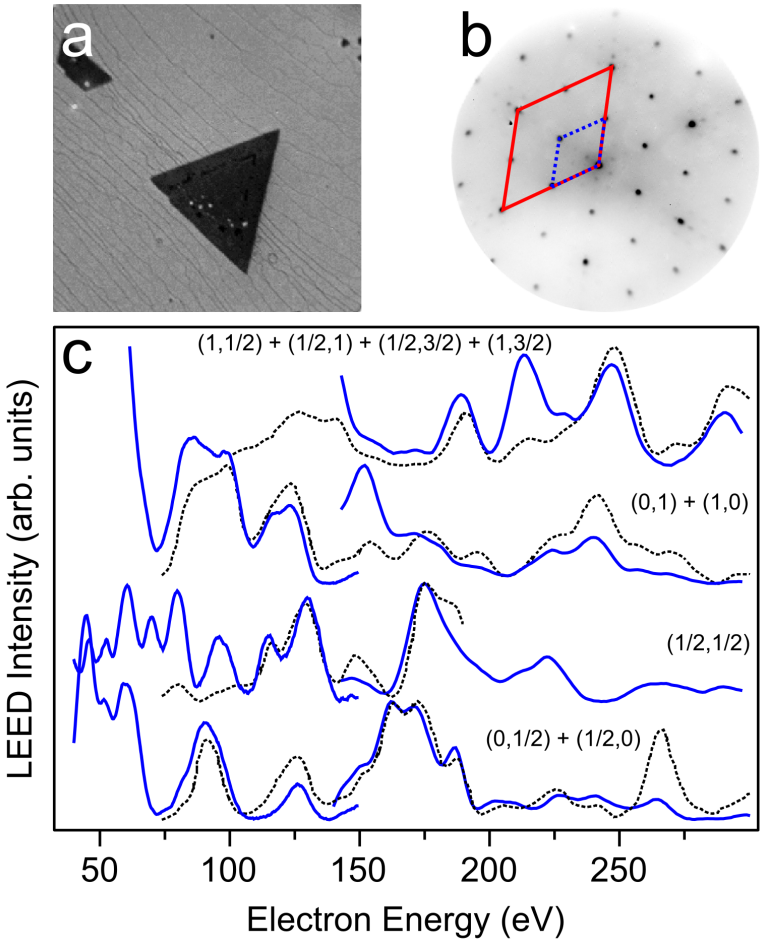

FIGURE 5.6: Intensity profiles of the magnetite LEED spots after a mild NO_2 treatment. A typical triangular magnetite island has been shown in **a**. The field of view is 7.1 μm^2 and the electron energy is 3.5 eV. **b**. LEED pattern from a magnetite island obtained by the sum of several LEED images collected at different energies. In red, the first order unit cell has been outlined, while the dashed blue line represents (2×2) structure. Comparison of experimental LEED spot profiles taken from a Fe_3O_4 island (blue lines) with a study (dashed black lines) of an unreconstructed bulk termination reported by Weiss and co workers (Figure 4 in ref. [8]).

layer, so the unit cell remains unchanged. However, the periodicity of the moiré is much larger (smaller spacing in reciprocal space), with a distance of 52 Å. This superstructure has been related with a magnetite (111) surface reconstruction [206, 207, 246, 249]. In addiction, weak 2×2 spots can be observed at specific energies which arise from either magnetite or maghemite.

In subsequent steps, the surface has been exposed to 1×10^{-8}–1×10^{-6} Torr of NO_2 and gently annealed in order to favor an oxidation reaction. As explained in the experimental chapter, NO_2 has been preferred to the conventional molecular oxygen gas because its higher oxidation efficiency.

Initially, we apply a gentle oxidation treatment by annealing at T<670 K and a NO_2

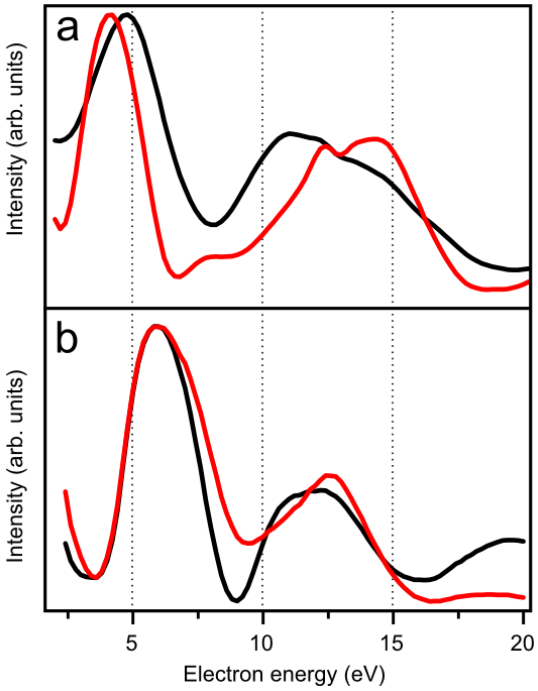

FIGURE 5.7: **a**. Electron reflectivity spectra recorded from the wetting layer (red) and the as-grown island (black). **b**. Electron reflectivity recorded from the oxidized wetting layer (red) and the oxidized island (black). All the spectra have been normalized to the maxim in order to enhance the differences.

pressure in the $\sim 10^{8}$ Torr range. The morphology of the film after this "gentle" treatment remains unchanged: large triangular islands on a wetting layer. In Figure 5.6c, we show the plot of each diffracted beam intensity (see Figure 5.6b) versus the beam energies recorded from a triangular magnetite island (see Figure 5.6a) by means of an illumination aperture. The LEED I-V (blue lines in Figure 5.6c) are in good agreement with those reported by Ritter and Weiss in their study about the $Fe_3O_4(111)$ surfaces [8] (dashed black lines in Figure 5.6c). According to this, after mild oxidation our islands exhibit an unreconstructed magnetite bulk termination which exposes $\frac{1}{4}$ of iron atoms tetrahedrally coordinated to the oxygen lattice. It has been reported that these trivalent iron cations are relaxed inward towards the underlying close-packed oxygen layer by 41% respect to the bulk value, and the next three interlayer spacings below the topmost layer also are strongly relaxed [173]. This relaxation effect has been interpreted as a mechanism that permits a stabilization of the magnetite polar termination, ad it has also been observed in other iron oxide surfaces, such as FeO(111).

Further exposure at a higher NO_2 pressure ($\sim 10^{-6}$ Torr range) again did not change the morphology as demonstrated by the two LEEM images recorded before (Figure 5.5a) and after (Figure 5.5d) the oxidation experiment. There are, however, changes in the electron reflectivity curves recorded from the oxidized film, as can be seen comparing Figures 5.7a and 5.7b. These variations of the electron reflectivity are accompanied by

a variation in the LEED patterns. Both regions, wetting layer and island, still present different LEED patterns, confirming that the film remains bi-component (i.e., islands and surrounding area have different structures). No satellite spots have been detected in the oxidized film. As shown in Figure 5.5, the wetting layer pattern (e) presents a $(\sqrt{3} \times \sqrt{3})R30°$ superstructure, while the island (f) still displays a (2×2) motif. The oxygen-oxygen lateral distances appear slightly contracted to 3.0 Å and 2.9 Å, and a small rotation of 3° between the island pattern and the wetting layer (which in turn is aligned with all the previous LEED patterns) is detected.

In summary, before NO_2 oxidation the wetting layer and the islands are composed by FeO(111) and Fe_3O_4(111), respectively. The latter has a reconstructed surface characterized by a *biphase* termination. A mild NO_2 exposure produces an improvement in the magnetite island crystalline order, as confirmed by LEED I-V. After this step, the magnetite surface is unreconstructed. After a more decisive oxidation step, the electron reflectivity and the LEED patterns still indicate a bi-component film, but with LEED pattern associated to hematite (wetting layer) and either magnetite or maghemite (islands).

Film Composition and Chemical State

As we previously demonstrated, XPS is a essential tool that can be utilized for iron oxides identification. XPS spectra have been extracted from a series of images acquired at a kinetic energy range of 90–120 eV with a photon energy of 825 eV. Thus, the integration of the image intensity permits us to measure the XPS $2p$ core-level spectra from different regions of the surface. Four Fe $2p$ XPS spectra recorded inside or outside a triangular island, before and after the NO_2 treatment, are shown in Figure 5.8.

The spectra from the wetting layer and the island collected before the oxidation have been described previously in the magnetite chapter 4. Now, we describe the Fe $2p$ spectra obtained from the oxidized film that are shown in Figure 5.8c and d. Neither of these new spectra have the characteristic shape of magnetite. In fact, the typical Fe^{2+} shake-up structure in the high binding energy side of the Fe $2p_{\frac{3}{2}}$ line disappears in the spectra of the oxidized film. Instead, another broad peak (blue line in Figure 5.8c and d) separated by approximately 8–9 eV from the main photoemission Fe $2p_{\frac{3}{2}}$ peak is observed. This feature, arising from electron shake-up interactions, is typical of the spectra of Fe^{3+} oxides. All these results clearly suggest that the NO_2 treatment promotes an oxidation reaction of both the FeO wetting layer and Fe_3O_4 island to iron phases containing mostly trivalent iron cations.

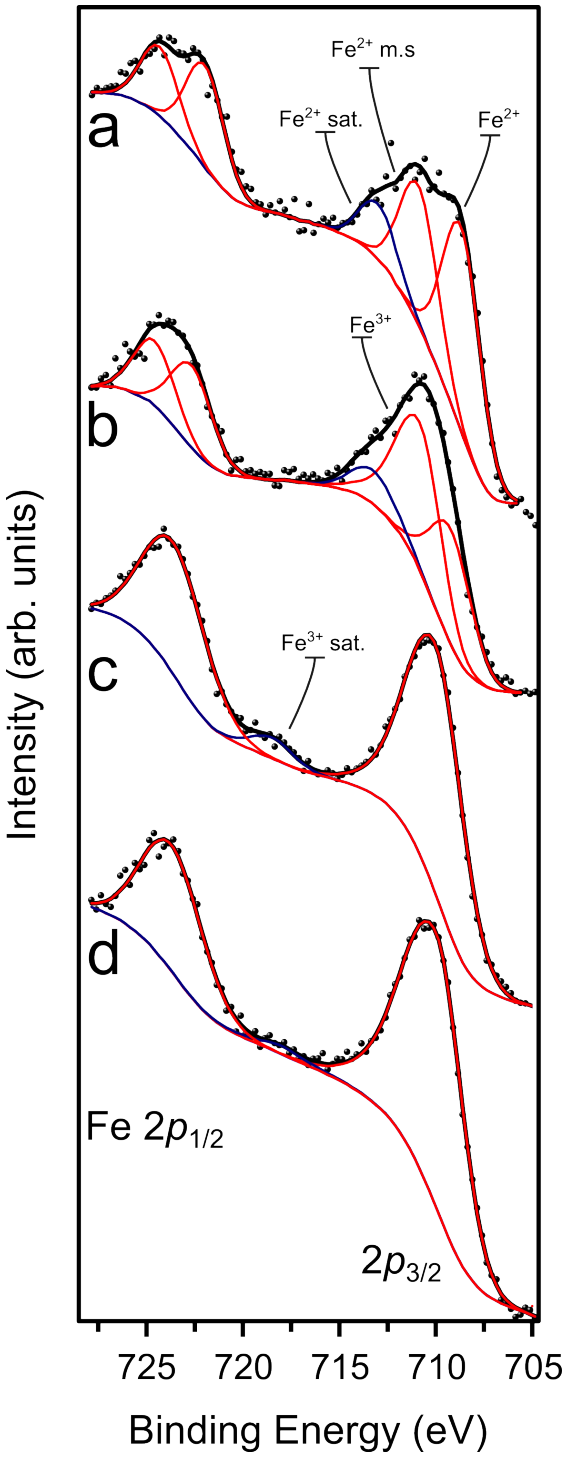

FIGURE 5.8: Fe 2*p* XPS spectra from the as-grown wetting layer (**a**), as-grown island (**b**), oxidized wetting layer (**c**) and oxidized island (**d**). The experimental spectra (black dots) have been fitted using mixed Gaussian-Lorentzian peaks (80%-20% respectively) and a combined Shirley-linear background. sat.: shake-up. m.s.: multiplet splitting.

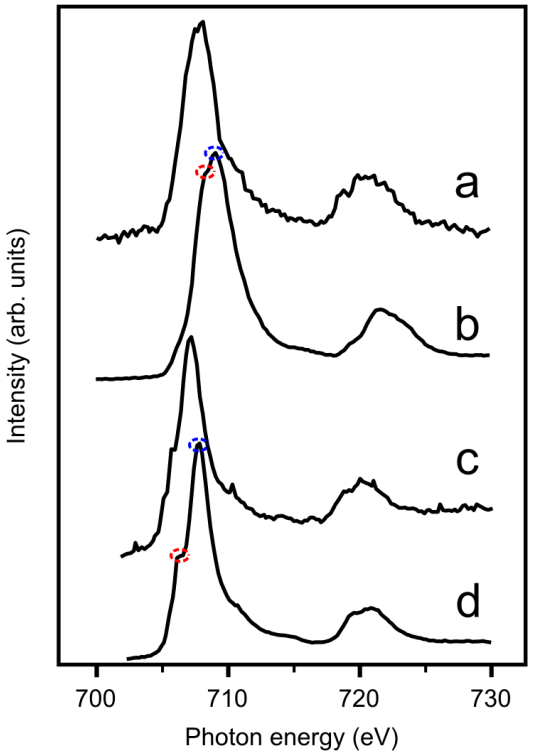

FIGURE 5.9: Fe $L_{2,3}$-edge XAS spectra. **a**. Wetting layer, as-grown. **b**. Island, as-grown. **c**. Oxidized wetting layer. **d**. Oxidized island. The red and blue circles mark the photon energies selected to obtain the XMCD images in Figure 5.11.

As describe in the introduction, both α and γ oxides accommodate Fe^{3+} cations in their structure resulting in a similar XPS Fe $2p$ spectra [26]. Although variations in the main Fe $2p_{\frac{3}{2}}$ shape originated from a change in the multiplet splitting component, or differences in the intensity of the Fe^{3+} shake-up satellite have sometimes been proposed to discriminate both phases [92], we consider the wetting layer and island spectra too similar as to give a reliable identification of one or another type of oxide.

Summarizing, the XPS data of the as-grown bi-component iron oxide confirm that the wetting layer is composed by FeO and that the triangular crystals are composed by magnetite. After the NO_2 treatment, the iron films still present two distinct components but now the wetting layer and the islands present only Fe^{3+} cations in their structure. However, an unequivocally assignment to a specific iron phase is not possible using only the XPS data. To conclude, we note that XPS nitrogen $1s$ core-level spectra were also acquired (not shown), in order to detect a possible incorporation of nitrogen into the iron oxide while using NO_2, but no N signal was detected.

Taking advantage from the synchrotron radiation, x-ray absorption spectra (XAS) can be measured to gain insight into the oxidation state and local cation arrangements in the various iron oxides. Furthermore, the iron $L_{2,3}$ edges of the iron oxide compounds

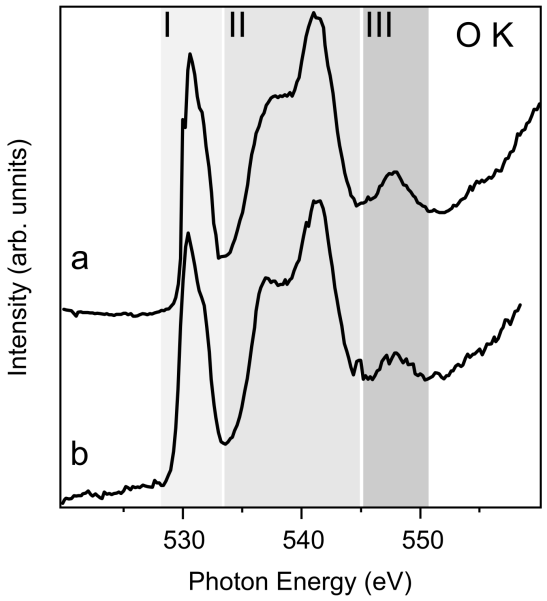

FIGURE 5.10: O K-edge absorption spectra from an as-grown (**a**) and an oxidized island (**b**), respectively. The three different features of the O K-edge spectrum have been outlined.

have been carefully investigated and can be used as fingerprint for identification purposes [274]. XAS spectra with surface sensitivity have been acquired using secondary electrons (K_E ~1.5±0.6 eV) and by integrating the PEEM image intensities inside or outside the triangular islands, before and after the oxidation process.

Figure 5.9 shows the Fe $L_{2,3}$ absorption spectra recorded from the initially-grown iron oxides: wetting layer (a) and triangular island (b).. As introduced in the previous chapter, the typical features of magnetite have been identified in the island spectrum. On the other, the absorption spectrum recorded from the wetting layer does not present this characteristic shoulder near the L_3-edge maximum and it corresponds with that reported for FeO [212]. Thus, the XAS results are, therefore, fully consistent with those obtained by XPS.

After the NO_2 oxidation, the Fe XAS $L_{2,3}$ spectra have been measured again. They present differences from those recorded before the oxidation reaction (see Figures 5.9c and d). The most distinguishing feature from the oxidized film is the pronounced shoulder of pre-L_3 edge peak at 705.8 eV, characteristic of Fe_2O_3 oxides [212]. Theoretical and experimental studies interpreted this feature as a strong contribution of Fe^{3+} cations in octahedral sites [275, 276]. It has been reported [274] that this pre-edge peak is more defined and appears more separated from the main peak of the L_3-edge in hematite than in maghemite. Although the LEED patterns suggest the formation of an hematite like oxide on the wetting layer after the NO_2 oxidation, this interpretation is not confirmed by the XAS spectrum of the wetting layer. We anticipate that this inconsistency can be

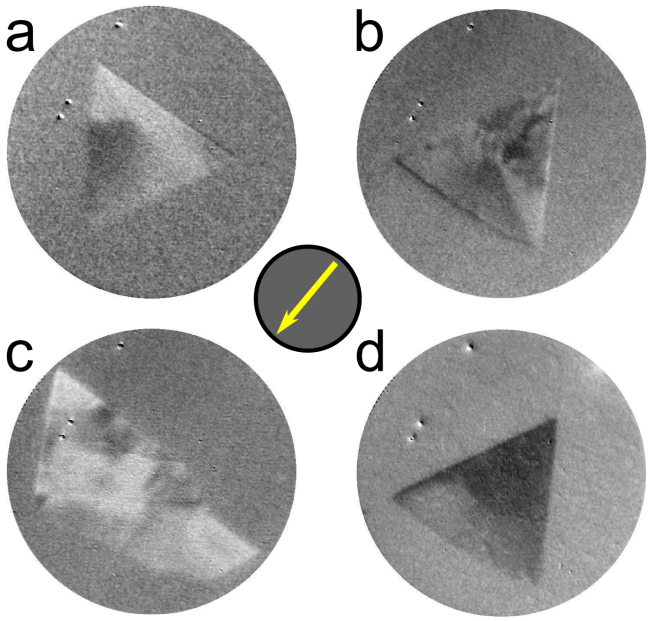

FIGURE 5.11: X-ray L_3 circular dichroism images showing a series of as-grown (**a**, **b**) and oxidized (**c**, **d**) islands. The field of view is 4 μm in both series. The photon energies are indicated in the XAS spectra in Figure 5.9. The inset in the middle indicates the experimental setting in which the photon beam (yellow arrow) direction makes an angle of 50° with the images x-axis and is oriented along the $\{01\bar{1}0\}$ substrate direction.

originated from a different depth of analysis: LEED is more surface-sensitive compared with the absorption spectroscopy. However, we will come back to discuss this point later.

Summarizing, the absorption spectra recorded from the treated surface are consistent with the XPS data in the sense that they indicate the formation of Fe^{3+} oxides both within and around the islands.

More information has been deduced from the oxygen K-edge XAS spectra recorded from the island, which are shown in Figure 5.10. Because the signal-to-noise ratio of the O K-edge spectra recorded from the wetting layer was too low, a reliable determination of its composition was hindered. This problem has been attributed to the smaller thickness of the wetting layer[3] together with the low-Z of oxygen atoms. Using the same method as for the iron edge, island spectra have been acquired before and after the NO_2 exposure. The two spectra show three different features, the first at 530 eV, the second at 535–545 eV and the third at 548 eV. The oxygen K-edge features can be compared with those reported in published works [277, 278], in which multiple scattering analysis was used to simulate the oxygen XAS spectra rendered by different iron oxides. Although at

[3]According with the previous XPS analysis described in the magnetite chapter, the wetting layer is around two FeO layer thick while the island has a thickness of (around) five FeO layers (see Chapter 4).

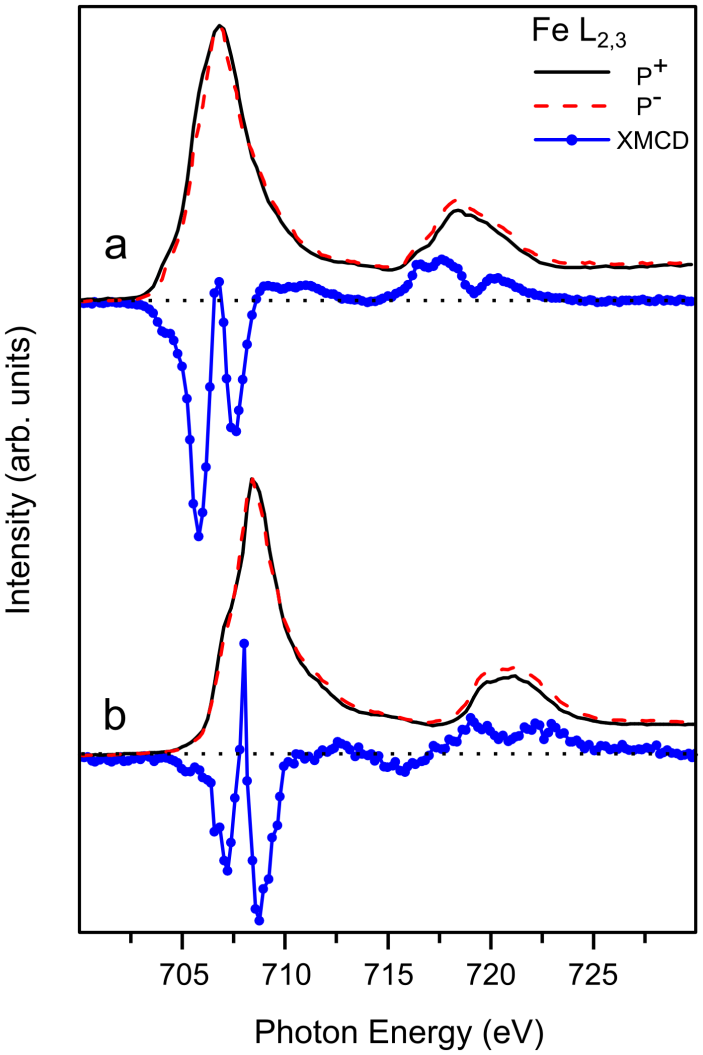

FIGURE 5.12: X-ray $L_{2,3}$ XAS with opposite (P^+, P^-) circular helicities (black and dashed red) and circular dichroism curve (blue dotted line) of an as-grown (**a**) and oxidized island (**b**). The upper XAS spectra have been adapted from the previous chapter.

first glance the spectra presented in Figure 5.10 could appear identical, a notable difference is appreciable in the shoulder found after the first peak (region (I) in Figure 5.10), being more prominent in the spectrum a than in b. This feature has been explained by transitions from oxygen antibonding $2p$ states to the empty Fe d-bands and its small variation has been interpreted in the literature as a change in the O–Fe structure [278]. Taking in account this argument, the as-grown island composition agrees with a magnetite phase while the oxidized island corresponds with the presence of a maghemite phase corroborating the previous diffraction and spectroscopic results.

Magnetic properties

As we already mentioned, iron oxides exhibit different magnetic properties (see Table 5.1): FeO and α–Fe_2O_3 are both antiferromagnetic[4] while Fe_3O_4 and γ–Fe_2O_3 have a ferrimagnetic behavior at room temperature. According with this, XMCD becomes an effective tool that helps in the identification of different iron oxide phases. Earlier we demonstrated that magnetite triangular crystals present dichroic contrast when illuminated with x-ray having different circular polarization while the FeO wetting layer does not. In a similar way, we have used XMCD-PEEM to characterize the oxidized bi-component film.

Again, we collected XAS images with opposite helicities and subtracted them pixel by pixel to provide a series of XMCD images, both from as-grown and from oxidized films. The images shown in Figure 5.11 were taken at the photon energies that correspond to the different features observed in the Fe $L_{2,3}$ spectra (red and blue circles in Figure 5.9). All the islands exhibit dichroic contrast, so they have, both before and after NO_2 exposure, an appreciable in-plane local magnetization. However, the wetting layer appears with a uniform gray intensity, both before and after oxidation, suggesting the absence of in-plane local magnetization in these regions.

The XMCD spectrum from the oxidized crystal has been measured using the same procedure described previously (see Chapter 4) and has been compared with that already presented for the as-grown film in Figure 5.12. Observing the XMCD spectrum from the as-grown island (see Figure 5.12a), we note that the well-defined peaks are usually attributed to the trivalent and divalent cations located in the octrahedral and tetrahedral sites of the magnetite structure (see Chapter 4). The XMCD spectrum of the NO_2-oxidized island is presented in Figure 5.12b. As in the case of magnetite, two negative peaks at 707.0 eV and 708.7 eV, combined with a positive peak at 707.9 eV, have been detected. The negative peak at lower energy appears less intense and shifted at higher energy when compared with its counterpart collected in the as-grown island. This change can be interpreted as the oxidation of the divalent iron cations and the the occurrence of octahedral vacancies. Thus, the XMCD spectrum collected from the oxidized crystal is consistent with maghemite [170, 276].

The XMCD results provide two important conclusions. The first one confirms the identification of maghemite in the oxidized islands. The second suggests the lack of ferri- or ferro- magnetic order in the wetting layer after NO_2-exposure. The absence of ferromagnetic order, the presence of exclusively Fe^{3+} observed in the XPS and XAS results,

[4] We remind the reader that FeO has a T_N ~200 K while hematite has a T_N ~260 K.

and the LEED pattern recorded from the region around the triangular crystals after the oxidation indicate a transformation of the as-grown FeO into an α–Fe_2O_3-like oxide.

5.3 Discussion

The as-grown films have been exhaustively discussed in the previous chapter where we have described that the wetting layer is composed by FeO while the triangular islands are composed by nanometer-thick magnetite. Now, a discussion about the effects of the NO_2 oxidation on this bi-component iron oxide film follows.

An initial NO_2 oxidation under mild condition produces an improvement in the crystallinity of the magnetite islands. By means of spot profile LEED analysis we confirm that the prepared magnetite islands exhibit a specific unreconstructed bulk termination. According with this, we speculate that a reconstruction of the magnetite surface occurs at the experimental conditions used for the oxygen-assisted MBE growth (see Chapter 4). This reconstruction, that has been also observed by STM, can be explained by the periodical arrangement of two phases ($Fe_{(1-x)}O$ and Fe_3O_4) in the magnetite topmost layer, i.e. *biphase ordering* [206, 207]. Thus, a mild NO_2 oxidation favors the transformation of the topmost layer to an unreconstructed bulk termination of the magnetite crystal.

After a prolonged NO_2 oxidation under more severe conditions the film topography is not changed in a major way, as observed by LEEM: the surface is still characterized by a continuous wetting layer and large, mostly triangular, flat islands. But the composition of the wetting layer and the regular crystals has been transformed markedly.

In the islands, the (2×2) LEED pattern is maintained, although with a smaller lattice spacing than before, 2.9 Å, and with a small rotation of 3°. On the other hand, the Fe 2*p* XPS signal changes, showing features characteristic of trivalent iron cations. This suggests that, upon oxidation, maghemite could be transformed to any of the Fe_2O_3 phases. Because the LEED pattern still exhibits a 2×2 spot arrangement, we discard an hematite phase that would give a $\sqrt{3}\times\sqrt{3}R30°$ LEED pattern [when it exposes its (0001) surface]. This description is further confirmed by the Fe and O XAS spectra, which are typical of maghemite and substantially different from that of magnetite. Finally, the islands still show XMCD contrast, indicating that these crystals present ferrimagnetic order. Since maghemite is the only binary ferrimagnetic iron oxide with Fe^{3+} cations, the islands obtained by a prolonged oxidation of magnetite at 600 K are unequivocally identified as γ–$Fe_2O_3(001)$.

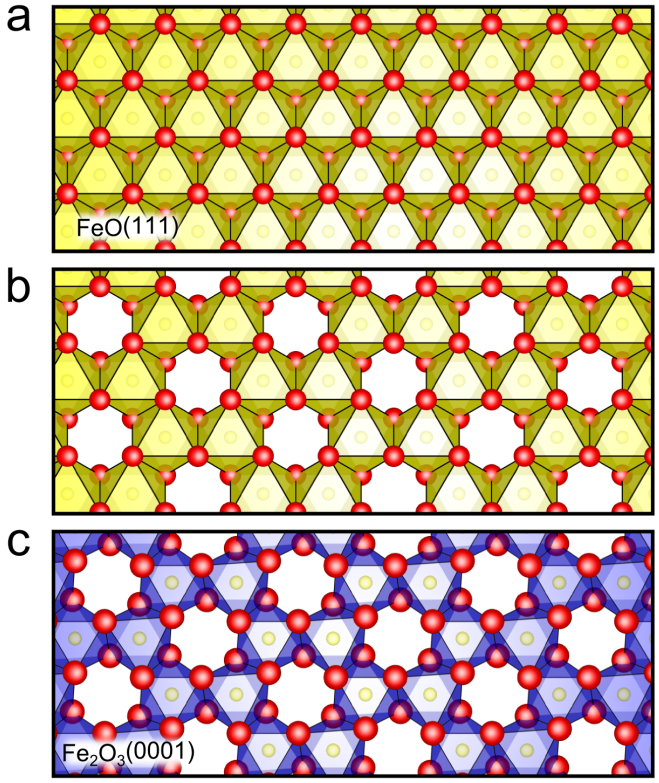

FIGURE 5.13: Schematic of the FeO(111)-to-Fe_2O_3(0001) oxidation mechanism. Two FeO(111) layers (**a**). In Figure **b**, $\frac{1}{3}$ iron atoms have been removed forming a $\sqrt{3} \times \sqrt{3}R30°$ pattern that is comparable with an hematite layer. An α–Fe_2O_3(0001) thin film can be achieved by relaxing the previous structure. The red spheres correspond to oxygen atoms, while the iron atoms in octahedral sites are labeled by yellow spheres.

Also analyzing the wetting layer, a modification has been registered after the NO_2 oxidation. The diffraction measurements indicate a reduction in the lattice spacing, 3.0 Å, and a new $\sqrt{3} \times \sqrt{3}R30°$ structure (see Figure 5.5e) is observed. As shown in the introduction section when the hematite surface has been discussed, this pattern is in agreement with that of an unreconstructed α–Fe_2O_3(0001) surface. This determination is further supported by XPS analysis, that shows a spectrum containing the typical features of a Fe^{3+} oxide. Because no XMCD signal has been detected, an antiferromagnetic or paramagnetic behavior has to be assumed. The absorption spectrum is more ambiguous as it shows some features that can be interpreted as trivalent iron oxide, but does not correspond clearly to hematite. In fact, hematite exhibits a particular peak before the absorption edge in its characteristic XAS spectrum which is not clearly observed here. This result can be explained assuming that XAS and XPS have different surface sensitivity due to the different energies of the collected electrons. Then, the difference between the XPS and XAS spectra would point to an incomplete oxidation of the full film thickness with the surface being completely converted to an hematite-like film while the film close to the Ru interface would still be composed by FeO.

The oxidation of the original bi-component oxide (FeO/Fe_3O_4) produces a transformation into two different alotropes of Fe_2O_3 (α/γ). The reason for the different oxidation pathway most probably can be attributed to the low temperature employed during the treatment. Considering the crystallographic properties of each phase, FeO, magnetite and maghemite are based on an fcc anion lattice while hematite is hcp. Also, while magnetite and maghemite are characterized by two different cation positions (octahedrally and tetrahedrally coordinated), in FeO and hematite the cations occupy only octahedral positions.

Thus, the transformation of magnetite to maghemite is topotactic: the atom arrangement remains unchanged and only some cations in octahedral position migrate to the surface where they react with oxygen. According with this argument, cation diffusion is supposed to be the main mechanism in the oxidation reaction in the bulk specimen [266, 268]. In contrast, the transformation of magnetite or maghemite into hematite requires i) a change in the oxygen lattice from fcc to hcp, ii) the removal of tetrahedral cations from the lattice. All together, it is clear that under our experimental condition the magnetite-to-hematite transformation, although could be thermodynamically favourable, is kinetically hindered.

However, the wetting layer evolves from an FeO structure to an hematite-like film. The mechanism of this oxidation reaction can be explained invoking the same arguments used for the magnetite-to-maghemite transformation. Both FeO(111) and α–Fe_2O_3(0001) have only octahedrally coordinated cations. Although the anion lattices are not equivalent, the difference requires at least three oxygen-iron layers (i.e. considering two layers, the sequence in an fcc or hcp lattice is equivalent). As the wetting layer is composed by around two layers, this limitation does not apply. Starting with FeO, the divalent cations occupy all the octahedral positions within the oxygen lattice (see Figure 5.13a). If $\frac{1}{3}$ of these cations migrate to the film's surface to react with further oxygen (provided by the NO_2 dissociation), the FeO structure evolves (Figure 5.13b) to that of hematite (Figure 5.13c), again topotactically. The same mechanism, diffusion of the iron cations, could be on the basis of the transformation of the magnetite to maghemite and the transformation of the ultrathin films of FeO to hematite. These results contribute to clarify old controversies [266, 267, 269, 270, 279] of the kinetic barriers associated with the magnetite-to-maghemite transformation, in which it was suggested [279] and then discussed [267] that magnemite evolves to maghemite only in the absence of hematite seed nanocrystals. With these crystals, the magnetite oxidation produces hematite instead of maghemite. In our case, despite the presence of an hematite wetting layer, the magnetite islands evolve only to maghemite.

5.4 Conclusion

In this chapter, the oxidation of a bi-component iron oxide surface has been described by means of diffraction, spectroscopy and microscopy methods. The initial film composed by FeO and large magnetite crystals evolves, upon NO_2 exposure, to hematite and maghemite, respectively. Both the wetting layer and island transformation have been interpreted by the diffusion of octahedrally coordinated iron cations to the surface. At the surface, they react with the atomic oxygen provided by the dissociation of NO_2. In both cases, these transformations are topotactic.

Our study indicates the possibility of obtaining different bi-component iron oxides in ultrathin film form in the same substrate by means of a choice of adequate experimental conditions. This behavior allows tailoring the characteristics of an ultrathin film exploiting their catalytic or magnetic properties.

Chapter 6

Integral Low-energy Electron Mössbauer Spectroscopy

6.1 Introduction

Mössbauer spectroscopy is a well-established tool which can provide essential information in many areas of science [9]. Taking advantage of the Mössbauer effect, this technique can be used for the investigation of the chemical, physical or magnetic properties of a material.

The Mössbauer Effect

A radioactive nucleus in an excited state undergoes a variety of level transitions resulting in the emission of radiation, for example, gamma radiation. During this decay process, a gamma ray can be resonantly absorbed by other stable nucleus of the same isotope. Because the nuclear recoil occurs both in the emission and absorption events, this resonance process was initially not observed. Only in 1957 Rudolf L. Mössbauer[1] discovered that the recoil process could be hindered by the incorporation of the radioactive nuclei in a solid matrix, favoring the emission without energy loss. The Mössbauer effect is restricted to a limited series of isotopes characterized by a low-lying excited states because the probability of such a recoil-less event depends, apart from some characteristics of the solid, on the energy of the emitted γ-ray [281]. Although it has been observed in over a hundred isotopes, the application of the Mössbauer effect as Mössbauer spectroscopy allows favorable experimental conditions only with a smaller number of them.

[1] Rudolf L. Mössbauer was awarded the 1961 Nobel Prize in Physics, *"for his researches concerning the resonance absorption of gamma radiation and his discovery in this connection of the effect which bears his name"* [280].

Since the ^{57}Fe isotope exhibits the most advantageous combination of properties for the Mössbauer spectroscopy, this technique has mainly been applied to the investigation of iron-containing materials.

Mössbauer Spectroscopy

The experimental setup for Mössbauer spectroscopy consists of a radioactive source with the Mössbauer isotope in an excited state and an absorber (the analyzed material) which incorporates this same isotope in its ground state. The source suitable for ^{57}Fe Mössbauer spectroscopy is ^{57}Co. This nuclide undergoes a spontaneous electron capture transition into a metastable state of ^{57}Fe which in turn decays to its ground state by emission of γ radiation. In order to prevent recoil effects, the radioactive source is embedded in a specific support providing the required solid environment.

In a typical transmission experiment, the radiation emitted by the ^{57}Co source illuminates the specimen, where it may be partially absorbed, and reaches a detector. Because the energy levels of the atoms situated in the sample are modified by the environment, an energy scanning is necessary in such a way that the emission energy becomes appropriate for the occurrence of a resonance absorption event.

This is usually achieved by a transducer that moves the radioactive source relative to a stationary absorber and hence gives an energy shift as a result of the Doppler effect. Thus, the energy scan is provided by the oscillatory motion of the source. Since a resonant absorption event occurs when the energy of the gamma radiation matches the nuclear transition energy for the sample isotope nucleus, a typical Mössbauer spectrum consists of a plot of the relative absorption versus the velocity of the source with respect to the specimen. The energy axis is usually expressed in millimeters per second. If both source and sample accommodate the same Mössbauer isotope in the same environment, the resulting spectrum consists of a single absorption line located at zero velocity.

The Mössbauer spectrum is characterized by the number, shape, position and relative intensity of the various absorption peaks. These features are strictly associated to the nature of the interactions of the nucleus with the surrounding atomic environment (*hyperfine interactions*). The shift of the Mössbauer spectrum as a whole is known as *isomer shift* and it is due to the electric interaction between the nuclear charge distribution and the electronic charge density which can exist within the nuclear volume (mostly due to s electrons). In a system where this electric monopole interaction is the only factor affecting the nuclear energy levels, the nuclear ground and excited states are unsplit, but their energy separation is different in the source and absorber by a specific value, the isomer shift δ. Figure 6.1a schematically describes this scenario, where the

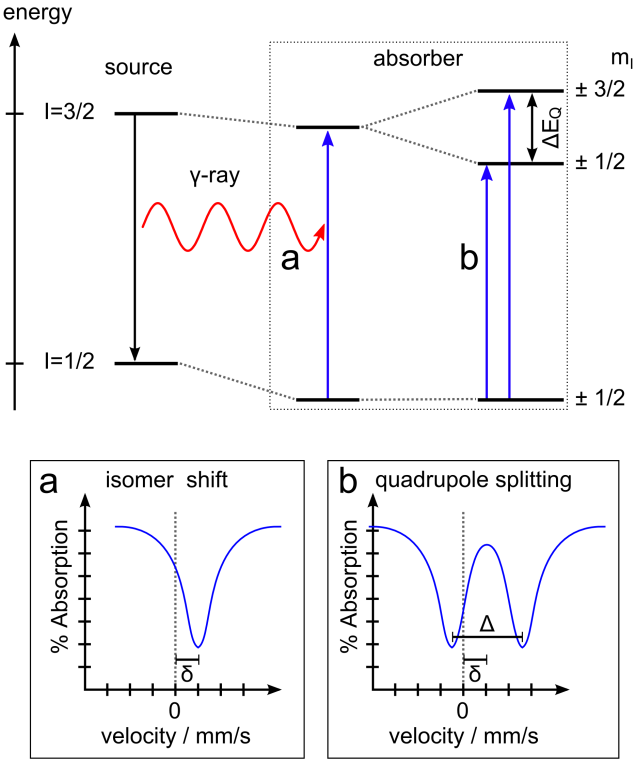

FIGURE 6.1: Schematic of the effect on the nuclear energy level of ^{57}Fe of the isomer shift (**a**) and the quadrupole splitting (**b**). The Mössbauer absorption event and the resulting spectra, which results in the isomer shift δ and the quadrupole splitting Δ, are shown.

transition energy between the ground and excited states is modified (with respect to the source) in the absorber by differences in the electronic environment of the sample nucleus. The resulting spectrum (see Figure 6.1a) consists of a single line shifted from the zero velocity line by δ. Because the electronic densities within the nuclear volume are affected by the electronic configuration of the atoms analyzed, the isomer shift δ becomes fundamental in the determination of atomic oxidation states.

When the nucleus exhibits an angular momentum quantum number $I > \frac{1}{2}$, its charge distribution is non-spherical and a nuclear quadrupole moment exists. If the nuclear quadrupole moment interacts with an asymmetric electric field produced by an inhomogeneous electronic charge distribution, an *electronic quadrupole interaction* occurs. As a result of this process, the nuclear energy levels are splitted as a function of I, corresponding to different alignments of the quadrupole moment with respect to the electric field. Considering that the ^{57}Fe has an excited state with $I{=}\frac{3}{2}$, in the presence of an asymmetric charge distribution it splits into two substates characterized by $m_I{=}\pm\frac{1}{2}$ and $m_I{=}\pm\frac{3}{2}$ as depicted in Figure 6.1b. This situation is reflected in the Mössbauer spectrum by the appearance of two lines separated by the *quadrupole splitting*, Δ (see Figure 6.1b). Because the quadrupole splitting results from the interaction of the nuclear quadrupole

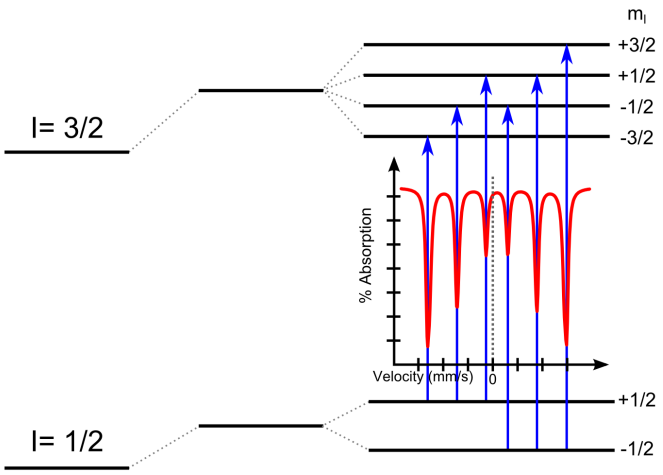

FIGURE 6.2: The effect of magnetic splitting on the energy levels of the ^{57}Fe nuclei. The Mössbauer absorption transitions are depicted with blue lines while the resulting Mössbauer spectrum characterized by absorption peaks is represented with a red line. The image has been adapted from ref. [9].

moment and an inhomogeneous charge distribution around the atom, this parameter gives information about ligand structure, coordination type or the defect structure of solids.

In a magnetic field, a magnetic dipole interaction occurs between the nuclear magnetic moment and the magnetic field. This removes the degeneracy of the nuclear states into $2I+1$ sublevels (for I>0). In ^{57}Fe, its ground state has $I=\frac{1}{2}$ that splits into two sublevels, while its excited state with $I=\frac{3}{2}$ splits into four sublevels, as schematically represented in Figure 6.2. According to the selection rules applicable to this system, $\Delta m_I=0,\pm1$, six possible transitions are possible when a γ-ray is absorbed, producing six absorption lines (see the inset in Figure 6.2) in the Mössbauer spectrum (*Magnetic Splitting*). The total magnetic field at the nucleus is the vector sum of the magnetic internal magnetic field and any applied magnetic field. Since the internal magnetic field arises from any unpaired spin of the electrons in the atom, it is affected by the oxidation or spin state of the atom itself. Moreover, only the unpaired electrons can contribute either directly or indirectly to the magnetic field. This hyperfine interaction is characteristic of magnetically ordered systems, or of paramagnetic systems when the electron spin relaxation times are relative long. The information obtained from the *magnetic splitting*, the so called *hyperfine field* can be used to investigate the magnetic order and structure of magnetically ordered systems, the nature of magnetic interactions, the magnetic moment of specific atoms, and to elucidate the electronic structure of atoms.

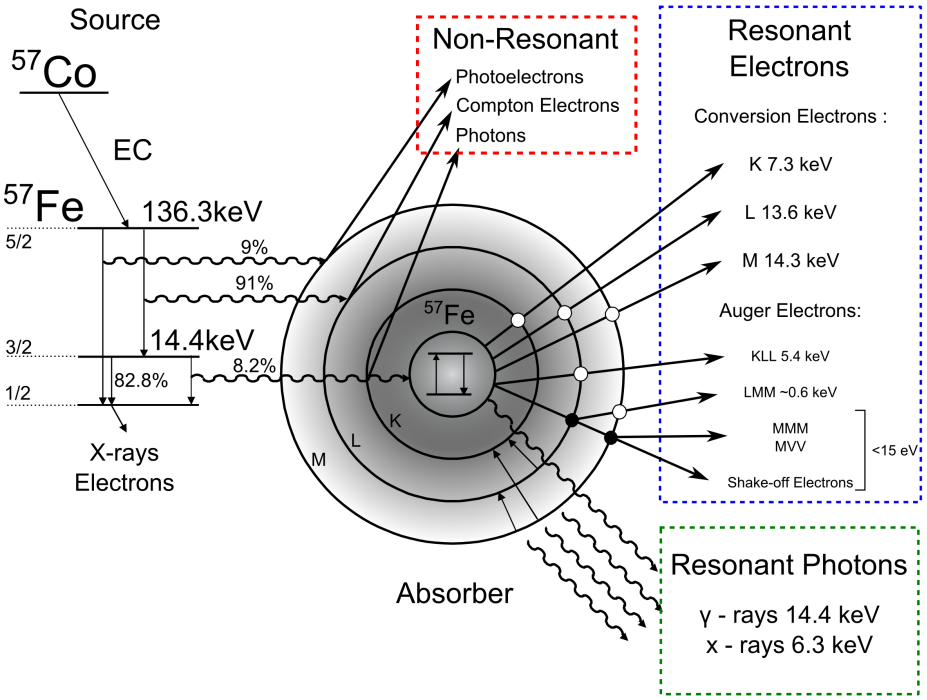

FIGURE 6.3: Schematic diagram showing the processes occurring at the ^{57}Fe atom consequentially to the nuclear resonant absorption of a γ-ray. The series of resonant and non-resonant photon and electron emissions combined with their energies have been listed. Adapted from Ref. [10].

6.2 Mössbauer Spectroscopy and Surface Science

Although Mössbauer Spectroscopy is usually considered a bulk-sensitive method, it has been also applied to the investigation of surfaces in the last decades [10, 11, 282–284]. In order to explain how Mössbauer spectroscopy can become a surface-sensitive technique, we start by describing the effects of the γ-ray absorption on the ^{57}Fe atoms.

Following the resonant absorption, the nuclear decay from an excited state to a ground state proceeds by two competitive processes: gamma emission or internal conversion [11]. The former has already been described. In the latter, the nucleus transfers its excess energy to an electron which is ejected from the atomic shell. Since internal conversion can eject electrons of different atomic levels, they are named indicating the shell where they come from (i.e. K, L, M - conversion electrons). Considering the 14.4 keV transition of ^{57}Fe, the probabilities of internal conversion by ejecting a K, L, or M electrons are 81, 9, and 1%, respectively while the probability of de-excitation through reemission of gamma radiation is 9%.

After the ejection of an electron, a hole in the atomic shell is generated which can be filled by another electron. This internal recombination produces a subsequent Auger electron or x-ray emission [27]. Other events also occur during the ejection of an electron

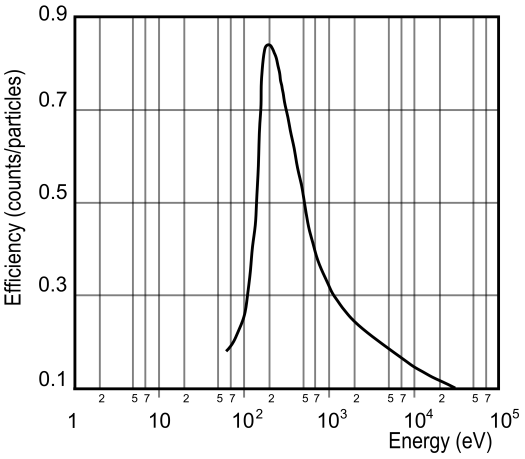

FIGURE 6.4: Typical curve of the dependence of channeltron detection efficiency with electron energy. From ref. [11].

from an inner shell. So, part of its energy can be transferred to another electron located in an outer shell favoring its expulsion. This mechanism is known as *shake-off* [27]. These electrons, that usually exhibit a small energy, represent a significant fraction of the whole electron emission (>50%). The processes following the nuclear resonant absorption, namely nuclear de-excitation and atomic relaxation, have been summarized in Figure 6.3.

The detection of the whole or a portion of the electron emission generated after the Mössbauer event gives place to electron Mössbauer spectroscopies. Because a large amount of resonant electrons is ejected from different depths in the solid (depending on the electron energies), these techniques are considered surface-sensitive.

The most established application is Integral Conversion Electron Mössbauer Spectroscopy (ICEMS), consisting in the collection of all the electrons ejected from the sample surface after its illumination with γ radiation regardless of their energy [11, 285]. Commonly the detection of the electron emission is carried out using gas-flow proportional counters or avalanche counters which are not UHV compatible. Moreover, there is risk of arcs between the sample and the detector damaging the sample. Although it has demonstrated that ICEMS provides information up to a depth of ∼330 nm, its surface sensitivity is not comparable with other surface sensitive spectroscopies (XPS, AES) in which the detection analysis is limited to ∼1 nm [27].

In this chapter we started by introducing the basic concepts of the Mössbauer spectroscopy and its capabilities for the understanding of many chemical and physical questions related with Fe-containing materials. In the following sections, the challenging

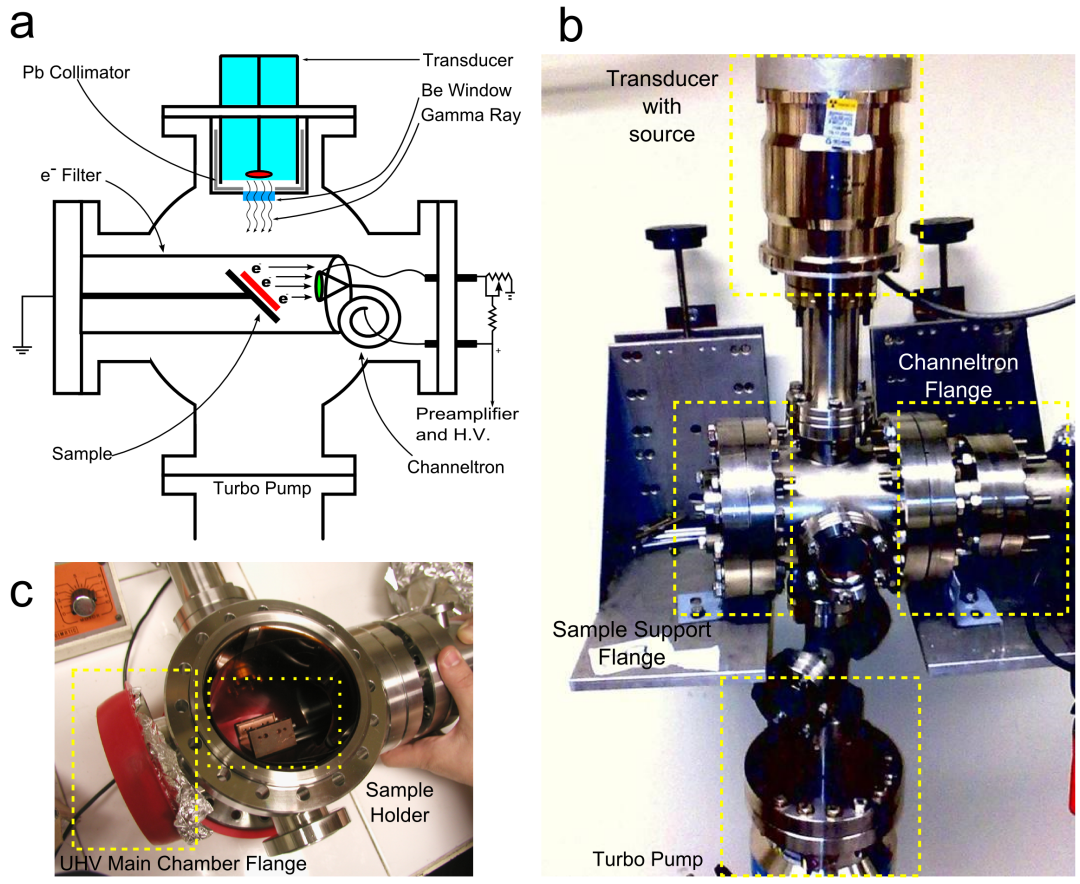

FIGURE 6.5: **a**. Schematics of an ILEEMS spectrometer. **b**. Image of the first setup of the ILEEMS spectrometer developed for the optimization procedures. **c**. Image of the definitive chamber before the coupling of the ILEEMS to the "Surfmoss" UHV main chamber.

implementation of a less known tool that permits an enhancement of the surface sensitivity of electron Mössbauer spectroscopy will be described and discussed.

6.3 Integral Low-Energy Electron Mössbauer Spectroscopy (ILEEMS)

Integral low-energy Mössbauer spectroscopy, which was proposed in the past [286, 287], and recently rediscovered [10], is a variant of electron Mössbauer spectroscopy that allows an enhancement of the surface-sensitivity.

As we described in the previous section, the de-excitation of a resonantly excited ^{57}Fe nucleus is followed by the ejection of electrons. Part of this electron emission is characterized by electrons with very-low energies (<15 eV) and can be more than 50% of the total resonant signal. It has theoretically and experimentally demonstrated that each

Mössbauer event generates an average of about 6.5 ejected electrons, of which ∼1.5 have high energy (>5 keV) and ∼5.0 are low-energy Auger (<100 eV) and shake-off (<15 eV) electrons. Several experimental results [286, 287] also established that this low-energy emission is originated from the topmost ∼5 nm of the sample providing surface-sensitive information. Thus, the detection of these electrons becomes, in principle, a suitable way to perform surface analysis with sensibilities comparable to those of AES or XPS.

From the experimental point of view, there are several methods to collect this low-energy electron emission. Although initial attempts employed an electrostatic energy analyzer to select electrons of the desired energy, this tool was latter discarded because it exhibited several experimental disadvantages (low counting rates, and long acquisition times) [11]. A more simple approach is the use of a channeltron electron multiplier as electron collector (that is also UHV compatible). By applying a positive bias between the sample and the cone entrance of the channeltron, the detection efficiency can be tuned and can be enhanced for those electrons with energies in the range of a few hundred eV. In fact, a positive bias modifies the energy of the resonant electrons in such a way that it can match the maximum of the channeltron detection efficiency (see Figure 6.4).

An ILEEMS spectrometer based on this method has been recently described [10]. The setup consists of an aluminum chamber, in which sample and channeltron are housed and maintained in high vacuum condition (∼10^{-5} Torr range) by a turbomolecular pump. In our design, to meet UHV conditions, a stainless steel chamber provided with several conflat-type flanges have been used for the housing of our ILEEMS spectrometer. An elementary sketch of the spectrometer arrangement is depicted in Figure 6.5a while Figure 6.5b shows the ILEEMS prototype built in our laboratory for testing. The definitive version of the ILEEMS chamber which has been coupled to the "Surfmoss" system, is shown in Figure 6.5c. Since the ILEEMS chamber communicates with the "Surfmoss" chamber by a gate valve, the latter setup permits the analysis of samples prepared both *ex situ* and *in situ* (usually prepared by MBE/O-MBE).

The main problem involved with the use of stainless steel is the unwanted contribution of the electrons coming from the inner walls of the chamber to the Mössbauer spectrum. This inconvenience becomes crucial when a positive bias is applied at the cone entrance of the channeltron. Because the sample and the chamber are grounded, the applied voltage favors the acceleration toward the channeltron of those electrons ejected both from the sample and from the chamber walls. In Figure 6.6 we present a series of ILEEMS spectra acquired from a 5 nm-thick ^{57}Fe thin film characterized by an oxidized topmost layer. Figure 6.6a shows a spectrum collected from this sample. It exhibits different contributions: a sextet relative to the α-Fe substrate and a doublet that arises from the Fe^{3+} contained in the external oxidized layer. When a +200 V voltage is

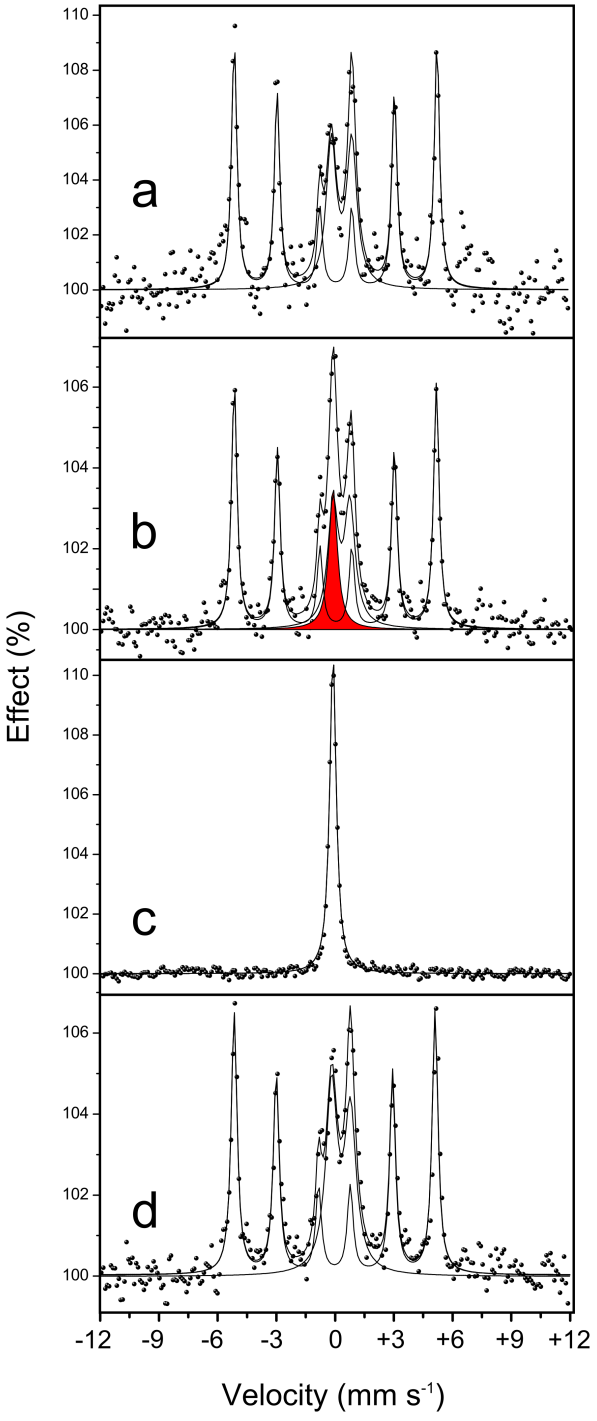

FIGURE 6.6: Mössbauer spectra from a 5 nm thick sample of ^{57}Fe oxidized at the surface. While the spectrum (**a**) has been recorded without bias, the spectrum in (**b**) has been collected with a bias of +200 V applied to the channeltron. The signal (single peak outlined in red) coming from the stainless steel of the chamber walls is clearly appreciable. **c**. ILEEMS spectrum recorded with the sample removed and at the same +200 V bias voltage. The typical Mössbauer spectrum of stainless steel is obtained. **d**. ILEEMS spectrum collected from the same iron oxide sample with a bias of +200 V after the application of an electron filter.

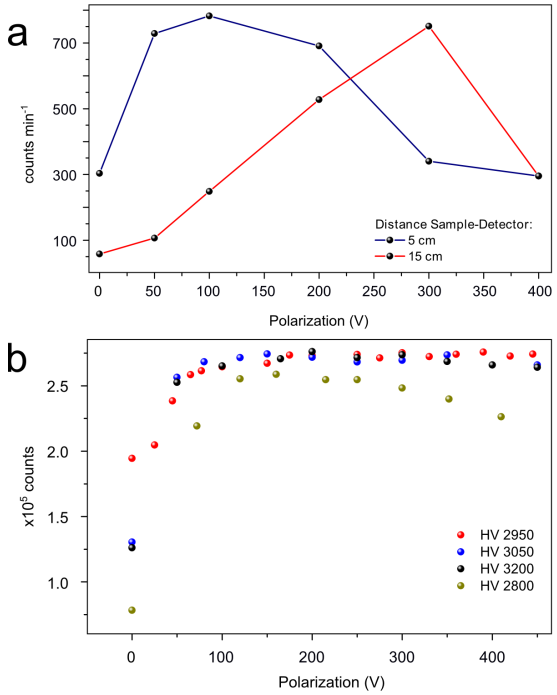

FIGURE 6.7: **a**. Dependence of the number of counts per second recorded in the channeltron of the ILEEMS prototype of Figure 6.5b, with applied bias voltage and different sample-to-detector distances. **b**. Dependence of the number of counts with the applied bias voltage and different operating channeltron voltages. The latter experiment has been carried out using the definitive setup of Figure 6.5c.

applied between the sample and the channeltron, a third component, interpreted as the stainless steel contribution produced by the chamber walls, appears (red peak in Figure 6.6b). More interestingly, even in absence of a sample, a spectrum composed of only a singlet is observed (see Figure 6.6c). This parasitic contribution can be eliminated by the application of a "physical electron filter": a simple Kapton sheet made conductive by a graphite coating. While in the initial setup (Figure 6.5a and b) the filter covers both the sample and the detector, in the other ILEEMS system (see Figure 6.5c) it was positioned directly upon the chamber walls. The filtering effect is demonstrated by the spectrum shown in Figure 6.6d in which the contribution of the stainless steel is absent.

The magnitude of the polarization voltage between the sample and the channeltron remains an important parameter that needs to be adjusted and optimized. Depending of the channeltron type and the distance between the sample and the detector, the polarization voltage can strongly affect the number of electrons that reach the detector. Figure 6.7a shows the behavior of the number of counts obtained varying the bias voltage and the sample-to-detector distance. The dependence of the number of counts with the polarization bias at different electric potentials (applied between the cone and the end of the channeltron) has been depicted in Figure 6.7b. These studies permit an improvement of the counting conditions that were utilized for obtaining the ILEEMS spectra.

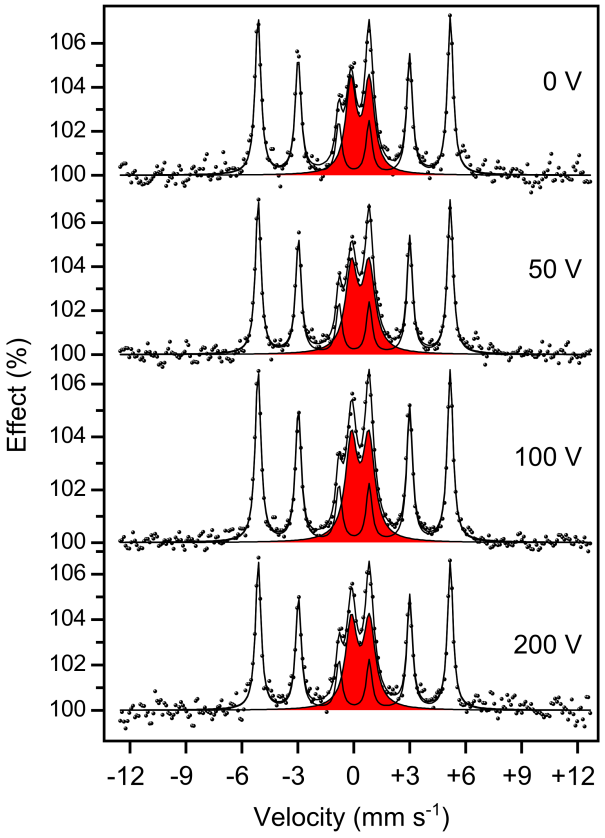

FIGURE 6.8: Series of ILEEMS spectra collected at different voltage polarization from a 5 nm thick ^{57}Fe film that exhibits an oxidized topmost layer.

Examples of several spectra recorded applying different polarization voltages are in Figure 6.8. The fitting of the spectra reveals that differences in the signal associated with the oxidized layer are not very appreciable. In fact, only a small increase (∼4%) of the doublet (red doublet in Figure 6.8) is observed for a polarization voltage of +100 V[2]. Since for the sample, the oxide should only be present at the surface of the film, an enhancement of the doublet would be expected by applying a bias voltage if the surface sensitivity is increased. That this is not the case might be interpreted by invoking (i) the nature of the sample (which probably has a rough surface), and (ii) the occurrence of multiple scattering events well inside the sample that can originate spurious resonant and non-resonant emission indistinguishable from the primary signal coming from the surface.

We compare data obtained from transmission experiments, ICEMS experiments[3], and ILEEMS experiments using the prototype described in Figure 6.5b. The spectra shown in Figure 6.9a have been recorded from acicular γ-Fe_2O_3 nanoparticles of about 400 nm

[2]This voltage corresponds to the maximum in number of counts in Figure 6.7a (blue line).

[3]The ICEMS technique has been carried out using a parallel-plate avalanche counter described in ref. [288].

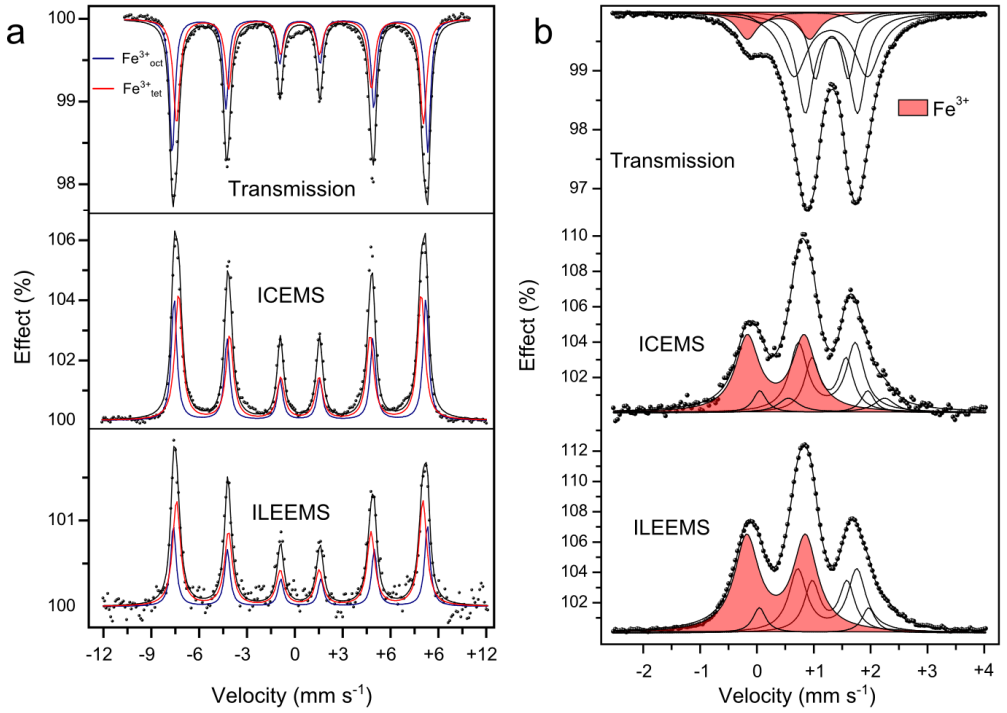

FIGURE 6.9: Transmission, ICEMS and ILEEMS spectra recorded from a sample of acicular γ-Fe_2O_3 nanoparticles (**a**) and a sample of $Fe_{0.33}NbTiP_3O_{12}$ (20% enriched with ^{5}7Fe) (**b**).

in length and 100 nm in width. The spectra have been fitted using two sextets corresponding to trivalent iron cations that occupy octahedral (blue lines) and tetrahedral (red lines) sites of the γ-Fe_2O_3 spinel structure. The intensity ratio ($\frac{tet}{oct}$) between the two components is 1.0 for the spectrum collected using transmission method, 1.4 for ICEMS and 1.9 for ILEEMS, respectively. Taking in account the shape of the particle, this result is expected because the particle surface exhibits a larger number of sites with reduced coordination. Even more, we demonstrate that ILEEMS has an increased surface sensitivity with respect to that shown by ICEMS.

Figure 6.9b shows another illustrative example. The same series of spectra have been collected from a sample of $Fe_{0.33}NbTiP_3O_{12}$. This compound is characterized by the presence of divalent iron cation occupying octahedral sites within its Nasicon-related structure [289]. In all the spectra an additional Fe^{3+} signal is appreciable and its value is 10% in the transmission spectrum while it is 40% in the ICEMS spectrum. This clearly suggests that the ferric contribution is a surface component rising from the oxidation of some surface Fe^{2+} cations. This component is more pronounced in the ILEEMS spectrum, accounting for 48% of the total spectral area (a 20% increase with respect to the ICEMS spectrum).

We note that although recent ILEEMS results revealed some differences between the surface and the bulk composition of some samples [10], unfortunately, they have not

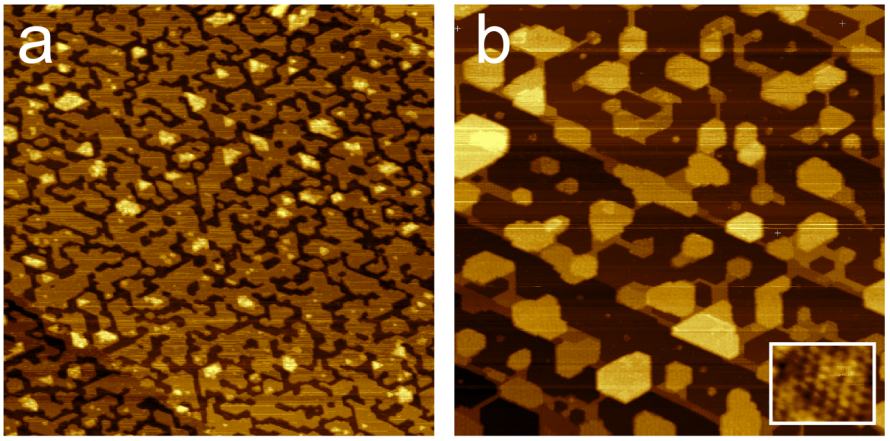

FIGURE 6.10: STM measurements on ^{57}Fe-containing iron oxide films. **a**. 300×300 nm^2 STM image showing the Ru(0001) surface covered with small $^{57}Fe_3O_4$(111) islands nucleated on 2 ML of ^{57}FeO(111). The image has been collected at I_t=0.9 nA and U_b=+2.0 V. **b**. 250×250 nm^2 STM image showing bigger magnetite islands nucleated on FeO(111). In the inset a detail of the atomic protrusions relative to the magnetite surface has been depicted. The atomic resolution reveals a surface unit cell of 6.0 Å (I_t=2.0 nA and U_b=+1.14 V.).

been compared with ICEMS data recorded using conventional electron counters. Thus, a reliable comparison of the surface sensitivity of ILEEMS with respect to the most common ICEMS technique has not been presented. Nevertheless, our experiments suggest an improved surface sensitivity of the ILEEMS with respect to that of ICEMS. However, it seems that the ILEEMS depth range of analysis is not comparable with that of surface science techniques (XPS, AES), as it has been proposed by de Grave and co workers [10, 284].

6.4 ILEEMS analysis on iron oxide ultrathin films

In this section we present the first results of the application of ILEEMS to the study of iron oxide ultrathin films. As we described before, the fundamental problem regarding ILEEMS is the discrimination between the primary resonant low-energy electron generated in the topmost region from those secondary electrons generated deep in the bulk. This is not a problem when a very thin layer of iron compound has been grown on an inert (i.e., not Mössbauer active) substrate.

Because the nuclear resonance absorption only occurs in ^{57}Fe[4], the preparation of ^{57}Fe-enriched ultrathin films is preferred in order to obtain a measurable Mössbauer signal. Thus, the growth of iron oxide films on Ru(0001) has been carried out using an home-made ^{57}Fe evaporator based on electron bombardment. The ^{57}Fe doser has been coupled

[4]The isotopic abundance of ^{57}Fe is 2% [281].

to the "Surfmoss" preparation chamber and calibrated by STM analysis. Applying the experimental conditions described in the previous chapters we were able to prepare ultrathin films of different iron oxides by depositing metallic iron layers followed by an oxidation process in oxygen atmosphere. Some examples of the obtained ultrathin films have been reported in Figure 6.10 that shows the Ru(0001) substrate covered with a bi-component film. Taking in account the previous studies about the iron oxide growth mechanism, we interpret the film as composed of nanometer-thick magnetite islands nucleated on top of two layers of ^{57}FeO(111). This interpretation is confirmed by measuring the distances between protrusions in the atomically resolved STM images (see the inset in Figure 6.10b). The thicker islands exhibit a surface unit cell of 6.0 Å corresponding to the lattice constant of the hexagonal unit cell of magnetite (111) surface [13, 75].

Figure 6.11c shows an ILEEMS spectrum recorded from an ^{57}Fe oxide ultrathin film comparable with those imaged by STM in Figure 6.10. Previously to the ILEEMS measurement the sample has been analyzed by LEED and XPS. Although in the observed LEED pattern the spots are blurry and do not allow to distinguish precisely the nature of the iron oxide[5], the Fe 2*p* XPS spectrum confirms the presence of Fe^{2+} and Fe^{3+} compatible with the presence of a mixture of magnetite and FeO.

Regarding the ILEEMS spectrum, the experimental data (dots in Figure 6.11) have been fitted using several components (summarized in Table 6.1). The first series of contributions include two doublets (red and blue peaks in Figure 6.11c) which can be attributed to a FeO-like phase that is paramagnetic at room temperature (FeO becomes antiferromagnetic below $T_N \approx 200$ K). Although the FeO contributions have been fitted using two different quadrupole-split doublets, the poor signal-to-noise ratio introduces a large uncertainty in the values obtained for δ and Δ [259, 264]. The second series of contributions consists of two sextets characteristic of a ferrimagnetic magnetite phase. These components have been assigned to the different coordination of the iron cations in the magnetite spinel structure. Because the electron *hopping* process is much faster than the de-excitation processes experimented by the ^{57}Fe nucleus, the octahedral site ions contribute with one average "$Fe^{2.5+}$"-like component to the Mössbauer spectrum. The second sextet is originated by the Fe^{3+} tetrahedrally coordinated. In a typical magnetite Mössbauer spectrum the intensity ratio between these two sextets becomes a very sensible measurement of the oxide stoichiometry (stoichiometric Fe_3O_4 gives I_{tet}/I_{oct}=0.5). As we already note, the lacking of good statistics precludes a precise quantification of the stoichiometry of the film. In fact, during the ILEEMS analysis, that runs for about one month, we observed a very low counting rate probably due to complications in the experimental design: because the Ru(0001) substrate has a diameter of only 9 mm and

[5]The unit cell measured using the blurry spots in Figure 6.11a is 3.2Å. This value is in agreement with those of FeO and the oxygen lattice in magnetite previously grown on Ru(0001).

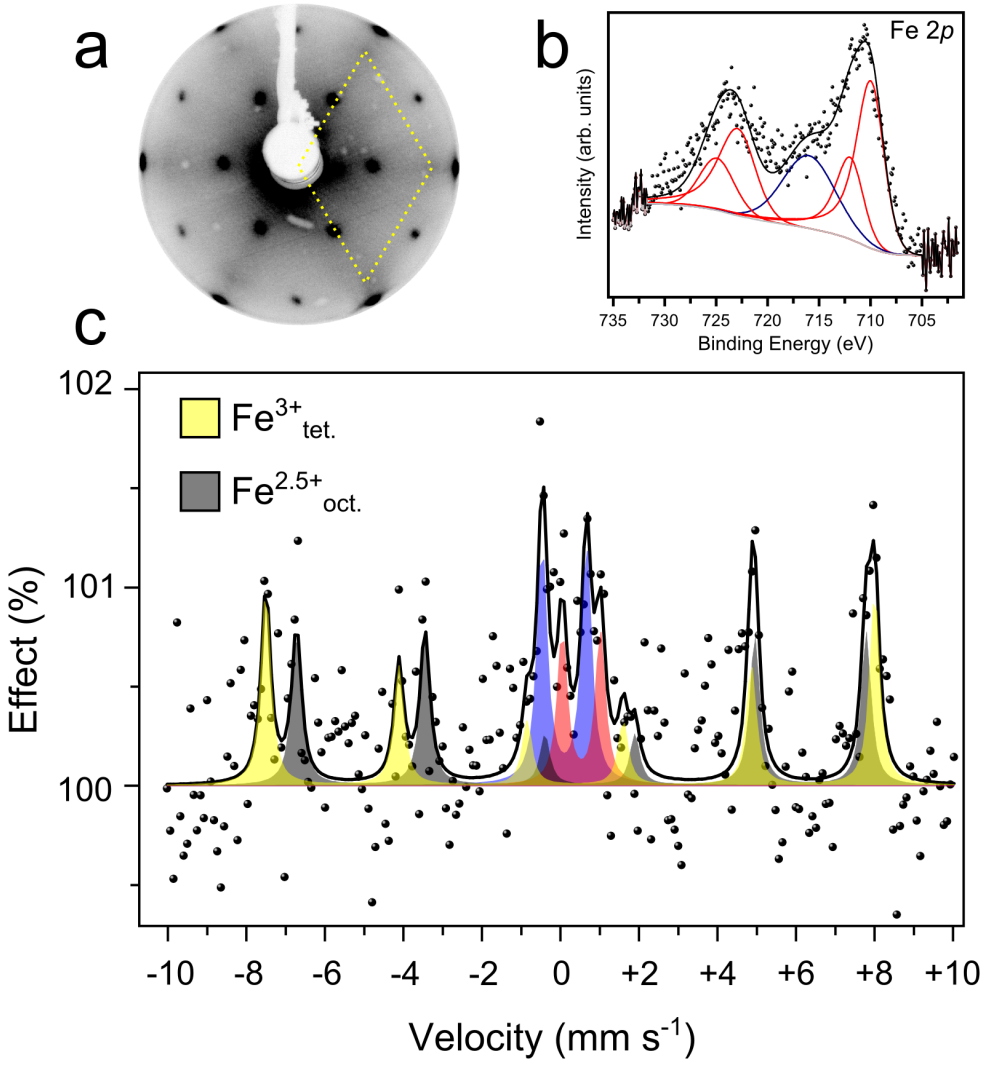

FIGURE 6.11: **a**. LEED pattern collected at 40 eV. The surface unit cell has been depicted using a yellow line. **b**. XPS Fe 2*p* spectrum. The experimental spectrum (black dots) has been fitted using the main Fe 2*p* photoemission peaks (red peaks) together with shake-up contribution (blue peak). **c**. ILEEMS Mössbauer spectrum collected from the bi-component iron oxide film. The experimental spectrum (black dots) has been fitted using two doublets (blue and red) and two sextets (yellow and gray).

the γ source has been situated far away behind a lead collimator (see the schematic in Figure 6.5a), the alignment of the beam becomes a complicate and tedious process. In addition, Ru has an high Z-number that means a large non-resonant electron emission mainly in the form of photoelectrons is expected as result of the ionization produced by the γ beam.

Nevertheless, it is important to remark that the fitting process, carried out using Recoil Mössbauer analysis software, has been performed without any "external" constraints. Thus, the parameters of the sextets, which are unequivocally characteristic of Fe_3O_4, are genuine and do not arise from a fitting procedure carried out with imposed values.

Component	Cation Valence	Hyperfine Field (T)	Isomer Shift (δ) (mm s^{-1})	Quadrupole Splitting (Δ) (mm s^{-1})	Measured Fraction (%)
Doublet (red)	2+		0.53	0.97	13.4±12.1
Doublet (blue)	2+		0.10	1.13	21.4±2.9
Sextet (yellow)	3+	48.10	0.31	-0.07	31.6±6.7
Sextet (gray)	2.5+	45.0	0.65	-0.10	33.5±7.6

TABLE 6.1: Summary of the parameters using for the fitting of the ILEEMS spectrum presented in Figure 6.11c.

6.5 Conclusion

In this chapter the integral low-energy electron Mössbauer spectroscopy has been introduced. After a brief description about the fundamental aspects of the Mössbauer effect and the corresponding spectroscopies, we described the construction of an ILEEMS spectrometer. In particular, we discuss the procedures that allow an enhancement of the surface sensitivity of this uncommon technique. So far, the surface sensitivity in ILEEMS has not been clearly demonstrated: at least it is far from achieving the surface sensitive of other and more common spectroscopies, such as AES or XPS.

In the last section of this chapter, the our results of the application of ILEEMS to the analysis of iron oxide ultrathin films have been presented. The preparation of these samples has been carried out using a home-made ^{57}Fe evaporator and its characterization has been performed by STM, XPS, and LEED. The presented ILEEMS spectrum, recorded from a bi-component iron oxide ultrathin film, has been fitted and discussed. Although it exhibits a poor signal-to-noise ratio, we are able to distinguish a paramagnetic and a ferrimagnetic components. The paramagnetic contribution can be explained by the presence of FeO layers covering the substrate ($\sim$2 ML_{FeO}). The ferrimagnetic contribution can be interpreting by invoking the existence of magnetite islands nucleated on the FeO layers. Moreover, these arguments agree with the XMCD results obtained on similar bi-component iron oxide films in which, despite its reduced thickness ($\sim$1 nm), magnetite crystals maintained the ferrimagnetic order. Unfortunatly, this ILEEMS spectrum preclude a detailed interpretation of the stoichiometry and magnetic properties of the magnetite because its poor signal-to-noise ratio.

Summarizing, ILEEMS remains a promising tool for surface science. Indeed, it has been demonstrated by its capabilities in the *in situ* analysis of iron oxide ultrathin films. Since ILEEMS is UHV compatible, it can be associated with diffraction, microscopy and spectroscopy techniques for a more complete investigation. Our ILEEMS ultrathin film experiment shows a very long acquisition time. We expect that a different substrate

with a lower Z-number, together with the increase of the illumination area would improve the measurement time.

Chapter 7

Conclusions

In this thesis several aspects of ultrathin iron oxide films have been investigated by a surface science approach. The preparation of iron oxide films and a detailed study of their chemical and physical properties was motivated by the potential application of these materials in microelectronics, and catalysis.

- FeO grown by O–MBE nucleates in bilayer or monolayer mode depending on the oxygen pressure. The concentration of absorbed oxygen on Ru plays a fundamental role driving the nucleation mode: the nucleation of a bilayer/monolayer FeO film is preferred in such a way that the concentration of absorbed oxygen is maintained below a critical value. The desired growth mechanism can be induced by changing the experimental parameters.

- By means of microscopy, diffraction and spectroscopy we have observed that magnetite can be stable even when the crystal thickness is reduced to the unit cell limit. X-ray magnetic circular dichroism reveals that these magnetite crystals maintain their ferrimagnetic order up to 520 K indicating that the magnetite's magnetic properties can be preserved at the nanometer limit. This is due to the structural and chemical quality of these crystals which have been grown from a single nuclei and are presumably free of APBs. A deviation of the values of the orbital and spin moments from those usually expected for this material has been observed. However their ratio (m_{orb}/m_{spin}) agrees with the values reported for bulk magnetite. Because the electronic and magnetic properties of magnetite seem to be maintained in carefully grown ultrathin crystals, the application of this material in the spintronic and microelectronic fields should be possible at the nanometer thickness limit.

- The exposure of a bicomponent Fe_3O_4/FeO film to a NO_2 atmosphere gives place to two different oxidation pathways: FeO oxidizes hematite and magnetite to maghemite. In both cases the transformation is interpreted by considering a topotactic mechanism involving the migration of divalent iron cations towards the surface and the subsequent oxidation to trivalent iron cations. The fabrication of ultrathin iron oxide films with same chemical composition and different structures can be tailored by selecting accurately the experimental parameters.

- An ILEEMS spectrometer has been designed and built. This spectrometer is able to distinguish between surface and bulk properties and shows, a better surface-sensitivity than other electron Mössbauer spectroscopies. The first results about ultrathin iron oxide films establish the potential application of ILEEMS for surface-science studies, using an *in situ* approach.

- LEEM is an important tool when the ability for fast real-spacing imaging is required. In fact, because the observation of growth and surface dynamics can easily be performed using this instrument, the study of unexpected pathways of surface evolution becomes available. This information is usually hidden to more common surface science techniques (STM or AFM) that allow to observe the final result, not the path in a dynamic way.

- The combination of spatially-resolved and element-selective techniques allows a precise characterization of the sample surface. These methods become incredibly powerful when the prepared sample is composed by different phases that cannot be differentiated using more common techniques that provide averaged results. In this investigation, XPEEM/LEEM was crucial in order to interpret the chemical and physical nature of the prepared nanostructures.

- Since the chemical and physical properties of the materials studied can be strongly influenced by surface effects, an *in situ* approach is compulsory. For all the experiments presented in this thesis, the characterization of the samples has been carried out immediately after their preparation, in the same experimental system: the observed properties are genuine of the samples and they have not been modified by any kind of interaction with the environment.

Future work envisaged

A more detailed study of FeO transition to a magnetite phase would be interesting. Although we have observed an initial stage of this oxidation process, the detailed mechanism is still unknown. For this purpose, theoretical calculations are in progress in order

to understand the FeO-to-magnetite conversion pathway. We anticipate that the initial calculations suggest that the formation of iron vacancies followed by their rearrangement could lead to a magnetite-like oxide.

For magnetite, the main goal is to obtain a more detailed knowledge about its magnetic and electronic properties. In particular, we have not obtained information about the dependence of these properties with the temperature since that the characterization has been carried out at room (or higher) temperature. Thus, considering the classic magnetite's Verwey transition, an important challenge could be the study of the variation of these magnetic and electronic properties at low temperatures.

Finally, an improvement of the ILEEMS experimental setup seems to be necessary in order to favor its routinary use. In fact, the ILEEMS capabilities could be fundamental to understand the already mentioned unanswered questions, such as the oxidation mechanisms or the magnetic properties of magnetite.

Chapter 8

Conclusiones

En el transcurso de esta tesis se han estudiado distintos aspectos de los óxidos de hierro preparados en forma de películas delgadas desde el punto de vista de la fisicoquímica de superficie. Este trabajo de investigación ha sido motivado por la necesidad de controlar la preparación de dichas estructuras, para su potencial aplicación en campos como la microelectrónica o la catálisis.

- Se han crecido películas ultradelgadas de FeO sobre Ru mediante epitaxia de haces moleculares asistida por oxígeno (O–MBE). Hemos observado que dichos óxidos nuclean en islas de una o dos capas atómicas dependiendo de la presión de oxigeno utilizada. Cuando la presión de oxígeno es suficientemente elevada la formación de islas de dos alturas permite mantener la concentración de oxígeno adsorbido en el Ru por debajo de un nivel crítico. Así, la inducción de una morfología particular se puede llevar a cabo controlando los parámetros experimentales.

- Hemos estudiado cristales de magnetita de espesor nanométrico utilizando técnicas espectroscópicas, de microscopía y de difracción. Hemos demostrado la estabilidad de dichos cristales aunque su espesor está cercano a una celda unidad. Mediante dicroísmo magnético circular hemos observado el carácter ferrimagnetico de los cristales crecidos. Este resultado demuestra que si la magnetita presenta una perfección estructural adecuada, mantiene sus propiedades magnéticas a espesores nanométricos. Hemos estimado los momentos orbital y de espín de los cristales de magnetita. Si bien el momento total es mas pequeño de lo esperado, el ratio entre componente orbital y de espín (m_{orb}/m_{spin}) es comparable con los resultados publicados. Por tanto, las propiedades magnéticas y electrónicas de la magnetita bulk parecen mantenerse en películas ultradelgadas, confirmando la potencial aplicación de este material, entre otros, en el campo de la microelectrónica.

- Tras exponer una película ultradelgada de magnetita y FeO a un gas oxidante NO_2, se observan dos reacciones distintas de oxidación: FeO se oxida a hematita, mientras la magnetita se oxida a maghemita. En ambos casos la reacción de oxidación se ha explicado utilizando un mecanismo topotáctico en el cual la migración de los cationes de hierro divalentes hacia la superficie es seguida de una oxidación a cationes trivalentes. Hemos demostrado que la preparación de películas delgadas compuestas por óxidos con equivalente estado de oxidación y diferente estructura es posible utilizando adecuado parámetros experimentales.

- Hemos construido un espectrómetro ILEEMS. Optimizando el espectrómetro hemos podido incrementar la sensibilidad superficial de la técnica ILEEMS respecto de la de ICEMS. Los primeros resultados obtenidos analizando películas ultradelgadas de óxidos de hierro han demostrado las posibilidades de la técnica desarrollada en los estudios de superficies.

- El microscopio LEEM permite una rápida observación de la superficie y el estudio de procesos dinámicos superficiales que normalmente no son visibles utilizando las microscopías más comunes como STM, y AFM. De hecho, estas técnicas proporcionan información sobre el estado inicial y final de la superficie impidiendo el análisis detallado de su evolución. El uso de la microscopía LEEM ha sido fundamental para observar la superficie en tiempo real y por tanto estudiar el crecimiento de las películas delgadas.

- La utilización de un XPEEM/LEEM ha sido fundamental para la correcta interpretación, caracterización e identificación de las propiedades químico físicas de las nanoestructuras preparadas. La capacidad de dicho microscopio de proporcionar información con sensibilidad espacial y elemental ha demostrado ser crucial cuando la superficie presenta diferentes fases y no puede ser perfectamente caracterizada con técnicas convencionales que proporcionan información promediada.

- Las propiedades químico físicas de las películas ultradelgadas pueden ser modificadas por efectos superficiales. En consecuencia, es necesario realizar medidas *in situ* para evitar cualquier tipo de reacción de la superficie con la atmósfera circundante. Por este motivo hemos caracterizado las muestras en el mismo sistema de preparación sin que estén nunca en contacto con el exterior.

Perspectivas de trabajo futuro

Es necesario un estudio más detallado sobre la transición de FeO a magnetita. Aunque hemos estudiado las etapas iniciales del proceso de oxidación del FeO, todavía no

está claro el mecanismo preciso que está involucrado en esta transición. Por este motivo, se están llevando a cabo cálculos teóricos encaminados a entender el proceso de formación de la magnetita. Podemos anticipar que los primeros cálculos sugieren el papel crucial de la formación y la reordenación de vacantes de hierro en la transformación de FeO en magnetita.

Acerca de la magnetita, el reto fundamental es alcanzar un conocimiento detallado de sus propiedades magnéticas y electrónicas. Como los experimentos han sido realizados a temperatura ambiente, no tenemos información sobre la dependencia de dichas propiedades con la temperatura. En concreto, es necesario un estudio de las propiedades de los cristales de magnetita a baja temperatura, para poder caracterizar la (posible) transición de Verwey en capas delgadas.

Finalmente, un perfeccionamiento del espectrómetro ILEEMS es necesario para un uso rutinario de la técnica. De hecho las posibilidades de la técnica ILEEMS pueden ser utilizadas para responder a las cuestiones que quedan por resolver.

Appendix A

Sample Holder

The sample holder used in the "Surfmoss" UHV chamber has been customized from a previous design [15] at the at the "Rocasolano" machine shop. Figure A.1 show several view of a cartridge that is made of titanium and is iron-free, i.e., suitable for Mössbauer measurements. The sample holder allows to heat the sample by electron bombardment of the rear of the sample by means of a filament (0.15 mm, diameter) directly mounted in the sample holder as shown in Figure A.1 (label 3). The filament is housed inside an alumina crucible since to avoid the cartridge overheating. A precise measurement of the sample temperature is carried out using a tungsten/rhenium alloy (W-5%Re versus W-26%Re) thermocouple, spot welded to the sample. Our design allows to reach high temperatures (up to 2000 K) in a few second for short flashes.

Samples can be transferred quickly between the different position of the chamber by means a transfer bar. Since the chamber is characterized by different operating positions (XPS, STM, ILEEMS, prepation chamber, fast-entry, parking station), the transfer mechanism has also been customized by us in order to allow an easy assembling in each position (see Figure A.2).

Figure A.3 shows the sample holder in the XPS position. The customized manipulator allows electrical contacts (filament and thermocouple) by means of copper flaps that touch the contact screw on the bottom of the cartridge A.1d. Moreover, an home-made tilting mechanism allows to align the sample normal for LEED measurements.

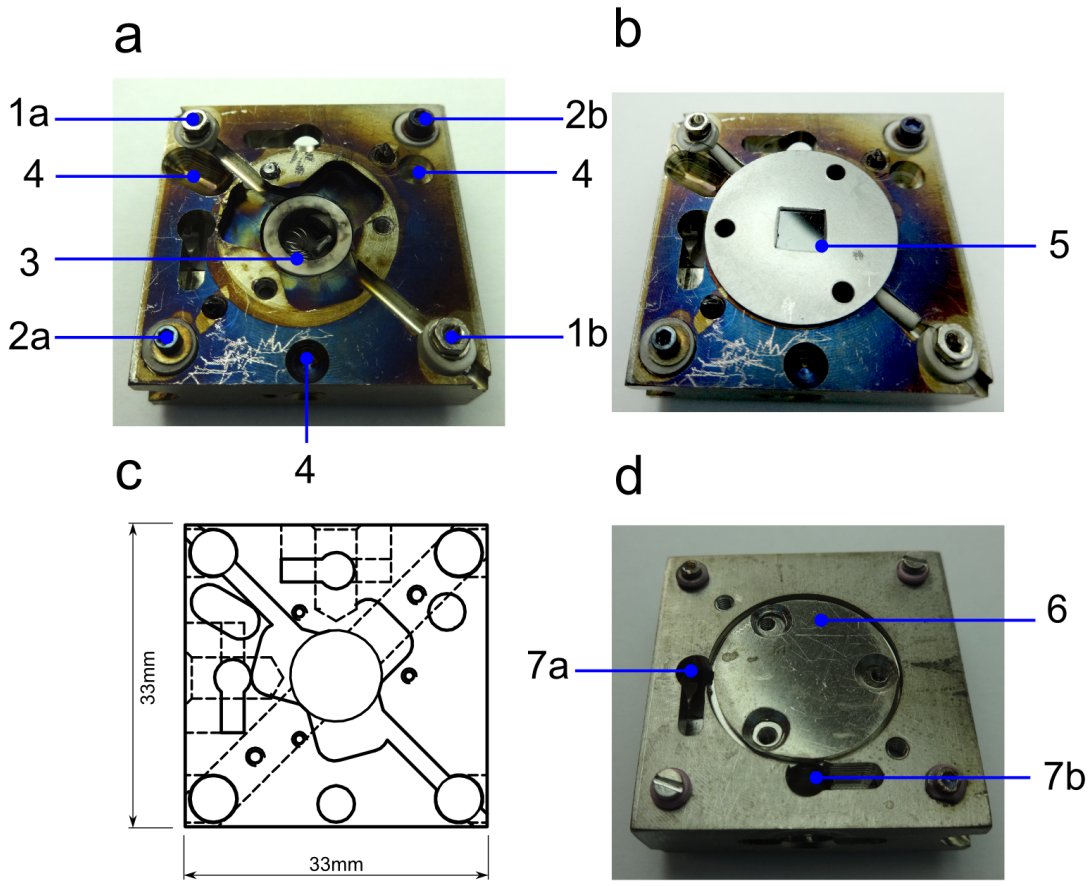

FIGURE A.1: Pictures of the cartridge, used in the "Surfmoss" UHV chamber. **a**. Front view without the sample. The thermocouple contacts have been labeled as 1a and 1b. The filament contacts have been labeled as 2a and 2b. The alumina crucible where the filament has been store is labeled as 3. Self-alignment grooves for the STM head have been labeled as 4. **b**. Front view of the complete sample holder. The sample (a magnetite crystal) has been labeled as 5. **c**. Plan view of the sample holder. **d**. Rear view of the sample holder. A mu-metal disk (labeled as 6) has been positioned on the bottom. Holes for the introduction of the transfer bar have been labeled as 7a and 7b.

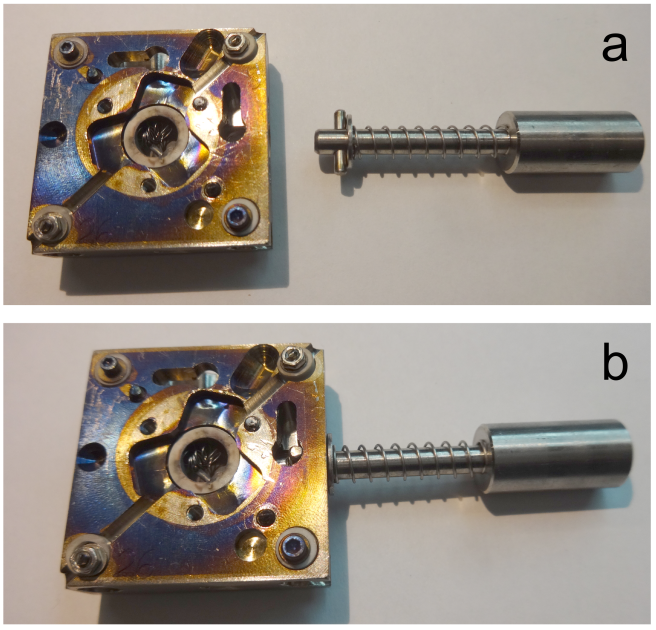

FIGURE A.2: **a** and **b** Pictures of the mechanism designed for the transfer procedures.

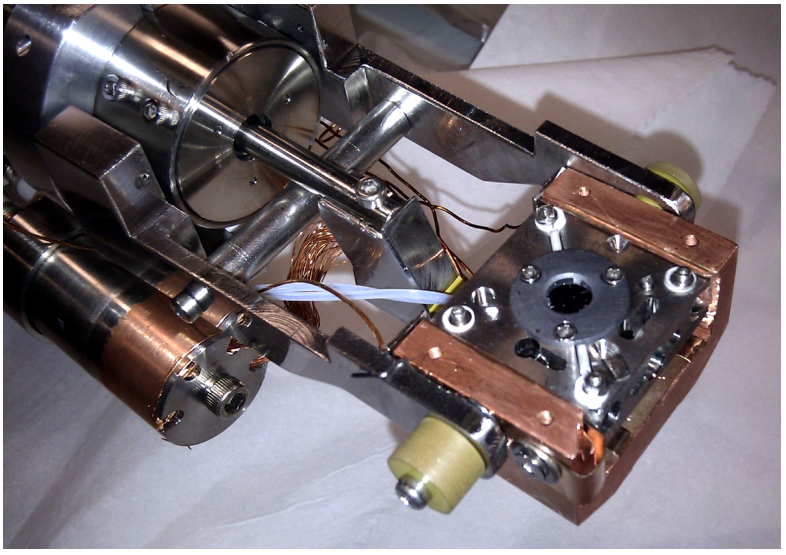

FIGURE A.3: Picture of the sample holder located in the XPS position.

Appendix B

List of Publications

- M. Monti, B. Dal Bianco, R. Bertoncello, and S. Voltolina.
  New protective coatings for ancient glass: Silica thin-films from perhydropolysilazane.
  Journal of Cultural Heritage, 9, e143, 2008.

- T. Herranz, K. F. McCarty, B. Santos, M. Monti, and J. de la Figuera.
  Real space observations of magnesium hydride formation and decomposition.
  Chemistry of Materials, 22, 1291, 2010.

- P. Prieto, M. Monti, J. de la Figuera, J. M. Sanz, and J. F. Marco.
  Mössbauer spectroscopic study of iron-nickel nitrides thin films prepared by ion beam assisted deposition.
  Hyperfine Interactions, 202,47, 2011.

- M. Monti, B. Santos, A. Mascaraque, O. Rodríguez de la Fuente, M. A. Niño, T. O. Menteş, A. Locatelli, K. F. McCarty, J. F. Marco, and J. de la Figuera.
  Magnetism in nanometer-thick magnetite.
  Physical Review B, 85, 020404, 2012.

- M. Monti, B. Santos, A. Mascaraque, O. Rodríguez de la Fuente, M. A. Niño, T. O. Menteş, Andrea Locatelli, Kevin F. McCarty, J. F. Marco, and J. de la Figuera.
  Oxidation pathways in bicomponent ultrathin iron oxide films.
  The Journal of Physical Chemistry C, 116, 11539, 2012.

- M. Sanz, M. Oujja, E. Rebollar, J. F. Marco, J. de la Figuera, M. Monti, A. Bollero, J. Camarero, F. J. Pedrosa, M. García-Hernández, and M. Castillejo.
  Stoichiometric magnetite grown by infrared nanosecond pulsed laser deposition.
  Applied Surface Science, 282, 642–651, 2013.

- J. F. Marco, J. R. Gancedo, M. Monti, and J. de la Figuera.
  Mössbauer spectroscopy and surface analysis.
  V. K. Sharma, G. Klingelhöfer, and T. Nishida, editors, Mössbauer Spectroscopy, 455. John Wiley & Sons, Inc., 2013.

- M. Monti, M. Sanz, M. Oujja, E. Rebollar, M. Castillejo, F. J. Pedrosa, A. Bollero, J. Camarero, J. L. F. Cuñado, N. M. Nemes, F. J. Mompean, M. García-Hernández, S. Nie, K. F. McCarty, A. T. N'Diaye, G. Chen, A. K. Schmid, J. F. Marco, and J. de la Figuera.
  Room temperature in-plane <100> magnetic easy axis for $Fe_3O_4/SrTiO_3(001)$:Nb grown by infrared pulsed laser deposition.
  Journal of Applied Physics, 114, 223902, 2013.

- S. Nie, E. Starodub, M. Monti, D. A. Siegel, L. Vergara, F. El Gabaly, N.C. Bartelt, J. de la Figuera, and K. F. McCarty.
  Insight into Magnetite's Redox Catalysis from Observing Surface Morphology during Oxidation
  Journal of The American Chemical Society, 135, 10091, 2013.

- K. F. McCarty, M. Monti, S. Nie, D. Siegel, E. Starodub, F. El Gabaly, A. McDaniel, A. Shavorskiy, T. Tyliszczak, H. Bluhm, N.C. Bartelt, and J. de la Figuera.
  Oxidation of magnetite (100) to hematite observed by In-situ spectroscopy and microscopy.
  The Journal of Physical Chemistry C, Accepted, 2014.

Bibliography

[1] M. P. Seah and W. A. Dench. Quantitative electron spectroscopy of surfaces: A standard data base for electron inelastic mean free paths in solids. *Surface and Interface Analysis*, 1(1):2, 1979.

[2] J. F. Watts and J. Wolstenholme. *An Introduction to Surface Analysis by XPS and AES*. Wiley, 2003.

[3] Specs^{TM}. www.specs.de, 2014.

[4] J. de la Figuera and K. F. McCarty. Low-energy electron microscopy. In G. Bracco and Bodil Holst, editors, *Surface Science Techniques*, number 51 in Springer Series in Surface Sciences, page 531. Springer Berlin Heidelberg, 2013.

[5] L. R. Merte, J. Knudsen, L. C. Grabow, R. T. Vang, E. Lægsgaard, M. Mavrikakis, and F. Besenbacher. Correlating STM contrast and atomic-scale structure by chemical modification: Vacancy dislocation loops on FeO/Pt(111). *Surface Science*, 603(2):L15, 2009.

[6] J. M. D. Coey and S. Sanvito. Magnetic semiconductors and half-metals. *Journal of Physics D: Applied Physics*, 37(7):988, 2004.

[7] M. Gracia, J. F. Marco, J. R. Gancedo, W. Exel, and W. Meisel. Surface spectroscopic study of the corrosion of ultrathin ^{57}Fe-evaporated and Langmuir–Blodgett films in humid SO_2 environments. *Surface and Interface Analysis*, 29(1):82, 2000.

[8] M. Ritter and W. Weiss. $Fe_3O_4(111)$ surface structure determined by LEED crystallography. *Surf. Sci.*, 432(1-2):81, 1999.

[9] Dominic P. E. Dickson and Frank J. Berry. *Mössbauer Spectroscopy*. Cambridge University Press, Cambridge; New York, 1987.

[10] E. de Grave, R. E. Vandenberghe, and C. Dauwe. ILEEMS: methodology and applications to iron oxides. In R. C. Mercader, J. R. Gancedo, A. Cabral Prieto, and E. Baggio-Saitovitch, editors, *LACAME 2004*, page 147. Springer Berlin Heidelberg, 2005.

[11] J. F. Marco, J. R. Gancedo, M. Monti, and J. de la Figuera. Mössbauer spectroscopy and surface analysis. In V. K. Sharma Ph.D, G. Klingelhöfer, and T. Nishida, editors, *Mössbauer Spectroscopy*, page 455. John Wiley & Sons, Inc., 2013.

[12] R. M. Cornell and U. Schwertmann. *The Iron Oxides*. John Wiley & Sons Ltd, February 1997.

[13] W. Weiss and W. Ranke. Surface chemistry and catalysis on well-defined epitaxial iron-oxide layers. *Progress in Surface Science*, 70(1-3):1, 2002.

[14] SEGAINVEX. http://www.uam.es/, 2014.

[15] B. Diaconescu, G. Nenchev, J. de la Figuera, and K. Pohl. An ultrahigh vacuum fast-scanning and variable temperature scanning tunneling microscope for large scale imaging. *Review of Scientific Instruments*, 78(10):103701, 2007.

[16] B. Santos. *Magnetic and structural properties of ultra-thin metallic layers upon hydrogen exposure*. PhD thesis, Universidad Autónoma de Madrid, Madrid, 2011.

[17] G. Binnig, H. Rohrer, Ch. Gerber, and E. Weibel. Surface studies by scanning tunneling microscopy. *Physical Review Letters*, 49(1):57, 1982.

[18] G. Binnig and H. Rohrer. Scanning tunneling microscopy. *Surface Science*, 126 (1–3):236, 1983.

[19] G. Binnig and H. Rohrer. Scanning tunneling microscopy—from birth to adolescence. *Reviews of Modern Physics*, 59(3):615, 1987.

[20] J. P. Ibe, P. P. Bey Jr, S. L. Brandow, R. A. Brizzolara, N. A. Burnham, D. P. DiLella, K. P. Lee, C. R. K. Marrian, and R. J. Colton. On the electrochemical etching of tips for scanning tunneling microscopy. *Journal of Vacuum Science & Technology A*, 8(4):3570, 1990.

[21] P. Nečas D. Klapetek and Anderson C. Gwyddion user guide – www.gwyddion.net, 2014.

[22] G. Ertl and J. Küppers. *Low energy electrons and surface chemistry*. Wiley-VCH Verlag GmbH, 1985.

[23] J. B. Pendry. *Low Energy Electron Diffraction: The Theory and Its Application to Determination of Surface Structure*. Academic Press Inc., 1974.

[24] E. A. Wood. Vocabulary of surface crystallography. *Journal of Applied Physics*, 35(4):1306, 1964.

[25] G. A. Somorjai and Y. Li. *Introduction to surface chemistry and catalysis, second edition*. John Wiley & Sons, Hoboken, N.J., 2010.

[26] J. F. Moulder, J. Chastain, and R. C. King. *Handbook of x-ray photoelectron spectroscopy: a reference book of standard spectra for identification and interpretation of XPS data*. Physical Electronics, 1995.

[27] D. Briggs and M. P. Seah. *Practical surface analysis: by auger and x-ray photoelectron spectroscopy*. Wiley, 1983.

[28] W. Telieps and E. Bauer. An analytical reflection and emission UHV surface electron microscope. *Ultramicroscopy*, 17(1):57, 1985.

[29] E. Bauer. Low energy electron microscopy. *Reports on Progress in Physics*, 57(9): 895, 1994.

[30] L. H. Veneklasen. Design of a spectroscopic low-energy electron microscope. *Ultramicroscopy*, 36(1–3):76, 1991.

[31] R. M. Tromp. Measuring and correcting aberrations of a cathode objective lens. *Ultramicroscopy*, 111(4):273, 2011.

[32] W. F. Chung and M. S. Altman. Step contrast in low energy electron microscopy. *Ultramicroscopy*, 74(4):237, 1998.

[33] E. Loginova, N. C. Bartelt, P. J. Feibelman, and K. F. McCarty. Evidence for graphene growth by C cluster attachment. *New Journal of Physics*, 10(9):093026, 2008.

[34] J. de la Figuera, N. C. Bartelt, and K. F. McCarty. Electron reflectivity measurements of Ag adatom concentrations on W(110). *Surface Science*, 600:4062, 2006.

[35] S. Nie, E. Starodub, M. Monti, D. A. Siegel, L. Vergara, F. El Gabaly, N. C. Bartelt, J. de la Figuera, and K. F. McCarty. Insight into magnetite's redox catalysis from observing surface morphology during oxidation. *Journal of the American Chemical Society*, 135(27):10091, 2013.

[36] A. Barinov, P. Dudin, L. Gregoratti, A. Locatelli, T. O. Menteş, M. A. Niño, and M. Kiskinova. Synchrotron-based photoelectron microscopy. *Nuclear Instruments and Methods in Physics Research Section A: Accelerators, Spectrometers, Detectors and Associated Equipment*, 601(1–2):195, 2009.

[37] A. Locatelli and E Bauer. Recent advances in chemical and magnetic imaging of surfaces and interfaces by XPEEM. *Journal of Physics: Condensed Matter*, 20(9): 093002, 2008.

[38] A. Locatelli, L. Aballe, T. O Mentes, M. Kiskinova, and E. Bauer. Photoemission electron microscopy with chemical sensitivity: SPELEEM methods and applications. *Surface and Interface Analysis*, 38:1554, 2006.

[39] A. Locatelli. Nanospectroscopy beamline website – www.elettra.trieste.it, 2014.

[40] B. Santos, E. Loginova, A. Mascaraque, A. K. Schmid, K. F. McCarty, and J. de la Figuera. Structure and magnetism in ultrathin iron oxides characterized by low energy electron microscopy. *Journal of Physics: Condensed Matter*, 21(31):314011, 2009.

[41] I. J. Malik and J. Hrbek. Very high atomic oxygen coverages on Ru(001). *Journal of Vacuum Science & Technology A*, 10(4):2565, 1992.

[42] W. J. Mitchell and W. H. Weinberg. Interaction of NO_2 with Ru(001): Formation and decomposition of RuO_x layers. *The Journal of Chemical Physics*, 104(22): 9127, 1996.

[43] J. I. Flege, J. Hrbek, and P. Sutter. Structural imaging of surface oxidation and oxidation catalysis on Ru(0001). *Physical Review B*, 78(16):165407, 2008.

[44] J. I. Flege and P. Sutter. Nanoscale analysis of Ru(0001) oxidation using low-energy and photoemission electron microscopy. *Journal of Physics: Condensed Matter*, 21(31):314018, 2009.

[45] W. Schweika, A. Hoser, M. Martin, and A. E. Carlsson. Defect structure of ferrous oxide $Fe_{1-x}O$. *Physical Review B*, 51(22):15771, 1995.

[46] G. H. Vurens, M. Salmeron, and G. A. Somorjai. Structure, composition and chemisorption studies of thin ordered iron oxide films on platinum (111). *Surface Science*, 201(1–2):129, 1988.

[47] G. H. Vurens, V. Maurice, M. Salmeron, and G. A. Somorjai. Growth, structure and chemical properties of FeO overlayers on Pt(100) and Pt(111). *Surface Science*, 268(1–3):170, 1992.

[48] Q. Fu, F. Yang, and X. Bao. Interface-confined oxide nanostructures for catalytic oxidation reactions. *Accounts of Chemical Research*, 46(8):1692, 2013.

[49] Y. N. Sun, Z. H. Qin, M. Lewandowski, E. Carrasco, M. Sterrer, S. Shaikhutdinov, and H. J. Freund. Monolayer iron oxide film on platinum promotes low temperature CO oxidation. *Journal of Catalysis*, 266(2):359, 2009.

[50] L. Giordano, M. Lewandowski, I. M. N. Groot, Y. N. Sun, J. Goniakowski, C. Noguera, S. Shaikhutdinov, G. Pacchioni, and H. J. Freund. Oxygen-induced

transformations of an FeO(111) film on Pt(111): a combined DFT and STM study. *The Journal of Physical Chemistry C*, 114(49):21504, 2010.

[51] Y. Sun, L. Giordano, J. Goniakowski, M. Lewandowski, Z. Qin, C. Noguera, S. Shaikhutdinov, G. Pacchioni, and H. J. Freund. The interplay between structure and CO oxidation catalysis on metal-supported ultrathin oxide films. *Angewandte Chemie International Edition*, 49(26):4418, 2010.

[52] L. Xu, Z. Wu, Y. Zhang, B. Chen, Z. Jiang, Y. Ma, and W. Huang. Hydroxyls-involved interfacial CO oxidation catalyzed by FeO_x(111) monolayer islands supported on Pt(111) and the unique role of oxygen vacancy. *The Journal of Physical Chemistry C*, 115(29):14290, 2011.

[53] X. Liu, O. Korotkikh, and R. Farrauto. Selective catalytic oxidation of CO in H_2: structural study of Fe oxide-promoted Pt/alumina catalyst. *Applied Catalysis A: General*, 226(1–2):293, 2002.

[54] T. Ma, Q. Fu, H. Su, H. Liu, Y. Cui, Z. Wang, R. Mu, W. Li, and X. Bao. Reversible structural modulation of Fe–Pt bimetallic surfaces and its effect on reactivity. *Physical Chemistry Chemical Physics*, 10(7):1013, 2009.

[55] P. N. Duchesne, G. Chen, N. Zheng, and P. Zhang. Local structure, electronic behavior, and electrocatalytic reactivity of CO-Reduced Platinum–Iron oxide nanoparticles. *The Journal of Physical Chemistry C*, 117(49):26324, 2013.

[56] A. Basińska, T. P. Maniecki, and W. K. Józwiak. Catalytic activity in water-gas shift reaction of platinum group metals supported on iron oxides. *Reaction Kinetics and Catalysis Letters*, 89(2):319, 2006.

[57] L. Xu, Z. Wu, Y. Jin, Y. Ma, and W. Huang. Reaction mechanism of WGS and PROX reactions catalyzed by Pt/oxide catalysts revealed by an FeO(111)/Pt(111) inverse model catalyst. *Physical Chemistry Chemical Physics*, 15(29):12068, 2013.

[58] L. Xu, Z. Wu, W. Zhang, Y. Jin, Q. Yuan, Y. Ma, and W. Huang. Oxygen vacancy-induced novel low-temperature water splitting reactions on FeO(111) monolayer-thick film. *The Journal of Physical Chemistry C*, 116(43):22921–22929, November 2012.

[59] U. Leist, W. Ranke, and K. Al-Shamery. Water adsorption and growth of ice on epitaxial Fe_3O_4(111), FeO(111) and Fe_2O_3(biphase). *Physical Chemistry Chemical Physics*, 5(11):2435, 2003.

[60] Y. Joseph, W. Ranke, and W. Weiss. Water on FeO(111) and Fe_3O_4(111): adsorption behavior on different surface terminations. *The Journal of Physical Chemistry B*, 104(14):3224, 2000.

[61] X. Deng, J. Lee, C. Wang, C. Matranga, F. Aksoy, and Z. Liu. In situ observation of water dissociation with lattice incorporation at FeO particle edges using scanning tunneling microscopy and x-ray photoelectron spectroscopy. *Langmuir*, 27(6):2146, 2011.

[62] Q. Fu, W. X. Li, Y. X. Yao, H. Y. Liu, H. Y. Su, D. Ma, X. K. Gu, L. M. Chen, Z. Wang, H. Zhang, B. Wang, and X. H. Bao. Interface-confined ferrous centers for catalytic oxidation. *Science*, 328:1141, 2010.

[63] L. Giordano, G. Pacchioni, C. Noguera, and J. Goniakowski. Identification of active sites in a realistic model of strong Metal–Support interaction catalysts: The case of platinum (111)-supported iron oxide film. *ChemCatChem*, 6(1):185, 2014.

[64] R. Ouyang and W. Li. Adsorbed CO induced change of the adsorption site and charge of Au adatoms on FeO(111)/Ru(0001). *Chinese Journal of Catalysis*, 34 (10):1820, 2013.

[65] Q. Fu, Y. Yao, X. Guo, M. Wei, Y. Ning, H. Liu, F. Yang, Z. Liu, and X. Bao. Reversible structural transformation of FeO_x nanostructures on Pt under cycling redox conditions and its effect on oxidation catalysis. *Physical Chemistry Chemical Physics*, 15(35):14708, 2013.

[66] R. Meyer, M. Bäumer, S. K. Shaikhutdinov, and H. J. Freund. Two-dimensional growth of Pd on a thin FeO(111) film: a physical manifestation of strong metal-support interaction. *Surface Science*, 546(2–3):L813, 2003.

[67] S. J. Tauster, S. C. Fung, and R. L. Garten. Strong metal-support interactions. Group 8 noble metals supported on titanium dioxide. *Journal of the American Chemical Society*, 100(1):170, 1978.

[68] S. J. Tauster and S. C. Fung. Strong metal-support interactions: Occurrence among the binary oxides of groups IIA–VB. *Journal of Catalysis*, 55(1):29, 1978.

[69] Y. Sun, Z. Qin, M. Lewandowski, S. Kaya, S. Shaikhutdinov, and H. J. Freund. When an encapsulating oxide layer promotes reaction on noble metals: Dewetting and in situ formation of an "inverted" FeO_x/Pt catalyst. *Catalysis Letters*, 126 (1-2):31, 2008.

[70] Y. J. Kim, C. Westphal, R. X. Ynzunza, Z. Wang, H. C. Galloway, M. Salmeron, M. A. Van Hove, and C. S. Fadley. The growth of iron oxide films on Pt(111): a combined XPD, STM, and LEED study. *Surface Science*, 416(1–2):68, 1998.

[71] H. C. Galloway, P. Sautet, and M. Salmeron. Structure and contrast in scanning tunneling microscopy of oxides: FeO monolayer on Pt(111). *Physical Review B*, 54(16):R11145, 1996.

[72] H. C. Galloway, J. J. Benítez, and M. Salmeron. The structure of monolayer films of FeO on Pt(111). *Surface Science*, 298(1):127, 1993.

[73] S. Shaikhutdinov, M. Ritter, and W. Weiss. Hexagonal heterolayers on a square lattice: A combined STM and LEED study of FeO(111) on Pt(100). *Physical Review B*, 62(11):7535, 2000.

[74] A. N. Koveshnikov, R. H. Madjoe, J. Karunamuni, R. L. Stockbauer, and R. L. Kurtz. Oxidized ultrathin Fe films on Cu(001). *Journal of Applied Physics*, 87: 5929, 2000.

[75] G. Ketteler and W. Ranke. Heteroepitaxial growth and nucleation of iron oxide films on Ru(0001). *The Journal of Physical Chemistry B*, 107(18):4320, 2003.

[76] G. Ketteler and W. Ranke. Self-assembled periodic Fe_3O_4 nanostructures in ultrathin FeO(111) films on ru(0001). *Physical Review B*, 66:033405, 2002.

[77] G. Ketteler, W. Ranke, and R. Schlogl. An interfactant for metal oxide heteroepitaxy: Growth of dispersed ZrO_2(111) films on FeO(111) precovered Ru(0001). *Physical Chemistry Chemical Physics*, 6:205, 2004.

[78] M. Monti, B. Santos, A. Mascaraque, O. de la Fuente R., M. A. Niño, T. O. Menteş T., A. Locatelli, K. F. McCarty, J. F. Marco, and J. de la Figuera. Magnetism in nanometer-thick magnetite. *Physical Review B*, 85:020404, 2012.

[79] I. Palacio, M. Monti, J. F. Marco, K. F. McCarty, and J. de la Figuera. Initial stages of FeO growth on Ru(0001). *Journal of Physics: Condensed Matter*, 25 (48):484001, 2013.

[80] N. A. Khan and C. Matranga. Nucleation and growth of Fe and FeO nanoparticles and films on Au(111). *Surface Science*, 602(4):932, 2008.

[81] C. Ruby. Preparation and characterisation of iron oxide films deposited on MgO(100). *Thin Solid Films*, 352(1-2):22, 1999.

[82] I. Ermanoski and G. L. Kellogg. Real-time observations of ultra-thin iron oxide film growth on oxygen-deficient YSZ(001). *Surface Science*, 614:1, 2013.

[83] Y. Gao and S. A. Chambers. Heteroepitaxial growth of α-Fe_2O_3, γ-Fe_2O_3 and Fe_3O_4 thin films by oxygen-plasma-assisted molecular beam epitaxy. *Journal of Crystal Growth*, 174(1–4):446, 1997.

[84] S. A. Chambers. Epitaxial growth and properties of thin film oxides. *Surface Science Reports*, 39:105, 2000.

[85] J. Kolaczkiewicz and E. Bauer. Growth and thermal stability of ultrathin films of Fe, Ni, Rh and Pd on the Ru(0001) surface. *Surface Science*, 423(2-3):292, 1999.

[86] J. Knudsen, L. R. Merte, L. C. Grabow, F. M. Eichhorn, S. Porsgaard, H. Zeuthen, R. T. Vang, E. Lægsgaard, M. Mavrikakis, and F. Besenbacher. Reduction of FeO/Pt(111) thin films by exposure to atomic hydrogen. *Surface Science*, 604(1): 11, 2010.

[87] T. Michely and J. Krug. *Islands, Mounds, and Atoms: Patterns and Processes in Crystal Growth Far from Equilibrium*. Springer, 1 edition, 2003.

[88] J. de la Figuera, J. E. Prieto, C. Ocal, and R. Miranda. Scanning-tunneling-microscopy study of the growth of cobalt on Cu(111). *Physical Review B*, 47(19): 13043, 1993.

[89] J. de la de la Figuera, J. M. Puerta, J. I. Cerda, F. El Gabaly, and K. F. McCarty. Determining the structure of Ru(0001) from low-energy electron diffraction of a single terrace. *Surface Science*, 600:L105, 2006.

[90] C. Busse, C. Polop, M. Müller, K. Albe, U. Linke, and T. Michely. Stacking-fault nucleation on Ir(111). *Physical Review Letters*, 91(5):056103, 2003.

[91] C. Noguera. Polar oxide surfaces. *Journal of Physics: Condensed Matter*, 12(31): R367, 2000.

[92] N. S. McIntyre and D.G. Zetaruk. X-ray photoelectron spectroscopic studies of iron oxides. *Analytical Chemistry*, 49:1521, 1977.

[93] S. Gota, E. Guiot, M. Henriot, and M. Gautier-Soyer. Atomic-oxygen-assisted MBE growth of α-fe$_2$o$_3$ on α-Al_2O_3(0001): metastable FeO(111)-like phase at subnanometer thicknesses. *Physical Review B*, 60(20):14387, 1999.

[94] A. P. Grosvenor, B. A. Kobe, M. C. Biesinger, and N. S. McIntyre. Investigation of multiplet splitting of Fe 2*p* XPS spectra and bonding in iron compounds. *Surface and Interface Analysis*, 36(12):1564, 2004.

[95] H. Pfnür, M. Lindroos, and D. Menzel. Investigation of adsorbates with low energy electron diffraction at very low energies (VLEED). *Surface Science*, 248(1-2):1, 1991.

[96] F. El Gabaly, J. M Puerta, C. Klein, A. Saa, A. K. Schmid, K. F. McCarty, J. I. Cerda, and J. de la Figuera. Structure and morphology of ultrathin Co/Ru(0001) films. *New Journal of Physics*, 8:80, 2007.

[97] W. L. Ling, N. C. Bartelt, K. F. McCarty, and C. B. Carter. Twin boundaries can be moved by step edges during film growth. *Physical Review Letters*, 95:166105, 2005.

[98] T. E. Madey, A. H. Engelhardt, and D. Menzel. Adsorption of oxygen and oxidation of CO on the ruthenium (001) surface. *Surface Science*, 48(2):304, 1975.

[99] C. Stampfl, S. Schwegmann, H. Over, M. Scheffler, and G. Ertl. Structure and stability of a High-Coverage (1×1) oxygen phase on Ru(0001). *Physical Review Letters*, 77(16):3371, 1996.

[100] S. Lizzit, A. Baraldi, A. Groso, K. Reuter, M. V. Ganduglia-Pirovano, C. Stampfl, M. Scheffler, M. Stichler, C. Keller, W. Wurth, and D. Menzel. Surface core-level shifts of clean and oxygen-covered Ru(0001). *Physical Review B*, 63(20):205419, 2001.

[101] K.L. Kostov, M. Gsell, P. Jakob, T. Moritz, W. Widdra, and D. Menzel. Observation of a novel high density 3O(2×2) structure on Ru(001). *Surface Science*, 394 (1–3):L138, 1997.

[102] J. A. Venables, G. D. T. Spiller, and M. Hanbucken. Nucleation and growth of thin films. *Reports on Progress in Physics*, 47:399, 1984.

[103] Y. W. Mo, J. Kleiner, M. B. Webb, and M. G. Lagally. Surface self-diffusion of Si on Si(001). *Surface Science*, 268:275, 1992.

[104] J. A. Stroscio, D. T. Pierce, and R. A. F. Dragoset. Homoepitaxial growth of iron and a real space view of reflection-high-energy-electron diffraction. *Physical Review Letters*, 70(23):3615, 1993.

[105] W. M. Robertson. Surface diffusion of oxides: A review. *Journal of Nuclear Materials*, 30(1-2):36, 1969.

[106] A. A. Mills. The lodestone: History, physics, and formation. *Annals of Science*, 61:273, 2004.

[107] J. Stöhr and H. C. Siegmann. *Magnetism: From Fundamentals to Nanoscale Dynamics*. Springer, 2006.

[108] J. E. Lorenzo, C. Mazzoli, N. Jaouen, C. Detlefs, D. Mannix, S. Grenier, Y. Joly, and C. Marin. Charge and orbital correlations at and above the verwey phase transition in magnetite. *Physical Review Letters*, 101(22):226401, 2008.

[109] E. J. Goering. Large hidden orbital moments in magnetite. *physica status solidi (b)*, 248(10):2345, 2011.

[110] I. Leonov, A. N. Yaresko, V. N. Antonov, and V. I. Anisimov. Electronic structure of charge-ordered Fe_3O_4 from calculated optical, magneto-optical Kerr effect, and O K-edge x-ray absorption spectra. *Physical Review B*, 74(16):165117, 2006.

[111] Z. Szotek, W. M. Temmerman, D. Ködderitzsch, A. Svane, L. Petit, and H. Winter. Electronic structures of normal and inverse spinel ferrites from first principles. *Physical Review B*, 74(17):174431, 2006.

[112] D. J. Huang, C. F. Chang, H.-T. Jeng, G. Y. Guo, H.-J. Lin, W. B. Wu, H. C. Ku, A. Fujimori, Y. Takahashi, and C. T. Chen. Spin and orbital magnetic moments of Fe_3O_4. *Physical Review Letters*, 93(7):077204, 2004.

[113] V. N. Antonov, B. N. Harmon, and A. N. Yaresko. Electronic structure and x-ray magnetic circular dichroism in Fe_3O_4 and Mn-, Co-, or Ni-substituted Fe_3O_4. *Physical Review B*, 67(2):024417, 2003.

[114] E. J. Goering, M. Lafkioti, and S. Gold. Comment on "Spin and orbital magnetic moments of Fe_3O_4". *Physical Review Letters*, 96(3):039701, 2006.

[115] E. J. Goering, S. Gold, M. Lafkioti, and G. Schütz. Vanishing Fe $3d$ orbital moments in single-crystalline magnetite. *Europhysics Letters*, 73(1):97, 2006.

[116] E. J. Goering, M. Lafkioti, S. Gold, and G. Schuetz. Absorption spectroscopy and XMCD at the verwey transition of Fe_3O_4. *Journal of Magnetism and Magnetic Materials*, 310(2):e249, 2007.

[117] S. K. Arora, Han-Chun Wu, R. J. Choudhary, I. V. Shvets, O. N. Mryasov, Hongzhi Yao, and W. Y. Ching. Giant magnetic moment in epitaxial Fe_3O_4 thin films on MgO(100). *Physical Review B*, 77:134443, 2008.

[118] W. Q. Liu, Y. B. Xu, P. K. J. Wong, N. J. Maltby, S. P. Li, X. F. Wang, J. Du, B. You, J. Wu, P. Bencok, and R. Zhang. Spin and orbital moments of nanoscale Fe_3O_4 epitaxial thin film on MgO/GaAs(100). *Applied Physics Letters*, 104(14): 142407, 2014.

[119] V. Hari Babu, R. K. Govind, K.-M. Schindler, M. Welke, and R. Denecke. Epitaxial growth and magnetic properties of ultrathin iron oxide films on $BaTiO_3$(001). *Journal of Applied Physics*, 114(11):113901, 2013.

[120] Yinwan Li, P. A. Montano, B. Barbiellini, P. E. Mijnarends, S. Kaprzyk, and A. Bansil. Spin moment over 10–300 K and delocalization of magnetic electrons above the Verwey transition in magnetite. *Journal of Physics and Chemistry of Solids*, 68(8):1556, 2007.

[121] J. A. Duffy, J. W. Taylor, S. B. Dugdale, C. Shenton-Taylor, M. W. Butchers, S. R. Giblin, M. J. Cooper, Y. Sakurai, and M. Itou. Spin and orbital moments in Fe_3O_4. *Physical Review B*, 81(13):134424, 2010.

[122] F. Walz. The Verwey transition - a topical review. *Journal of Physics: Condensed Matter*, 14:R285, 2002.

[123] S. Todo, K. Siratori, and S. Kimura. Transport properties of the high temperature phase of Fe_3O_4. *Journal of the Physical Society of Japan*, 64(6):2118, 1995.

[124] W. Tabis, J. E. Lorenzo, A. Kozlowski, T. Kolodziej, Z. Tarnawski, Z. Kakol, C. Mazzoli, H. C. Walker, N. Jaouen, D. Mannix, C. Marin, and J. M. Honig. Effect of surface polishing and oxidization induced strain on electronic order at the Verwey transition in Fe_3O_4. *Journal of Physics: Condensed Matter*, 25(5): 055603, 2013.

[125] E. J. W. Verwey. Electronic conduction of magnetite Fe_3O_4 and its transition point at low temperatures. *Nature*, 144:327, 1939.

[126] J. de la Figuera, Z. Novotny, M. Setvin, T. Liu, Z. Mao, G. Chen, A. T. N'Diaye, M. Schmid, U. Diebold, A. K. Schmid, and G. S. Parkinson. Real-space imaging of the Verwey transition at the (100) surface of magnetite. *Physical Review B*, 88 (16):161410, 2013.

[127] H. Uzu and A. Tanaka. Complex-orbital order in Fe_3O_4 and mechanism of the Verwey transition. *Journal of the Physical Society of Japan*, 77(7):074711, 2008.

[128] J. P. Wright, J. P. Attfield, and P. G. Radaelli. Charge ordered structure of magnetite Fe_3O_4 below the verwey transition. *Physical Review B*, 66(21):214422, 2002.

[129] E. J. Verwey, P. W. Haayman, and F. C. Romeijn. Physical properties and cation arrangement of oxides with spinel structures II. Electronic conductivity. *The Journal of Chemical Physics*, 15(4):181, 1947.

[130] J. García and G. Subías. The Verwey transition - a new perspective. *Journal of Physics: Condensed Matter*, 16:R145, 2004.

[131] G. Kh. Rozenberg, M. P. Pasternak, W. M. Xu, Y. Amiel, M. Hanfland, M. Amboage, R. D. Taylor, and R. Jeanloz. Origin of the Verwey transition in magnetite. *Physical Review Letters*, 96(4):045705, 2006.

[132] S. C. Weng, Y. R. Lee, C. G. Chen, C. H. Chu, Y. L. Soo, and S. L. Chang. Direct observation of charge ordering in magnetite using resonant multiwave x-ray diffraction. *Physical Review Letters*, 108(14):146404, 2012.

[133] G. Hu and Y. Suzuki. Negative spin polarization of Fe_3O_4 in magnetite/manganite-based junctions. *Physical Review Letters*, 89(27):276601, 2002.

[134] Z. Zhang and S. Satpathy. Electron states, magnetism, and the Verwey transition in magnetite. *Physical Review B*, 44(24):13319, 1991.

[135] M. Pénicaud, B. Siberchicot, C. B. Sommers, and J. Kübler. Calculated electronic band structure and magnetic moments of ferrites. *Journal of Magnetism and Magnetic Materials*, 103(1–2):212, 1992.

[136] M. Fonin, Yu S. Dedkov, R. Pentcheva, U. Rüdiger, and G. Güntherodt. Magnetite: a search for the half-metallic state. *Journal of Physics: Condensed Matter*, 19(31): 315217, 2007.

[137] M. I. Katsnelson, V. Yu. Irkhin, L. Chioncel, A. I. Lichtenstein, and R. A. de Groot. Half-metallic ferromagnets: From band structure to many-body effects. *Reviews of Modern Physics*, 80:315, 2008.

[138] M. Fonin, Y. S. Dedkov, R. Pentcheva, U. Rüdiger, and G. Güntherodt. Spin-resolved photoelectron spectroscopy of Fe_3O_4-revisited. *Journal of Physics: Condensed Matter*, 20(14):142201, 2008.

[139] G. T. Rado and J. M. Ferrari. Electric field dependence of the magnetic anisotropy energy in magnetite (Fe_3O_4). *Physical Review B*, 12(11):5166, 1975.

[140] K. Kato and S. Iida. Observation of ferroelectric hysteresis loop of Fe_3O_4 at 4.2 k. *Journal of the Physical Society of Japan*, 51(5):1335–1336, 1982.

[141] M. Alexe, M. Ziese, D. Hesse, P. Esquinazi, K. Yamauchi, T. Fukushima, S. Picozzi, and U. Gösele. Ferroelectric switching in multiferroic magnetite Fe_3O_4 thin films. *Advance Materials*, 21:4452, 2009.

[142] S.D. Bader and S.S.P. Parkin. Spintronics. *Annual Review of Condensed Matter Physics*, 1(1):71, 2010.

[143] M. Bibes and A. Barthelemy. Oxide spintronics. *IEEE Ttransactions on electron devices*, 54(5):1003, 2007.

[144] J. Korecki, B. Handke, N. Spiridis, T. Ślęzak, I. Flis-Kabulska, and J. Haber. Size effects in epitaxial films of magnetite. *Thin Solid Films*, 412(1–2):14, 2002.

[145] N. T. H. Kim-Ngan, A. G. Balogh, J. D. Meyer, J. Brötz, S. Hummelt, M. Zając, T. Ślęzak, and J. Korecki. Structure, composition and crystallinity of epitaxial magnetite thin films. *Surface Science*, 602(14):2358, 2008.

[146] L. McGuigan, R. C. Barklie, R. G. S. Sofin, S. K. Arora, and I. V. Shvets. In-plane magnetic anisotropies in Fe_3O_4 films on vicinal MgO(100). *Physical Review B*, 77 (17):174424, 2008.

[147] A. Fernández-Pacheco, J. M. De Teresa, J. Orna, L. Morellon, P. A. Algarabel, J. A. Pardo, M. R. Ibarra, C. Magen, and E. Snoeck. Giant planar hall effect in epitaxial Fe_3O_4 thin films and its temperature dependence. *Physical Review B*, 78 (21):212402, 2008.

[148] W. Eerenstein, T. T. M. Palstra, T. Hibma, and S. Celotto. Origin of the increased resistivity in epitaxial Fe_3O_4 films. *Physical Review B*, 66(20):201101, 2002.

[149] W. Eerenstein, T. T. M. Palstra, S. S. Saxena, and T. Hibma. Spin-polarized transport across sharp antiferromagnetic boundaries. *Physical Review Letters*, 88 (24):247204, 2002.

[150] A. Ikeuchi, S. Hiura, T. Mizuno, E. Kaji, A. Subagyo, and K. Sueoka. Atomically resolved observations of antiphase domain boundaries in epitaxial Fe_3O_4 films on MgO(001) by scanning tunneling microscopy. *Japanese Journal of Applied Physics*, 51(8S3):08KB02, 2012.

[151] R. Ramos, S. K. Arora, and I. V. Shvets. Influence of miscut on the anisotropic magnetoresistance of magnetite thin films. *Journal of Applied Physics*, 105(7): 07B108, 2009.

[152] P. A. A. van der Heijden, P. J. H. Bloemen, J. M. Gaines, J. T. W. M. van Eemeren, R. M. Wolf, P. J. van der Zaag, and W. J. M. de Jonge. Magnetic interface anisotropy of MBE-grown ultra-thin (001) Fe_3O_4 layers. *Journal of Magnetism and Magnetic Materials*, 159(3):L293, 1996.

[153] W. Eerenstein, L. Kalev, L. Niesen, T. T. M. Palstra, and T. Hibma. Magnetoresistance and superparamagnetism in magnetite films on MgO and $MgAl_2O_4$. *Journal of Magnetism and Magnetic Materials*, 258-259:73, 2003.

[154] S. van Dijken, X. Fain, S. M. Watts, K. Nakajima, and J. M. D. Coey. Magnetoresistance of Fe_3O_4/Au/Fe_3O_4 and Fe_3O_4/Au/Fe spin-valve structures. *Journal of Magnetism and Magnetic Materials*, 280(2-3):322, 2004.

[155] D. T. Margulies, F. T. Parker, F. E. Spada, R. S. Goldman, J. Li, R. Sinclair, and A. E. Berkowitz. Anomalous moment and anisotropy behavior in Fe_3O_4 films. *Physical Review B*, 53(14):9175, 1996.

[156] F. C. Voogt, T. T. M. Palstra, L. Niesen, O. C. Rogojanu, M. A. James, and T. Hibma. Superparamagnetic behavior of structural domains in epitaxial ultrathin magnetite films. *Physical Review B*, 57(14):R8107, 1998.

[157] T. Hibma, F. C. Voogt, L. Niesen, P. A. A. van der Heijden, W. J. M. de Jonge, J. J. T. M. Donkers, and P. J. van der Zaag. Anti-phase domains and magnetism in epitaxial magnetite layers. *Journal of Applied Physics*, 85(8):5291, 1999.

[158] D. J. Huang, C. F. Chang, J. Chen, L. H. Tjeng, A. D. Rata, W. P. Wu, S. C. Chung, H. J. Lin, T. Hibma, and C. T. Chen. Spin-resolved photoemission studies of epitaxial Fe_3O_4(100) thin films. *Journal of Magnetism and Magnetic Materials*, 239(1–3):261, 2002.

[159] R. Ramos, S. K. Arora, and I. V. Shvets. Anomalous anisotropic magnetoresistance in epitaxial Fe_3O_4 thin films on MgO(001). *Physical Review B*, 78(21):214402, 2008.

[160] C. S. Kelley, J. Naughton, E. Benson, R. C. Bradley, V. K. Lazarov, S. M. Thompson, and J. A. D. Matthew. Investigating the magnetic field-dependent conductivity in magnetite thin films by modelling the magnetorefractive effect. *Journal of Physics: Condensed Matter*, 26(3):036002, 2014.

[161] P. A. A. van der Heijden, M. G. van Opstal, C. H. W. Swüste, P. H. J. Bloemen, J. M. Gaines, and W. J. M. de Jonge. A ferromagnetic resonance study on ultra-thin Fe_3O_4 layers grown on (001)MgO. *Journal of Magnetism and Magnetic Materials*, 182(1–2):71, 1998.

[162] D. T. Margulies, F. T. Parker, M. L. Rudee, F. E. Spada, J. N. Chapman, P. R. Aitchison, and A. E. Berkowitz. Origin of the anomalous magnetic behavior in single crystal Fe_3O_4 films. *Physical Review Letters*, 79(25):5162, 1997.

[163] F. C. Voogt, T. Hibma, G. L. Zhang, M. Hoefman, and L. Niesen. Growth and characterization of non-stoichiometric magnetite $Fe_{3-\delta}O_4$ thin films. *Surface Science*, 331-333(2):1508, 1995.

[164] R. F. C. Farrow, P. M. Rice, M. F. Toney, R. F. Marks, J. A. Hedstrom, R. Stephenson, M. J. Carey, and A. J. Kellock. Nanoscale phase separation in Fe_3O_4(111) films on sapphire(0001) and phase stability of Fe_3O_4(001) films on MgO(001) grown by oxygen-plasma-assisted molecular beam epitaxy. *Journal of Applied Physics*, 93(9):5626, 2003.

[165] A. Tanaka, C. F. Chang, M. Buchholz, C. Trabant, E. Schierle, J. Schlappa, D. Schmitz, H. Ott, P. Metcalf, L. H. Tjeng, and C. Schüßler-Langeheine. Analysis of charge and orbital order in Fe_3O_4 by Fe $L_{2,3}$ resonant x-ray diffraction. *Physical Review B*, 88(19):195110, 2013.

[166] H. L. Abbott, A. Aumer, Y. Lei, C. Asokan, R. J. Meyer, M. Sterrer, S. Shaikhutdinov, and H. J. Freund. CO adsorption on monometallic and bimetallic Au–Pd

nanoparticles supported on oxide thin films. *The Journal of Physical Chemistry C*, 114(40):17099, 2010.

[167] A. Sala, H. Marchetto, Z. H. Qin, S. Shaikhutdinov, T. Schmidt, and H. J. Freund. Defects and inhomogeneities in Fe_3O_4(111) thin film growth on Pt(111). *Physical Review B*, 86(15):155430, 2012.

[168] S. K. Shaikhutdinov, M. Ritter, X. G. Wang, H. Over, and W. Weiss. Defect structures on epitaxial Fe_3O_4(111) films. *Physical Review B*, 60(15):11062–11069, 1999.

[169] Y. Q. Cai, M. Ritter, W. Weiss, and A. M. Bradshaw. Valence-band structure of epitaxially grown Fe_3O_4(111) films. *Physical Review B*, 58(8):5043, 1998.

[170] P. Morrall, F. Schedin, G. S. Case, M. F. Thomas, E. Dudzik, G. van der Laan, and G. Thornton. Stoichiometry of $Fe_{3-\delta}O_4$(111) ultrathin films on Pt(111). *Physical Review B*, 67(21):214408, 2003.

[171] F. Schedin, L. Hewitt, P. Morrall, V. N. Petrov, G. Thornton, S. Case, M. F. Thomas, and V. M. Uzdin. In-plane magnetization of an ultrathin film of Fe_3O_4(111) grown epitaxially on Pt(111). *Physical Review B*, 58(18):R11861, 1998.

[172] W. Weiss, A. Barbieri, M. A. Van Hove, and G. A. Somorjai. Surface structure determination of an oxide film grown on a foreign substrate: Fe_3O_4 multilayer on Pt(111) identified by low energy electron diffraction. *Physical Review Letters*, 71 (12):1848, 1993.

[173] A. Barbieri, W. Weiss, M. A. Van Hove, and G. A. Somorjai. Magnetite Fe_3O_4: surface structure by LEED crystallography and energetics. *Surface Science*, 302 (3):259, 1994.

[174] C. Lemire, R. Meyer, V. E. Henrich, S. Shaikhutdinov, and H. J. Freund. The surface structure of Fe_3O_4(100) films as studied by CO adsorption. *Surface Science*, 572(1):103, 2004.

[175] V. V. Roddatis, D. S. Su, C. Kuhrs, W. Ranke, and R. Schlögl. Transmission electron microscopy investigation of Fe_3O_4 films grown on (111)Pt substrates. *Thin Solid Films*, 396(1–2):78, 2001.

[176] Y. S. Dedkov, U. Rüdiger, and G. Güntherodt. Evidence for the half-metallic ferromagnetic state of Fe_3O_4 by spin-resolved photoelectron spectroscopy. *Physical Review B*, 65(6):064417, 2002.

[177] D. Bruns, S. R. Lindemann, K. Kuepper, T. Schemme, and J. Wollschläger. Fe_3O_4 films on Ag(001)—Generation of high-quality epitaxial ferrimagnetic metal oxide films. *Applied Physics Letters*, 103(5):052401, 2013.

[178] H. Tian, J. Verbeeck, S. Brück, M. Paul, D. Kufer, M. Sing, R. Claessen, and G. van Tendeloo. Interface-induced modulation of charge and polarization in thin film Fe_3O_4. *Advanced Materials*, 26(3):461, 2014.

[179] G. E. Sterbinsky, J. Cheng, P. T. Chiu, B. W. Wessels, and D. J. Keavney. Investigation of heteroepitaxial growth of magnetite thin films. *Journal of Vacuum Science & Technology B*, 25(4):1389, 2007.

[180] J. G. Zheng, G. E. Sterbinsky, J. Cheng, and B. W. Wessels. Epitaxial Fe_3O_4 on $SrTiO_3$ characterized by transmission electron microscopy. *Journal of Vacuum Science & Technology B*, 25(4):1520, 2007.

[181] M. Monti, M. Sanz, M. Oujja, E. Rebollar, M. Castillejo, F. J. Pedrosa, A. Bollero, J. Camarero, J. L. F. Cuñado, N. M. Nemes, F. J. Mompean, M. García-Hernández, S. Nie, K. F. McCarty, A. T. N'Diaye, G. Chen, A. K. Schmid, J. F. Marco, and J. de la Figuera. Room temperature in-plane <100> magnetic easy axis for $Fe_3O_4/SrTiO_3$(001):Nb grown by infrared pulsed laser deposition. *Journal of Applied Physics*, 114(22):223902, 2013.

[182] F. Schedin, E. W. Hill, G. van der Laan, and G. Thornton. Magnetic properties of stoichiometric and nonstoichiometric ultrathin Fe_3O_4(111) films on Al_2O_3(0001). *Journal of Applied Physics*, 96(2):1165, 2004.

[183] T. Fujii, M. Takano, R. Katano, Y. Isozumi, and Y. Bando. Surface and interface properties of epitaxial Fe_3O_4 films studied by Mössbauer spectroscopy. *Journal of Magnetism and Magnetic Materials*, 130(1-3):267, 1994.

[184] J. B. Moussy, S. Gota, A. Bataille, M. J. Guittet, M. Gautier-Soyer, F. Delille, B. Dieny, F. Ott, T. D. Doan, P. Warin, P. Bayle-Guillemaud, C. Gatel, and E. Snoeck. Thickness dependence of anomalous magnetic behavior in epitaxial Fe_3O_4(111) thin films: Effect of density of antiphase boundaries. *Physical Review B*, 70(17):174448, 2004.

[185] K. Matsuzaki, V. K. Lazarov, L. Lari, H. Hosono, and T. Susaki. Fe_3O_4(111) thin films with bulk-like properties: growth and atomic characterization. *Journal of Physics D: Applied Physics*, 46(2):022001, 2013.

[186] D. Gilks, L. Lari, K. Matsuzaki, H. Hosono, T. Susaki, and V. K. Lazarov. Structural study of Fe_3O_4(111) thin films with bulk like magnetic and magnetotransport behaviour. *Journal of Applied Physics*, 115(17):17C107, 2014.

[187] Y. X. Lu, J. S. Claydon, E. Ahmad, Y. B. Xu, M. Ali, B. J. Hickey, S. M. Thompson, J. A. D. Matthew, and K. Wilson. Hybrid Fe_3O_4/GaAs(100) structure for spintronics. *Journal of Applied Physics*, 97(10):10C313, 2005.

[188] S. M. Watts. Transport characteristics of magnetite thin films grown onto GaAs substrates. *Journal of Applied Physics*, 95(11):7465, 2004.

[189] L. Yongxiong, J. S Claydon, E. Ahmad, X. Yongbing, S. M. Thompson, K. Wilson, and G. van der Laan. Xps and xmcd study of Fe_3O_4/GaAs interface. *IEEE Transactions on Magnetics*, 41(10):2808, 2005.

[190] Y. X. Lu, J. S. Claydon, Y. B. Xu, S. M. Thompson, K. Wilson, and G. van der Laan. Epitaxial growth and magnetic properties of half-metallic Fe_3O_4 on GaAs(100). *Physical Review B*, 70(23):233304, 2004.

[191] Y. X. Lu. Magnetic properties of ultrathin Fe_3O_4 on GaAs(100). *Journal of Applied Physics*, 95(11):7228, 2004.

[192] Z. C. Huang, X. F. Hu, Y. X. Xu, Y. Zhai, Y. B. Xu, J. Wu, and H. R. Zhai. Magnetic properties of ultrathin single crystal Fe_3O_4 film on InAs(100) by ferromagnetic resonance. *Journal of Applied Physics*, 111(7):07C108, 2012.

[193] P. K. J. Wong, W. Zhang, X. G. Cui, Y. B. Xu, J. Wu, Z. K. Tao, X. Li, Z. L. Xie, R. Zhang, and G. van der Laan. Ultrathin Fe_3O_4 epitaxial films on wide bandgap GaN(0001). *Physical Review B*, 81(3):035419, 2010.

[194] T. Fujii, M. Takano, R. Katano, Y. Bando, and Y. Isozumi. CEMS study of the growth and properties of Fe_3O_4 films. *Journal of Crystal Growth*, 99(1–4):606, 1990.

[195] D. T. Margulies, F. T. Parker, and A. E. Berkowitz. Magnetic anomalies in single crystal Fe_3O_4 thin films. *Journal of Applied Physics*, 75(10):6097, 1994.

[196] S. Kale, S. M. Bhagat, S. E. Lofland, T. Scabarozi, S. B. Ogale, A. Orozco, S. R. Shinde, T. Venkatesan, B. Hannoyer, B. Mercey, and W. Prellier. Film thickness and temperature dependence of the magnetic properties of pulsed-laser-deposited Fe_3O_4 films on different substrates. *Physical Review B*, 64(20):205413, 2001.

[197] M. Fonin, C. Hartung, U. Rüdiger, D. Backes, L. Heyderman, F. Nolting, A. Fraile Rodríguez, and M. Kläui. Formation of magnetic domains and domain walls in epitaxial Fe_3O_4(100) elements. *Journal of Applied Physics*, 109(7):07D315, 2011.

[198] X. W. Li, A. Gupta, G. Xiao, and G. Q. Gong. Transport and magnetic properties of epitaxial and polycrystalline magnetite thin films. *Journal of Applied Physics*, 83(11):7049, 1998.

[199] J. M. Gaines, P. J. H. Bloemen, J. T. Kohlhepp, C. W. T. Bulle-Lieuwma, R. M. Wolf, A. Reinders, R. M. Jungblut, P. A. A. van der Heijden, J. T. W. M. van Eemeren, J. aan de Stegge, and W. J. M. de Jonge. An STM study of $Fe_3O_4(100)$ grown by molecular beam epitaxy. *Surface Science*, 373(1):85, 1997.

[200] T. Kasama, R. E. Dunin-Borkowski, and W. Eerenstein. Off-axis electron holography observation of magnetic microstructure in a magnetite (001) thin film containing antiphase domains. *Physical Review B*, 73(10):104432, 2006.

[201] S. K. Arora, R. G. S. Sofin, and I. V. Shvets. Magnetoresistance enhancement in epitaxial magnetite films grown on vicinal substrates. *Physical Review B*, 72(13): 134404, 2005.

[202] J. B. Moussy. From epitaxial growth of ferrite thin films to spin-polarized tunnelling. *Journal of Physics D: Applied Physics*, 46(14):143001, 2013.

[203] T. Fujii, F. M. F. de Groot, G. A. Sawatzky, F. C. Voogt, T. Hibma, and K. Okada. In situ XPS analysis of various iron oxide films grown by NO_2-assisted molecular-beam epitaxy. *Physical Review B*, 59(4):3195, 1999.

[204] M. Zajac, K. Freindl, T. Ślęzak, M. Ślęzak, N. Spiridis, D. Wilgocka Ślęzak, and J. Korecki. Electronic and magnetic properties of ultra-thin epitaxial magnetite films on MgO(001). *Thin Solid Films*, 519(16):5588, 2011.

[205] G. Ketteler, W. Weiss, W. Ranke, and R. Schlogl. Bulk and surface phases of iron oxides in an oxygen and water atmosphere at low pressure. *Physical Chemistry Chemical Physics*, 3:1114, 2001.

[206] N. G. Condon, F. M. Leibsle, A. R. Lennie, P. W. Murray, D. J. Vaughan, and G. Thornton. Biphase ordering of iron oxide surfaces. *Physical Review Letters*, 75 (10):1961, 1995.

[207] N. G. Condon, F. M. Leibsle, T. Parker, A. R. Lennie, D. J. Vaughan, and G. Thornton. Biphase ordering on $Fe_3O_4(111)$. *Physical Review B*, 55(23):15885, 1997.

[208] M. Paul, M. Sing, R. Claessen, D. Schrupp, and V. A. M. Brabers. Thermodynamic stability and atomic and electronic structure of reduced $Fe_3O_4(111)$ single-crystal surfaces. *Physical Review B*, 76(7):075412, 2007.

[209] J. Wintterlin, J. Trost, S. Renisch, R. Schuster, T. Zambelli, and G. Ertl. Real-time STM observations of atomic equilibrium fluctuations in an adsorbate system: O/Ru(0001). *Surface Science*, 394(1–3):159–169, 1997.

[210] C. Corriol, F. Calleja, A. Arnau, J. J. Hinarejos, A. L. Vázquez de Parga, W. A. Hofer, and R. Miranda. Role of surface geometry and electronic structure in STM images of O/Ru(0001). *Chemical Physics Letters*, 405(1–3):131, 2005.

[211] C. M. Schneider and G. Schönhense. Investigating surface magnetism by means of photoexcitation electron emission microscopy. *Reports on Progress in Physics*, 65(12):1785, 2002.

[212] J. P. Crocombette, M. Pollak, F. Jollet, N. Thromat, and M. Gautier-Soyer. X-ray-absorption spectroscopy at the Fe $L_{2,3}$ threshold in iron oxides. *Physical Review B*, 52:3143, 1995.

[213] P. Kuiper, B. G. Searle, L. C. Duda, R. M. Wolf, and P. J. van der Zaag. Fe $l_{2,3}$ linear and circular magnetic dichroism of fe_3o_4. *Journal of Electron Spectroscopy and Related Phenomena*, 86(1-3):107–113, 1997.

[214] K. Mori, M. Yamazaki, T. Hiraki, H. Matsuyama, and K. Koike. Magnetism of a FeO(111)/Fe(110) surface. *Physical Review B*, 72(1):014418, 2005.

[215] L. Giordano, G. Pacchioni, J. Goniakowski, N. Nilius, E. D. L. Rienks, and H. J. Freund. Interplay between structural, magnetic, and electronic properties in a FeO/Pt(111) ultrathin film. *Physical Review B*, 76(7):075416, 2007.

[216] I. Krug. *Magnetic proximity effects in highly-ordered transition metal oxide heterosystems studied by soft X-ray photoemission electron microscopy*. PhD thesis, Universität Duisburg-Essen, 2008.

[217] M. S. Altman, W. F. Chung, Z. Q. He, H. C. Poon, and S. Y. Tong. Quantum size effect in low energy electron diffraction of thin films. *Applied Surface Science*, 169–170:82, 2001.

[218] P. Carra, B. T. Thole, M. Altarelli, and X. Wang. X-ray circular dichroism and local magnetic fields. *Physical Review Letters*, 70(5):694, 1993.

[219] B. T. Thole, P. Carra, F. Sette, and G. van der Laan. X-ray circular dichroism as a probe of orbital magnetization. *Physical Review Letters*, 68(12):1943, 1992.

[220] C. T. Chen, Y. U. Idzerda, H.-J. Lin, N. V. Smith, G. Meigs, E. Chaban, G. H. Ho, E. Pellegrin, and F. Sette. Experimental confirmation of the x-ray magnetic circular dichroism sum rules for iron and cobalt. *Physical Review Letters*, 75:152, 1995.

[221] R. Zboril, M. Mashlan, and D. Petridis. Iron(III) oxides from thermal processes–synthesis, structural and magnetic properties, Mössbauer spectroscopy characterization, and applications. *Chemistry of Materials*, 14(3):969, 2002.

[222] K. Sivula, F. LeFormal, and M. Grätzel. Solar water splitting: Progress using hematite α–Fe_2O_3 photoelectrodes. *ChemSusChem*, 4:432, 2011.

[223] Ö. Özdemir, David J. Dunlop, and T. S. Berquoo. Morin transition in hematite: Size dependence and thermal hysteresis. *Geochemistry, Geophysics, Geosystems*, 9(10):Q10Z01, 2008.

[224] K. Chen, Y. Fan, Z. Hu, and Q. Yan. Carbon monoxide hydrogenation on Fe_2O_3/ZrO_2 catalysts. *Catalysis Letters*, 36(3-4):139, 1996.

[225] S. Minicó, S. Scirè, C. Crisafulli, A. M. Visco, and S. Galvagno. FT-IR study of Au/Fe_2O_3 catalysts for CO oxidation at low temperature. *Catalysis Letters*, 47 (3-4):273, 1997.

[226] H. Sakurai, S. Tsubota, and M. Haruta. Hydrogenation of CO_2 over gold supported on metal oxides. *Applied Catalysis A: General*, 102(2):125, 1993.

[227] W. S. Epling, G. B. Hoflund, J. F. Weaver, S. Tsubota, and M. Haruta. Surface characterization study of Au/α–Fe_2O_3 and Au/Co_3O_4 low-temperature CO oxidation catalysts. *The Journal of Physical Chemistry*, 100:9929, 1996.

[228] H. G. Cha, J. Song, H. S. Kim, W. Shin, K. B. Yoon, and Y. S. Kang. Facile preparation of Fe_2O_3 thin film with photoelectrochemical properties. *Chemical Communications*, 47(8):2441, 2011.

[229] K. Takanabe and K. Domen. Preparation of inorganic photocatalytic materials for overall water splitting. *ChemCatChem*, 4(10):1485, 2012.

[230] C. Jorand Sartoretti, M. Ulmann, B. D. Alexander, J. Augustynski, and A. Weidenkaff. Photoelectrochemical oxidation of water at transparent ferric oxide film electrodes. *Chemical Physics Letters*, 376:194, 2003.

[231] T. W. Hamann. Splitting water with rust: hematite photoelectrochemistry. *Dalton Transactions*, 41(26):7830, 2012.

[232] F. Le Formal, M. Grätzel, and K. Sivula. Controlling photoactivity in ultrathin hematite films for solar water-splitting. *Advanced Functional Materials*, 20(7): 1099, 2010.

[233] K. McCarty, M. Monti, S. Nie, D. Siegel, E. Starodub, F. El Gabaly, A. McDaniel, A. Shavorskiy, T. Tyliszczak, H. Bluhm, N. Bartelt, and J. de la Figuera. Oxidation of magnetite (100) to hematite observed by In-situ spectroscopy and microscopy. *The Journal of Physical Chemistry C*, (Submitted), 2014.

[234] Y. Qiu, S. F. Leung, Q. Zhang, B. Hua, Q. Lin, Z. Wei, K. H. Tsui, Y. Zhang, S. Yang, and Z. Fan. Efficient photoelectrochemical water splitting with ultrathin films of hematite on three-dimensional nanophotonic structures. *Nano Letters*, 14 (4):2123, 2014.

[235] F. L. Souza, K. P. Lopes, E. Longo, and E. R. Leite. The influence of the film thickness of nanostructured α–Fe_2O_3 on water photooxidation. *Physical Chemistry Chemical Physics*, 11(8):1215, 2009.

[236] R. van de Krol, Y. Liang, and J. Schoonman. Solar hydrogen production with nanostructured metal oxides. *Journal of Materials Chemistry*, 18(20):2311, 2008.

[237] R. J. Lad and V. E. Henrich. Structure of α–Fe_2O_3 single crystal surfaces following Ar^+ ion bombardment and annealing in O_2. *Surface Science*, 193(1–2):81, 1988.

[238] R. A. Fellows, A. R. Lennie, H. Raza, C. L. Pang, G. Thornton, and D. J. Vaughan. $Fe_3O_4(111)$ formation on a reduced α–$Fe_2O_3(11\bar{2}3)$ substrate: a low-energy electron diffraction and scanning tunnelling microscopy study. *Surface Science*, 445 (1):11, 2000.

[239] T. Fujii, D. Alders, F. C. Voogt, T. Hibma, B. T. Thole, and G. A. Sawatzky. In situ RHEED and XPS studies of epitaxial thin α–$Fe_2O_3(0001)$ films on sapphire. *Surface Science*, 366(3):579, 1996.

[240] Y. Gao, Y. J. Kim, and S. A. Chambers. Preparation and characterization of epitaxial iron oxide films. *Journal of Materials Research*, 13(07):2003, 1998.

[241] S. K. Shaikhutdinov and W. Weiss. Oxygen pressure dependence of the α–$Fe_2O_3(0001)$ surface structure. *Surface Science*, 432(3):L627, 1999.

[242] S. A. Chambers and S. I. Yi. Fe termination for α–Fe_2O_3 as grown by oxygen-plasma-assisted molecular beam epitaxy. *Surface Science*, 439(1–3):L785–L791, September 1999.

[243] X. Deng and C. Matranga. Selective growth of Fe_2O_3 nanoparticles and islands on Au(111). *The Journal of Physical Chemistry C*, 113(25):11104, 2009.

[244] A. Barbier, R. Belkhou, P. Ohresser, M. Gautier-Soyer, O. Bezencenet, M. Mulazzi, M. J. Guittet, and J. B. Moussy. Electronic and crystalline structure, morphology, and magnetism of nanometric Fe_2O_3 layers deposited on Pt(111) by atomic-oxygen-assisted molecular beam epitaxy. *Physical Review B*, 72:245423, 2005.

[245] Y. J. Kim, Y. Gao, and S. A. Chambers. Selective growth and characterization of pure, epitaxial α–$Fe_2O_3(0001)$ and $Fe_3O_4(001)$ films by plasma-assisted molecular beam epitaxy. *Surface Science*, 371(2–3):358, 1997.

[246] C. H. Lanier, A. N. Chiaramonti, L. D. Marks, and K. R. Poeppelmeier. The Fe_3O_4 origin of the "biphase" reconstruction on α–$Fe_2O_3(0001)$. *Surface Science*, 603(16):2574, 2009.

[247] Y. Tang, H. Qin, K. Wu, Q. Guo, and J. Guo. The reduction and oxidation of $Fe_2O_3(0001)$ surface investigated by scanning tunneling microscopy. *Surface Science*, 609:67, 2013.

[248] N. G. Condon, F. M. Leibsle, A. R. Lennie, P. W. Murray, T. M. Parker, D. J. Vaughan, and G. Thornton. Scanning tunnelling microscopy studies of α–$Fe_2O_3(0001)$. *Surface Science*, 397(1–3):278, 1998.

[249] N. G. Condon, P. W. Murray, F. M. Leibsle, G. Thornton, A. R. Lennie, and D. J. Vaughan. $Fe_3O_4(111)$ termination of α–$Fe_2O_3(0001)$. *Surface Science*, 310(1–3): L609, 1994.

[250] A. Kiejna and T. Pabisiak. Mixed termination of hematite (α–Fe_2O_3)(0001) surface. *The Journal of Physical Chemistry C*, 117(46):24339, 2013.

[251] R. Dronskowski. The little maghemite story: A classic functional material. *Advanced Functional Materials*, 11(1):27, 2001.

[252] H. Takei and S. Chiba. Vacancy ordering in epitaxially-grown single crystals of γ–Fe_2O_3. *Journal of the Physical Society of Japan*, 21(7):1255, 1966.

[253] A. N. Shmakov, G. N. Kryukova, S. V. Tsybulya, A. L. Chuvilin, and L. P. Solovyeva. Vacancy Ordering in γ–Fe_2O_3: Synchrotron X-ray Powder Diffraction and High-Resolution Electron Microscopy Studies. *Journal of Applied Crystallography*, 28(2):141, 1995.

[254] R. Grau-Crespo, A. Y. Al-Baitai, I. Saadoune, and N. H. de Leeuw. Vacancy ordering and electronic structure of γ–Fe_2O_3 (maghemite): a theoretical investigation. *Journal of Physics: Condensed Matter*, 22(25):255401, 2010.

[255] H. Yanagihara, M. Hasegawa, E. Kita, Y. Wakabayashi, H. Sawa, and K. Siratori. Iron vacancy ordered γ–$Fe_2O_3(001)$ epitaxial films: The crystal structure and electrical resistivity. *Journal of the Physical Society of Japan*, 75:054708, 2006.

[256] M. Hasegawa, H. Yanagihara, Y. Toyoda, E. Kita, and L. Ranno. Electrical and magnetic properties of γ–Fe_2O_3 epitaxial films. *Journal of Magnetism and Magnetic Materials*, 310:2283, 2007.

[257] G. Bate. Magnetic recording materials since 1975. *Journal of Magnetism and Magnetic Materials*, 100(1–3):413, 1991.

[258] M. Sugimoto. The past, present, and future of ferrites. *Journal of the American Ceramic Society*, 82(2):269, 1999.

[259] F. C. Voogt, T. Fujii, P. J. M. Smulders, L. Niesen, M. A. James, and T. Hibma. NO_2-assisted molecular-beam epitaxy of Fe_3O_4, $Fe_{3-\delta}O_4$, and γ–Fe_2O_3 thin films on MgO(100). *Physical Review B*, 60(15):11193, 1999.

[260] T. Manago, T. Sonobe, I. Yamaguchi, and F. Takano. Lattice template effect on epitaxial γ–Fe_2O_3 films prepared by metal organic deposition. *Journal of Applied Physics*, 107(5):053908, 2010.

[261] Y. Gao, Y. J. Kim, S. Thevuthasan, S. A. Chambers, and P. Lubitz. Growth, structure, and magnetic properties of γ–Fe_2O_3 epitaxial films on MgO. *Journal of Applied Physics*, 81(7):3253, 1997.

[262] S. B. Ogale, V. N. Koinkar, Sushama Joshi, V. P. Godbole, S. K. Date, A. Mitra, T. Venkatesan, and X. D. Wu. Deposition of iron oxide thin films by pulsed laser evaporation. *Applied Physics Letters*, 53(14):1320, 1988.

[263] F. Bertram, C. Deiter, K. Pflaum, M. Suendorf, C. Otte, and J. Wollschläger. In-situ x-ray diffraction studies on post-deposition vacuum-annealing of ultra-thin iron oxide films. *Journal of Applied Physics*, 110(10):102208, 2011.

[264] F. C. Voogt, P. J. M. Smulders, G. H. Wijnja, L. Niesen, T. Fujii, M. A. James, and T. Hibma. NO_2-assisted molecular-beam epitaxy of wustitelike and magnetitelike fe oxynitride films on MgO(100). *Physical Review B*, 63(12):125409, 2001.

[265] S. A Chambers and S. A Joyce. Surface termination, composition and reconstruction of $Fe_3O_4(001)$ and γ–$Fe_2O_3(001)$. *Surface Science*, 420(2–3):111, 1999.

[266] K. J. Gallagher, W. Feitknecht, and U. Mannweiler. Mechanism of oxidation of magnetite to γ–Fe_2O_3. *Nature*, 217:1118, 1968.

[267] W. Feitknecht and K. J. Gallagher. Mechanisms for the oxidation of Fe_3O_4. *Nature*, 228(5271):548, 1970.

[268] R. Dieckmann. Defects and cation diffusion in magnetite (IV): nonstoichiometry and point defect structure of magnetite (Fe_3O_4). *Berichte der Bunsengesellschaft für physikalische Chemie*, 86(2):112, 1982.

[269] U. Colombo, F. Gazzarrini, G. Lanzavecchia, and G. Sironi. Magnetite oxidation: A proposed mechanism. *Science*, 147(3661):1033, 1965.

[270] U. Colombo, G. Fagherazzi, F. Gazzarrini, G. Lanzavecchia, and G. Sironi. Mechanisms in the first stage of oxidation of magnetites. *Nature*, 202(4928):175, 1964.

[271] F. Zhou and G. Ceder. First-principles determination of charge and orbital interactions in Fe_3O_4. *Physical Review B*, 81(20):205113, 2010.

[272] C. Schlueter, M. Lübbe, A. M. Gigler, and W. Moritz. Growth of iron oxides on Ag(111)-reversible Fe_2O_3/Fe_3O_4 transformation. *Surface Science*, 605(23-24): 1986, 2011.

[273] M. Xue, S. Wang, K. Wu, J. Guo, and Q. Guo. Surface structural evolution in iron oxide thin films. *Langmuir*, 27(1):11, 2010.

[274] C. P. Markus. *Molecular Beam Epitaxy and Properties of Magnetite Thin Films on Semiconducting Substrates*. PhD thesis, Julius-Maximilians-Universität Würzburg, 2010.

[275] T. Schedel-Niedrig, W. Weiss, and R. Schlögl. Electronic structure of ultrathin ordered iron oxide films grown onto Pt(111). *Physical Review B*, 52(24):17449, 1995.

[276] E. Pellegrin, M. Hagelstein, S. Doyle, H. O Moser, J. Fuchs, D. Vollath, S. Schuppler, M. A James, S. S Saxena, L. Niesen, O. Rogojanu, G. A Sawatzky, C. Ferrero, M. Borowski, O. Tjernberg, and N. B Brookes. Characterization of nanocrystalline γ-Fe_2O_3 with synchrotron radiation techniques. *physica status solidi (b)*, 215(1): 797, 1999.

[277] Z. Y. Wu, S. Gota, F. Jollet, M. Pollak, M. Gautier-Soyer, and C. R. Natoli. Characterization of iron oxides by x-ray absorption at the oxygen K edge using a full multiple-scattering approach. *Physical Review B*, 55(4):2570, 1997.

[278] S. Giovannini, F. Boscherini, R. Carboni, L. Signorini, L. Pasquini, N. Mahne, A. Giglia, M. Pedio, S. Nannarone, M. Benfatto, and S. Della Longa. Multiple scattering analysis of O K Edge NEXAFS in iron oxides. *Physica Scripta*, T115: 424, 2005.

[279] U. Colombo, G. Fagherazzi, F. Gazzarrini, G. Lanzavecchia, and G. Sironi. Mechanism of low temperature oxidation of magnetites. *Nature*, 219(5158):1036, 1968.

[280] R. L. Mössbauer. Kernresonanzfluoreszenz von gammastrahlung in Ir^{191}. *Zeitschrift für Physik*, 151(2):124, 1958.

[281] G. J. Long. *Mössbauer Spectroscopy Applied to Inorganic Chemistry*. Springer, 1984.

[282] G. N. Belozerski. *Mössbauer Studies of Surface Layers*. Elsevier Science, 1993.

[283] C. Van Cromphaut, V. G. de Resende, E. De Grave, L. Presmanes, I. Pasquet, and P. Thaillades. ILEEMS of thin α–Fe_2O_3 films prepared by RF sputtering. *Hyperfine Interactions*, 189(1-3):175, 2009.

[284] C. Van Cromphaut, V. G. de Resende, E. De Grave, and R. E. Vandenberghe. Surface effects in α–Fe_2O_3 nanoparticles studied by ILEEMS and TMS. *Hyperfine Interactions*, 191(1-3):167, June 2009.

[285] J. R. Gancedo, J. Z. Dávalos, M. Gracia, and J. F. Marco. The use of Mössbauer spectroscopy in surface studies. A methodological survey. *Hyperfine Interactions*, 110(1-2):41, 1997.

[286] J. S. Zabinski and B. J. Tatarchuk. Generation mechanisms for low energy electrons produced during relaxation of ^{57}Fe. *Nuclear Instruments and Methods in Physics Research Section B: Beam Interactions with Materials and Atoms*, 42(3):379, 1989.

[287] J. S. Zabinski and B. J. Tatarchuk. Resonant low energy electrons and their impact on sampling depth during backscatter-electron Mössbauer spectroscopy. *Nuclear Instruments and Methods in Physics Research Section B: Beam Interactions with Materials and Atoms*, 31(4):576, 1988.

[288] J. R. Gancedo and M. Gracia. Cems in non conducting surfaces with a parallel plate avalanche counter. *Hyperfine Interactions*, 29(1-4):1097, 1986.

[289] F. J. Berry, R. Gancedo, J. F. Marco, and R. C. Thied. Mössbauer spectroscopic investigations of metal incorporation within nasicon-related $NbTiP_3O_{12}$. *Journal of the Chemical Society, Dalton Transactions*, page 1703, 1994.